Universitat de les
Illes Balears

Doctoral Thesis
2015

IMPACT OF LARGE-SCALE ATMOSPHERIC VARIABILITY ON SEA LEVEL AND WAVE CLIMATE

Adrián Martínez Asensio

Universitat de les
Illes Balears

Doctoral Thesis
2015

Doctoral Programme of Physics

IMPACT OF LARGE-SCALE ATMOSPHERIC VARIABILITY ON SEA LEVEL AND WAVE CLIMATE

Adrián Martínez Asensio

Thesis Supervisor: Marta Marcos Moreno
Thesis Supervisor: Damià Gomis Bosch

Doctor by the University of the Balearic Islands

List of Publications included in the Doctoral Thesis:

Martínez-Asensio, A., Marcos, M., Jorda, G., Gomis, D., 2013. Calibration of a new wind-wave hindcast in the Western Mediterranean. Journal of Marine Systems 121–122, 1–10.

Martínez-Asensio, A., Marcos, M., Tsimplis, M.N., Gomis, D., Josey, S., Jordà, G., 2014. Impact of the atmospheric climate modes on Mediterranean sea level variability. Global and Planetary Change, 118, 1-15.

Martínez-Asensio, A., Tsimplis, M.N., Marcos, M., Feng. X., Gomis, D., Jordà, G., Josey, S., 2015. Response of the North Atlantic wave climate to atmospheric modes of variability. International Journal of Climatology (accepted)

Martínez-Asensio, A., Marcos, M., Tsimplis, M.N., Jordà, G., Feng. X., Gomis, D., 2015. On the ability of statistical wind-wave models to capture the long-term trends in winter wave climate. Ocean Modelling (in revision).

The 2013 quality features of the journals where the articles were published are:

Journal	Impact Factor	Category Name	Total Journals in Category	Journal Rank in Category	Quartile in Category
JMS[1]	2.476	GEOSCIENCES, MULTIDISCIPLINARY	174	46	Q2
		MARINE & FRESHWATER BIOLOGY	103	20	Q1
		OCEANOGRAPHY	59	16	Q2
GPCH[2]	3.707	GEOGRAPHY, PHYSICAL	46	7	Q1
		GEOSCIENCES, MULTIDISCIPLINARY	173	18	Q1
IJC[3]	3.398	METEOROLOGY & ATMOSPHERIC SCIENCES	76	17	Q1
OM[4]	2.590	METEOROLOGY & ATMOSPHERIC SCIENCES	76	24	Q2
		OCEANOGRAPHY	59	12	Q1

[1] Journal of Marine Systems

[2] Global and Planetary Change

[3] International Journal of Climatology

[4] Ocean Modelling

UIB

Universitat de les
Illes Balears

Dr Marta Marcos Moreno, of the University of Balearic Islands

I DECLARE:

That the thesis titles IMPACT OF LARGE-SCALE ATMOSPHERIC VARIABILITY ON SEA LEVEL AND WAVE CLIMATE, presented by Adrián Martínez Asensio to obtain a doctoral degree, has been completed under my supervision and meets the requirements to opt for an European Doctorate.

For all intents and purposes, I hereby sign this document.

Signature

Palma de Mallorca, 22/05/2015

Universitat de les
Illes Balears

Dr Damià Gomis Bosch, of the University of Balearic Islands

I DECLARE:

That the thesis titles IMPACT OF LARGE-SCALE ATMOSPHERIC VARIABILITY ON SEA LEVEL AND WAVE CLIMATE, presented by Adrián Martínez Asensio to obtain a doctoral degree, has been completed under my supervision and meets the requirements to opt for an European Doctorate.

For all intents and purposes, I hereby sign this document.

Signature

Palma de Mallorca, 22/05/2015

A la memoria de mis abuelos, por mostrarme el camino

A mi familia, por apoyarme siempre

A Eva, mi sueño

L'un, és el mirall de l'altre,
font de vida primigènia
escenari d'una dansa indefinida,
impassible,
aliena al goteig del temps
que alhora crea i omple l'espai.
L'altre, li xiuxiueja a cau d'orella
mentre li acarona subtilment la pell,
embraonant-la,
fent-li expel · lir exhalacions de goig,
sospirs periòdics a colp de batec,
viatgers irreductibles cap a un lloc
desconegut.

JUAN MANUEL SAYOL

Agradecimientos / Acknowledgements

En primer lugar, quiero dar las gracias a todos los ciudadanos que han contribuido, con sus impuestos, a la financiación de esta tesis. Ellos son, al fin y al cabo, los que hacen posible que algunos privilegiados podamos formarnos como científicos. Esta tesis se ha llevado a cabo en el Instituto Mediterráneo de Estudios Avanzados (IMEDEA), gracias a una beca FPI que tuve la suerte de recibir del desaparecido Ministerio de Ciencia e Innovación del Gobierno de España, y que está asociada al proyecto VANIMEDAT-2 (CTM2009-10163-C02-01). Además de poder financiar mi investigación en Mallorca, con esta beca he podido realizar tres estancias en el Reino Unido, las cuales han tenido un papel clave en el desarrollo de esta tesis. Por último, agradecer a la Universidad de las Islas Baleares, la ayuda recibida para poder asistir a diferentes congresos internacionales.

Recuerdo perfectamente aquel día de verano, allá por el 2010, en que, estando sentado a la mesa con mis padres, sonó mi móvil. Era Damià Gomis, que me llamaba para proponerme venir Mallorca a hacer la tesis. En ese momento, me sentí muy afortunado por la posibilidad que me brindaba la vida de poder formarme como científico. Sin embargo, no fue hasta que llegué a esta maravillosa isla, y conocí a las personas con las que luego compartiría mi día a día en IMEDEA, que me di cuenta de lo verdaderamente afortunado que había sido (Gracias Paye, se que moviste los cables desde ahí arriba).

No hay suficientes palabras para expresar mi agradecimiento a mi co-directora de tesis, Marta Marcos. Ella ha sido mi amiga y maestra durante todos estos años, y digo maestra, porque Marta ha sabido transmitirme las cosas a través de la práctica, como en un oficio, de corazón a corazón. Lo ha hecho de tal forma, que ha sacado lo mejor de mí, sin que yo me diera cuenta. He aprendido mucho de ella y, siempre que he ido a tocar la puerta de su despacho (montones de veces, cada día), ha dejado inmediatamente aquello que estuviera haciendo y se ha detenido a escucharme y a ayudarme con una sonrisa sincera. Su dedicación hacia esta tesis y hacia mi formación como científico ha sido mucho mayor de lo que yo nunca hubiera podido imaginar. Gracias, Marta, muchas gracias. (Gracias Paye, se que lo volviste a hacer).

Siempre estaré enormemente agradecido a mi co-director de tesis, Damià Gomis, por todo el apoyo y la dedicación que me ha dado durante estos años. Quiero agradecerle que depositara su confianza en mí para llevar a cabo esta empresa, a pesar de que mi bagaje no fuera el más adecuado. Damià ha co-dirigido esta tesis de manera impecable, siempre ha estado pendiente de mi, y se ha preocupado de guiarme en todo momento, a pesar de ser una persona con tantísimas responsabilidades. Ha corregido con precisión cada uno de los capítulos, los ha impregnado de una pátina de larga experiencia y ha procurado un clima de trabajo en el que siempre me he sentido muy cómodo. Mil gracias, Damià.

Quiero agradecer a Biel Jordà todo el apoyo recibido a lo largo de la tesis. Siempre que lo he necesitado, Biel ha tenido la paciencia de explicarme los conceptos más básicos, y aclararme dudas de todo tipo, y también de ayudarme a solucionar problemas imposibles de la manera más sencilla e inteligente. No solo ha revisado con mucho cuidado cada uno de los artículos y ha aportado muchísimas ideas, sino que me ha proporcionado la mayor parte de los datos utilizados en esta tesis. Gracias por todo, Biel.

También quiero agradecer la atención recibida a los otros miembros del grupo, como son Sebastià Montserrat, con quien he pasado muy buenos ratos aprendiendo sobre mecánica de fluidos; Antonio Sánchez, por su ayuda en el tercer capítulo; a Marga Palmer y a Guy Woppelmann. a quien agradezco que me invitara a dar una charla a La Rochelle, y nos regalara unos días estupendos, junto con Marta y Belén. Quiero dar las gracias a Josep Llasses, por su amistad y compañerismo, y por los buenos ratos que hemos pasado juntos; a Ángel Amores, por salvarme el pellejo con las clases y por el cachondeo que se trae siempre.

I want to thank Mikis Tsimplis for giving me the opportunity to work with him in Southampton. It was a very enriching experience for me, not only in an academic or professional level, but also personal. Three chapters of this thesis were developed at NOC and the true is that working with Mikis is like playing a funny game where the original ideas and challenges constantly flow. I feel I have learnt a lot with him. I thank Xiangbo Feng for drawing the attention and help to me with the chapters on waves, but above all, for the friendship he showed me during I was a NOC. I also thank Simon Josey for the help with the chapters on climate modes. I want to thank Eleni Trotzi for sharing with me many friends, conversations, dinners, breads, decafs, music, wines, joys and sorrows, thanks for all, Leni. I thank to Matti, for his fellowship and great sense of humour. Gracias a Rafael Jaume, por llevarme a la cantina casi todas las mañanas para empezar el día con una buena dosis de carcajadas y de buen rollo. A Kiko Calafat le agradezco toda la atención y la confianza recibida durante mi última estancia en el NOC. I cannot overlook Andrew Shaw and Chris Banks, with whom I spent good times at the office.

Quiero dar las gracias a todas las personas que he conocido en IMEDEA y que han contribuido de alguna forma a esta tesis. Son tantas que seguro que me olvido de muchas. En primer lugar, agradecer a todos aquellos que ha pasado por la Conti-cueva: Juanma (a.k.a. El Juat-man), muchas gracias por permitir que te fuera explicando detalladamente cada pequeño avance de la tesis, cada figura, cada presentación, y por discutirlas conmigo y darme tus consejos. Gracias por las discusiones de última hora sobre cualquier tema interesante, por ayudarme con las clases y por organizar conmigo las Charlas Imedéic@s. Ha sido un verdadero placer y un privilegio poder aprender tantas cosas juntos. Quiero agradecer a Romain (a.k.a. El Pucelano del Norte) el haberme ayudado a dar mis primeros pasos en MATLAB (estoy seguro de que todo hubiera sido mucho más lento de no haber sido por sus consejos) y por los buenos ratos que hemos pasado aprendiendo oceanografía (de la buena) encima de la tabla. Gracias también a Inés (a.k.a. La Hipiiiie), por el cariño que siempre me ha dado, hasta que nos abandonó, claro ;) y por su amor compartido al buen pan; a Dani Conti (a.k.a. El Desaparecido), por sus frases míticas; a Isma (a.k.a. El Ismafrutis), por ser el alma de la fiesta siempre, ya sea en el trabajo o en los Carnavales de Cádiz; a Gema (a.k.a. Gémula de Esponja), por sus galletas de chocolate y por su religioso"¡buenos días, compañeros!"; a Bárbara (a.k.a. La Salsera de Porreres), por contagiarnos el ritmo de esa forma; a Carlos (a.k.a. el Gambita), por compartir las cosas buenas de la vida; y gracias también a los recién llegados, Esther (a.k.a. La Profe) y Dani (a.k.a, El Bluesman), porque ellos heredarán la Conti-cueva. También quiero dar las gracias a Jano por su atención durante estos años y por el curso de oleaje que nos dio desinteresadamente.

Ya llevo casi tres páginas y todavía no he terminado de dar las gracias, y es que cuatro años rodeado de tanta gente dan para mucho. Además de las personas que ya he nombrado, hay otras que han contribuido a que mi etapa en Mallorca haya sido, sin duda, la mejor época de mi vida. Muchas de ellas ya han volado, Veriozka, Bea, Pedro, Sámer, Lauriña, Luana, Juanki, Albert, Lucie,...otros todavía siguen por aquí, Rubén, Daffne, Javi, Morten, Ceci, Aquetzalli, Richi, Francesca, Merit, Jordi, Noe, Johnna, Marc, Natascha,...aunque hay muchos más. A todos ellos, gracias, muchas gracias. Gracias a Cati, Balbina y Ramona, por su simpatía, y a Toni y a Jaime por sus buenos días y hasta mañanas. También quiero agradecer a mis amigos de Ibi el haber estado siempre pendientes de mi, en especial a Ángel, al Jorge y al Juli, que es el artista que se ha currado la portada de esta tesis, y también a los amigos de Barna, el Berru, el Xavi, el Víctor, la Mireia y la María.

Quiero agradecer a Eva el haber estado a mi lado durante todo este tiempo, y que me haya cuidado con tanto cariño. Gracias a ella he aprendido a valorar las cosas realmente importantes de la vida (Gracias Paye, te pasaste!).

Quiero agradecer a mi querida familia el haber estado siempre tan cerca de mí, a pesar de la distancia. A mi madre, le agradezco, entre muchas otras cosas, todo el esfuerzo que ha hecho para sacarme adelante, para que la vea siempre sonriendo y para enseñarme a ser feliz y en la vida. A mi padre le agradezco, sobre todo, el esfuerzo que ha hecho para que no me falte de nada, para enseñarme el valor del trabajo, y el significado del esfuerzo y de la disciplina. A mi hermana le quiero agradecer todo el cariño que me ha dado. A mi tita, mi segunda madre, le agradezco que haya estado siempre tan cerca de mí.

Abstract

This thesis aims at quantitatively characterizing the recent (last few decades) and future climate variability of marine climate in the Western Mediterranean Sea and the North Atlantic Ocean. Namely it focuses on sea level and wind-waves, as these are the variables with a larger potential impact on coastal ecosystems and infrastructures. We first use buoy and altimetry data to calibrate a 50-year wind-wave hindcast over the Western Mediterranean in order to obtain the best characterization of the wave climate over that region. The minimization of the differences with respect to observations through a non-linear transformation of the Empirical Orthogonal Functions of the modelled fields results in an improvement of the hindcast, according to a validation test carried out with independent observations. We then focus on the relationship between the large scale atmospheric forcing and our target variables. Namely we quantify and explore the cause-effect relations between the major modes of atmospheric variability over the North Atlantic and Europe, i.e. the North Atlantic Oscillation, the East Atlantic pattern, the East Atlantic Western Russian pattern and the Scandinavian pattern, and both the Mediterranean sea level and the North Atlantic wave climate. To do so, we use data from different sets of observations and numerical models, including tide gauges, wave buoys, altimetry, hydrography and numerical simulations. Our results point to the North Atlantic Oscillation as the mode with the largest impact on both, Mediterranean sea level (due to the local and remote influence on its atmospheric component) and the North Atlantic wave climate (due to its effect on both the wind-sea and swell components). Other climate indices have smaller but still meaningful contributions; e.g. the East Atlantic pattern plays a significant role in the wave climate variability through its impact on the swell component. Finally, we explore the performance of statistical models to project the future wave climate over the North Atlantic under global warming scenarios, including the large scale climate modes as predictors together with other variables such as atmospheric pressure and wind speed. Notably, we highlight that the use of wind speed as statistical predictor is essential to reproduce the dynamically projected long-term trends.

Resumen

Esta tesis caracteriza cuantitativamente la variabilidad climática reciente (las últimas décadas) y futura del clima marino en el Mar Mediterráneo y en el Océano Atlántico Norte. Concretamente, se centra en el nivel del mar y en el oleaje, ya que éstas son las variables con un mayor impacto potencial en ecosistemas e infraestructuras costeras. En primer lugar, utilizamos datos de boyas y altimetría para calibrar un hindcast de oleaje de 50 años en el Mediterráneo Occidental, con el objetivo de obtener la mejor caracterización climática del oleaje sobre esta región. La minimización de las diferencias con respecto a las observaciones a través de una transformación no lineal de las Funciones Empíricas Ortogonales de los campos modelados se traduce en una mejora del hindcast, de acuerdo al test de validación llevado a cabo con observaciones independientes. Luego nos centramos en las relaciones entre el forzamiento atmosférico de gran escala y nuestras variables de interés. En concreto, cuantificamos y exploramos las relaciones causa-efecto entre los modos de variabilidad atmosférica más importantes del Atlántico Norte y Europa (la Oscilación del Atlántico Norte, el patrón del Atlántico Oriental, el patrón del Atlántico Oriental/Rusia Occidental y el patrón Escandinavo) y el nivel del mar del Mediterráneo y el oleaje del Atlántico Norte. Para ello, usamos datos de diferentes conjuntos de observaciones y modelos numéricos, incluyendo mareógrafos, boyas de oleaje, altimetría, hidrografía y simulaciones numéricas. Nuestros resultados señalan la Oscilación del Atlántico Norte como el modo de mayor impacto, tanto en el nivel del mar del Mediterráneo (debido a la influencia local y remota en su componente atmosférica) como en el oleaje del Atlántico Norte (debido a su efecto en las componentes de mar de viento y de mar de fondo) Otros índices climáticos tienen contribuciones más pequeñas pero todavía significativas; e.g. el patrón del Atlántico Oriental juega un papel importante en la variabilidad del oleaje a través de su impacto en la componente de mar de fondo. Finalmente, exploramos la capacidad de los modelos estadísticos de proyectar el clima futuro del oleaje sobre el Atlántico Norte bajo escenarios de calentamiento global, incluyendo los modos climáticos de gran escala como predictores junto con otras variables como la presión atmosférica y la velocidad del viento. En particular, destacamos que el uso de la velocidad del viento como predictor estadístico es esencial para reproducir las tendencias a largo plazo proyectadas de por los modelos dinámicos.

Contents

List of abbreviations and acronyms

ISDM	Integrated Science Data Management
AEMET	Agencia Estatal de Meteorología
AO	Arctic Oscillation
CANDHIS	Centre d'Archivage National de Donnés de Houle In Situ
DAC	Dynamic Atmospheric Correction
DJF	December to February
DJFM	December to March
DynHist	Historical wind-wave simulation
DynProj	Future wind-wave simulation
EA	East Atlantic pattern
EA/WR	East Atlantic Western Russian pattern
ECMWF	European Centre for Medium-Range Weather Forecasts
EN	Envisat
EOF	Empirical Orthogonal Function
ERS-1	European Remote Sensing 1
ERS-2	European Remote Sensing 2
G	Sea level pressure gradient
G2	Geosat Follow On
GCM	General Circulation Model
GHG	Greenhouse gas
GIA	Glacial Isostatic Adjustment
HE40	ERA-40 wind-wave hindcast
HEI	ERA-INTERIM wind-wave hindcast
IH	Instituto Hidrográfico - Portuguese Navy
IPCC	Intergovernmental Panel on Climate Change
ISPRA	Istituto Superiore per la Protezione e la Ricerca Ambientale
J1	Jason-1
J2	Jason-2
JJAS	June to September
M	Mean
MAMJ	From March to May
METEO-FRANCE	French National Meteorological Service
MOI	Mediterranean Oscillation Index
MPI	Max Plank Institute
MSLP	Mean sea level atmospheric pressure
MWD	Mean wave direction
MWP	Mean wave period
NAM	Northern Hemisphere Annular Mode

NAO	North Atlantic Oscillation
P	Sea level pressure
PC	Principal Component
PNA	Pacific-North American pattern
PSMSL	Permanent Service for Mean Sea Level
RLR	Revised Local Reference
RMS	Root Mean Squared
RMSD	Root Mean Squared difference
S	Salinity
SCAN	Scandinavian pattern
SLA	Sea Level Anomaly
SOND	From September to December
STD	Standard deviation
SWH	Significant wave heights
T	Temperature
TNH	Tropical-Northern Hemisphere pattern
TP	Topex/Poseidon
U10	10m wind speed
URMSD	Unbiased Root Mean Squared difference
V	Variance
WP	West-Pacific pattern
XIOM	Xarxa d'Instruments Oceanogràfics i Meteorològics

Chapter 1

Introduction: The marine climate of the North-east Atlantic Ocean and the Mediterranean Sea

— Y qué importa que lo que yo cuente esté o no escrito en algún libro muy sabio? ¿Quién os dice a vosotros que las historias que ponen en los libros sabios no sean también inventadas, sólo que nadie se acuerda ya?

— Maybe you won't find my stories in any guidebook, but what's the difference? Who knows if the stuff in the guidebooks isn't made up too, only no one remembers any more.

Michael Ende, Momo (1973)

1.1 The concept of marine climate

The term marine climate is commonly used to define the statistical properties of the state of the atmosphere (weather) and the corresponding state of the oceans (marine weather) (Weisse et al., 2010). Changes in marine climate can have significant impacts on the coastal and marine environment. For example, small variations in water temperature and salinity can induce notable changes on the structure and functioning of the ecosystems. Among the set of parameters that characterize the marine climate, sea level and wind waves are considered as high impact variables due to their high-cost effects on coastal and offshore areas, especially in highly developed and populated regions. The term marine climate used throughout this thesis will restrict to these high impact variables.

The direct physical effects of sea level variations are coastal erosion, changes in the flooding level and salinity intrusion into estuaries and coastal aquifers (Sorenson et al., 1984). On the other hand, wind waves affect the stability of coastal structures, ship routing and harbour operations; it also affects the configuration of beaches and the ecology of shallow waters and low-lying areas (Burrows et al., 2008). The considerations that 10% of the world population live at less than 10 m above mean sea level (McGranahan et al., 2007) and that maritime traffic represents more than 90% of world's trade give by themselves a measure of the potential economical and societal impact of sea level and wave climate. As populations grow, the knowledge on marine climate becomes critical in order to guarantee future successful management strategies.

The term marine climate change refers to changes in the marine climate that occur over decadal to millennium time scales. These long-term changes are due to different factors, such as changes in the Earth's orbit, changes in the solar activity and natural or anthropogenic changes in the atmospheric chemistry. These factors determine the global climate of the Earth and also strongly influence the climate at regional and local scales. Superimposed onto these long-term changes, there is also seasonal and inter-annual variability.; e.g. some years have higher than normal sea levels and wave heights, as it was the case of the recent winter 2013-14 over most of the North Atlantic region. These yearly fluctuations above or below a long-term average value are called marine climate variability.

Although the marine weather may appear to vary randomly, it is related to the inter-annual and longer time scales of extra-tropical atmospheric circulation, which is organized into well-defined spatial patterns. These large-scale patterns mainly consist of atmospheric anomalies (with respect to a spatial average value) that have opposite sign over distant parts of the globe and vary between two possible states in such a way that they are teleconnected. These patterns or modes do not need any forcing to be generated. They occur naturally in the climate system due to its own inherent dynamics and constitute major drivers of weather and climate variability (Timm et al., 2004). As variations in the frequency and intensity of the modes affect large regions, they have major impacts on societies and ecosystems. In the North Atlantic, the coordinated variations of both mid-latitude pressure centres (i.e. the subtropical Azores-High and the Iceland-Low) and the related strength and location of the Westerlies and Trades are referred to as the North Atlantic Oscillation (NAO). It is worth noting that the term oscillation in the acronym NAO refers to a spatial oscillation of the air mass between the Arctic and the subtropical Atlantic, its time variation being mostly random (Hurrel and Deser, 2009). Modes are also expressed in the time domain as climate indices that represent the overall physical variability of the system.

The NAO is not the only mode with a significant impact on the marine climate of the Mediterranean and the North Atlantic region; other large scale patterns, such as the East Atlantic pattern (EA), the Scandinavian pattern (SCAN) and the East Atlantic/Western Russian (EA/WR) pattern have also been identified to play a relevant role on, for example, air-sea heat exchanges over the Mediterranean (Josey et al., 2011). As climate indices include information of large-scale variations in atmospheric and oceanic parameters like temperature, pressure or precipitation, they account for a high amount of climate variability. The NAO and the other internal modes of atmospheric variability are superimposed onto the long-term climate change signal, altogether with shorter term events such as volcanic eruptions. For instance, the persistence of positive phases of the NAO between the 1960s and 1990s resulted in a significant sea level rise differences between the Mediterranean Sea and the global ocean (Tsimplis et al, 2005; Marcos and Tsimplis, 2008 and references therein). Likewise, inter-annual changes in the NAO can be determinant for mean sea level changes in the Mediterranean basin (Gomis et al., 2006; Tsimplis et al, 2013; Landerer and Volkov, 2013).

1.2 Wind-wave and sea level climate of the North-east Atlantic Ocean and the Mediterranean Sea

The main features of the marine climate over the North Atlantic Ocean and the Mediterranean Sea are determined by the air temperature gradient between the North Pole and the Equator, which in turn is due to the meridional variation of the Earth's insolation. The meridional air temperature gradient is higher over the western North Atlantic than over the eastern North Atlantic and the Mediterranean and it is also higher during the winter season (Isemer and Hasse, 1985). Overall the gradient results in the organization of the atmospheric circulation in the well-known three-cell system associated with the Equatorial-Low, the subtropical Azores-High, the Iceland-Low and the North Pole-High pressure centres. The Coriolis force caused by the Earth's rotation makes the air to flow clockwise around high pressure centres and counter-clockwise around low pressure centres in the Northern Hemisphere, thus leading to three relatively persistent wind systems: south-westwards winds at low latitudes (Trades), north-eastwards winds at middle latitudes (Westerlies) and south-westwards winds at high latitudes (Polar Easterlies).

The described pattern of surface winds determines the mean wave climate over the North Atlantic: highest waves are observed in the extra-tropical regions under the influence of the Westerlies and also in the tropical regions affected by the Trades. The Westerlies generate higher waves with larger directional variability than those generated by the Trades, which are weaker and more persistent in speed and direction (Semedo et al, 2011). Although wind speed is closely related to wave heights, the spatial patterns of the two fields are not analogous due to the propagation of waves over long distances (over thousands of kilometres, Chen et al, 2002). Thus the wave field can be considered as the results of two components: the wind-sea and the swell. The first term refers to wind-waves that are locally produced when the wind blows over the ocean surface. The swell refers to waves propagating away from the generation region and therefore not being related to the local wind. During winter, the wind-sea is higher along the Westerly winds than along the Trade winds, and the swells generated by the Westerlies at extra-tropical latitudes travel southwards and become the dominant component of equatorial regions. During the summer season, the wind-sea is higher along the Trade winds than along the Westerly winds, and the swell component is much lower than during winter (Semedo et al., 2011).

Regarding the variability of the marine climate of Europe and the Mediterranean region, this is dominated by the storm track of the Westerlies in winter and by the Azores anticyclone in summer. During spring and autumn intermediate conditions prevail. Storm tracks are variable over the eastern North Atlantic and the Mediterranean region. In the latter they are highly influenced by the complex topography of the basin (Brayshaw et al., 2010). The relative warmer conditions of the Mediterranean Sea from fall to spring lead to surface cyclogenesis that enhance eastward storms coming from the Atlantic, especially over the western sub-basin (Trigo et al., 2012). Thus Mediterranean cyclonic activity is mainly associated with strong and persistent north and north-westerly winds (locally known as Tramuntana and Mistral) which enter the basin through the passage between the Pyrenees and the Alps. The opposite occurs during summer months, when the Mediterranean Sea cools the upper atmosphere leading to anticyclonic atmospheric conditions over the basin. Trends on storminess and wind-wave parameters have been detected using satellite altimetry. However, the period is too short to distinguish if they are a consequence of climate change or correspond to decadal natural variability (Young et al., 2011).

Winds are also one of the major forcing of sea level. Altogether with atmospheric pressure they constitute the forcing of the atmospheric component of long-term sea level variability. The other components are the variability in the density of the water column (referred to as the steric component) and the variability in the mass derived from non-atmospheric forcing (referred to as the mass component). There are evidences that the atmosphere and the oceans have warmed, on average, during the last century. The latest Intergovernmental Panel on Climate Change Assessment Report (IPCC AR5, 2013) concluded with a high degree of confidence that the human activities have substantially contributed to the increase of global mean surface temperature and the corresponding sea level rise (Bindoff et al., 2013). The mean contributors to global sea level rise during the last century are the increase in ocean mass due to the melting of glaciers and ice sheets and the thermal expansion of the water masses due to the ocean warming (Church et al., 2013). Global mean sea level rose at a rate of 1.3-1.9 mm/year between 1901 and 2010 (Church and White, 2011; Jevrejeva et al 2014; Hay et al, 2015) and at 3.2 mm/yr between 1993 and 2010 (Cazenave and Llovel, 2010).

At regional scales changes in sea level can significantly deviate from the global mean because of changes in the ocean dynamics and water mass redistribution (Stammer et al, 2013). In particular, the atmospheric forcing, which averages to zero for global mean sea level, contributes to regional differences. For instance, the Mediterranean mean sea level increased at a lower rate than in the neighbouring North Atlantic during 1961-2000 due to the increase of atmospheric pressure over the region (Tsimplis and Josey, 2001; Marcos and Tsimplis, 2008; Gomis et al., 2008; Calafat and Gomis, 2009). Also longer term sea level trends are lower in the Mediterranean Sea that at the global scale; they have been estimated in 1.2 mm/yr for the 20th century using the longest available tide gauges (Tsimplis and Baker, 2000; Marcos and Tsimplis, 2008; Woppelmann et al, 2014). Other studies used long tide gauge records to explore changes in extreme high water levels associated with storminess. They demonstrated the regional nature of such variations and found evidence of increased activity either due to a enhanced storminess (Menéndez and Woodworth, 2010) or due to the combined effect of mean sea level rise with storm surges (Araújo and Pugh, 2008 in Newlyn tide gauge; Marcos et al, 2009 in Southern Europe).

1.3 The study of the climate system: observations and numerical modelling

The key methods to study the dynamics of the climate system are the analysis of observed data and the numerical experiments with climate models. Regarding the former, ocean surface observations can be obtained from different sources. In-situ observations of coastal sea level are obtained from tide gauges at high temporal (typically hourly) resolution. Tide gauges are one of the oldest measurement systems of the ocean surface, some of them spanning more than one century. The oldest records of wind-waves are visual observations from ships, although they are located only over the major navigation routes. Nowadays in-situ observations of wind-waves are obtained from wave buoys anchored on either coastal or deep waters. The buoys provide information at high temporal (typically 3-hourly) resolution on height, period and direction of the waves and in some cases also their wind-sea and swell components. In-situ observations of other oceanographic and atmospheric variables such as atmospheric pressure, wind, temperature or salinity are also necessary to study the mechanisms driving the marine climate variability. The development of satellite remote sensors during the 1970s constituted a revolution in understanding the marine climate due to their quasi-global spatial coverage. For the key parameters of marine climate the step forward was the development of satellite altimeters during the early 1990s, as they provide a nearly synoptic view of sea level, winds and wave height over the globe. Their counterpart is a low spatio-temporal resolution (tens of kilometres and between 10 and 30 days, respectively), which limits the understanding of some of the physical processes involved in marine climate variability.

One way to overcome the problem of limited measurements is to combine observations with numerically simulated fields of the target variables. Numerical models can realistically simulate a sequence of weather events by solving the primitive equations that describe the physical processes of the Earth System, including atmosphere, oceans, land and their interactions. When used for (atmospheric and/or marine) weather forecasting, numerical models include data assimilation from different observational sources. The same models can also be forced with historical observations and used to produce reanalysis, which are a collection of weather maps during a historical period of typically a few decades. When historical series are used only to force the model, but no observations of the predicted variables are assimilated during the run, the simulations are referred to as hindcasts; the fields of predicted variables are often validated against the available observations in order to assess the accuracy of the simulation. Finally, when only the radiative forcing is imposed, the model runs freely, without any chronological constraint; the interest of these simulations is the study of the variability from a statistical point of view, which is actually what defines the climate system. These runs are referred to as control simulations when the radiative forcing corresponds to either the pre-industrial period or to present day.

There are different types of numerical ocean models and the choice depends on the processes to be investigated. Barotropic ocean models, for example, represent a vertically integrated ocean. They have proved to be adequate in simulating the response of sea level to the forcing of atmospheric pressure and wind (see e.g. Pascual et al., 2008) and are therefore the basis for short-term operational sea level forecasting, as the atmospheric forcing is by far the dominant component at scales between one day and one month. Conversely, baroclinic ocean models are aimed at simulating the full three-dimensional structure of the ocean. The advantage is that they provide information about depth varying oceanographic variables like temperature and salinity, which can be useful in understanding some of the processes driving sea level variability. However, for operational applications they do not reach the good performance of barotropic models due to the complexity of the processes involved in the simulations (Pérez et al., 2012). Hence, a comparison between various baroclinic hindcasts covering the Mediterranean region has revealed important regional differences (Calafat et al., 2012). Another type of models is given by the wind-wave models, forced only with surface winds and widely used with operational purposes due to their ability to forecast wind-wave conditions. Wind-wave hindcasts providing retrospective information of the wave climate are often biased with respect the observations because of a poor representation of the forcing, limitation of the physics of the model and/or the spatial resolution. This problem can be partially overcome by using wind-wave observations from buoys and/or satellite altimetry to correct the hindcasted output fields. The correction process is commonly called calibration and can be carried out following different methodologies (Caires and Sterl, 2005; Tomas et al., 2008; Mínguez et al., 2011).

Whatever numerical model is used, there is always a trade-off between the resolution (spatial and temporal), the spatial coverage and the time span. The spatial resolution of global models is often too coarse as to include physical processes that can be important for regional climate variability. Therefore, for the forcing of ocean (baroclinic, barotropic or wave) models it is common to increase the spatial resolution of the atmospheric forcing over the area of interest. This process can be carried out either using a regional climate model that includes smaller scales for the physical processes and a high resolution topography (in which case the process is referred to as dynamical downscaling) or through statistical relationships between the global model parameters and regional observations (in which case the process is referred to as statistical downscaling).

In addition to reproduce past and present-day climate variability, numerical models are also a very powerful tool to project future climate under imposed forcing conditions. In these climate simulations, referred to as projections, the forcing fields are derived from Earth's radiative conditions that correspond to plausible changes in CO2 and aerosol emissions based on different future scenarios of social and economic development. A single model run under a single scenario does not suffice to provide realistic projections of climate change for a number of reasons. First, because long term runs of climate models may suffer from biases and drifts, which become evident when the models are forced with a constant forcing over time (the control simulations mentioned above). These drifts can be corrected, at least to some extent, by comparing the projections with the corresponding control simulations. A second reason is that the natural variability superimposed onto climate change signals may have comparable or even larger amplitudes. These natural variations, with yearly to decadal time scales, have arbitrary time phases and therefore they can be expected to cancel out when averaging projections from many different models. Finally, there is also a spread of models outputs even if they are run under the same conditions, due to the different ways in which the physical processes are formulated or parameterized. This altogether makes desirable to use a number as large as possible of individual numerical climate simulations to project future climate conditions, particularly to estimate their uncertainties. It is common practice to compute the ensemble mean and consider it as the best approach to future climate response; the underlying assumptions in this approximation are that the errors of the different models spread more or less randomly around the true values and that the number of simulations is large enough as to cancel out the errors, as it does with the natural variability.

The generation of a large ensemble of model simulations generally requires a high computational effort. However, for some particular variables this limitation can be overcome using reliable statistical approaches. This is the case of the wind-wave climate simulations, for which a vast literature does exist on how to take advantage of the close relationship between wind-waves and atmospheric fields to design statistical models (Wang et al., 2004; Wang and Swail, 2006; Wang et al., 2012; Casas-Prat et al., 2014; Wang et al., 2014). A strong assumption in this type of models is that the relationship found for present-day climate is stationary in time and also holds for other periods under different climate conditions. Atmospheric pressure and winds are the most common predictors in such models, but not the only possible candidates. For example, given the relationship between large scale atmospheric climate indices and temporal variations in wind-wave climate, it seems reasonable to enquire about other possibilities based on these indices.

1.4 Framework, objectives and structure of this thesis

The present thesis has been developed in the framework of two research projects carried out by the Sea Level and Climate research group of the University of the Balearic Islands (http://marine-climate.uib.es). Both projects were aimed at the generation and analysis of regional marine climate scenarios for the Mediterranean Sea and the North-east Atlantic Ocean. The first one, entitled “Development, validation and application of oceanic regional models” (ESCENARIOS) was carried out during 2009-2012 and was an assignment from the Spanish Meteorological Office (AEMET). The second project, entitled “Generation of 21st century marine climate scenarios for the Mediterranean Sea and the Northeast

Atlantic Ocean" (VANIMEDAT2) was funded by the Spanish National Research Program and run during 2010-2013. As a result of the activities developed within these two projects a large number of regional marine climate scenarios including baroclinic, barotropic and wind-wave simulations were generated and analyzed.

This thesis is part of the efforts to characterize the recent and future evolution of the marine climate in the region of interest. Namely, a major part of the work presented here is devoted to the study of the wind-wave fields in the Western Mediterranean Sea and the North Atlantic Ocean. In Chapter 2 we present the calibration of a new wind-wave hindcast of the Western Mediterranean using buoy and altimetry data; the aim was to obtain and describe the best possible representation of the wave climate in this region during the last decades. The next chapters of the thesis focus on the mechanisms underlying the observed marine climate; namely we analyze the impact of the large scale atmospheric modes on the wave and sea level climate. Chapter 3 investigates and quantifies the effect that the dominant climate modes have on Mediterranean sea level and its different contributions, making use of observations from tide gauges, altimetry and hydrography, as well as model output fields. In Chapters 4 and 5 the focus is put on the wind-wave climate of the North Atlantic Ocean. Chapter 4 quantifies the impact of the same large scale climate modes over the current North Atlantic wind-wave regime on the basis of two wave hindcasts and buoy and altimetry observations; the aim is to determine the wind-wave variability that can be explained by the large scale atmospheric forcing. In Chapter 5 the major effort is devoted to the evaluation of different methodologies to project the wind-wave climate of the 21st century, including the use of climate modes together with statistical and dynamical models; the objective here is to determine the strengths and weaknesses of the different approaches evaluated.

This thesis is presented as a collection of research articles, each one addressing specific scientific issues. The state of the art for each of those issues as well as specific methodologies are presented within each chapter. Other works carried out in the framework of the same projects and led by different authors complement those presented here. This is the case of the calibration of a sea level hindcast (Jordà et al., 2012a), the generation and analysis of future sea level scenarios (Marcos and Tsimplis, 2008; Marcos et al., 2011; Jordà et al., 2012b), the quantification of the NAO impact on the Mediterranean sea level (Tsimplis et al., 2013), the evaluation of the coastal sea level rise along the southern European coasts (Woppelmann and Marcos, 2012) or the generation and analysis of future wind-wave scenarios in the Mediterranean Sea (still ongoing), among others. Therefore, this thesis represents a contribution to the overall efforts of the Sea Level and Climate research team to describe the marine climate in the Mediterranean and North Atlantic Ocean.

Bibliography

Araújo, I. B., & Pugh, D. T. (2008). Sea levels at Newlyn 1915-2005: analysis of trends for future flooding risks. Journal of Coastal Research, 24(sp3), 203-212.

Bindoff, N. L., Stott, P. A., AchutaRao, K. M., Allen, M. R. Gillett, N., Gutzler, D., Hansingo, K., Hegerl, G., Hu, Y., Jain, S., Mokhov, I. I., Overland, J., Perlwitz, J., Sebbari R., & Zhang, X. (2013). Detection and Attribution of Climate Change: from Global to Regional. In: Climate Change (2013). The Physical Science Basis. Contribution of Working Group I to the Fifth Assessment Report of the Intergovernmental Panel on Climate Change [Stocker, T.F., Qin, D., Plattner, G.K., Tignor, M., Allen, S. K., Boschung, J., Nauels, A., Xia, Y., Bex V., & Midgley P. M. (eds.)]. Cambridge University Press, Cambridge, United Kingdom and New York, NY, USA.

Brayshaw, D. J., Hoskins, B. & Black, E. (2010). Some physical drivers of changes in the winter storm tracks over the North Atlantic and Mediterranean during the Holocene. Phil. Trans. R. Soc. A 368, 5185–5223.

Burrows, MT., Harvey, R., & Robb,. L. (2008). Wave exposure indices from digital coastlines and the prediction of rocky shore community structure. Mar Ecol Prog Ser 353:1–14.

Caires, S., & Sterl, A. (2005). A new non parametric method to correct model data: application to significant wave height from the ERA-40 re-analysis. J. Atmos. Ocean. Technol. 22,443–459.

Calafat, F.M., & Gomis, D. (2009). Reconstruction of Mediterranean Sea level fields for the period 1945–2000. Global and Planetary Change 66 (3–4), 225–234.

Calafat, F.M., Jordà, G., Marcos, M., & Gomis, D. (2012). Comparison of Mediterranean sea level variability as given by three baroclinic models, J. Geophys. Res., 117, C02009.

Casas-Prat M., Wang, X. L. & Sierra, J. P. (2014). A physical-based statistical method for modeling ocean wave heights. Ocean Model, 73:59–75

Cazenave, A., Llovel, W. (2010). Contemporary Sea Level Rise. Annu. Rev. Mar. Sci. 2010. 2:145–73. 10.1146/annurev-marine-120308-081105.

Chen, G., Chapron, B., Ezraty, R., & Vandemark, D. (2002). A global view of swell and wind sea climate in the ocean by satellite altimeter and scatterometer. Journal of Atmospheric and Oceanic Technology, 19(11), 1849-1859.

Church, J.A., Clark, P.U., Cazenave, A., Gregory, J.M., Jevrejeva, S., Levermann, A., Merrifield, M.A., Milne, G.A., Nerem, R.S., Nunn, P.D., Payne, A.J., Pfeffer, W.T., Stammer, D., & Unnikrishnan, A.S. (2013). Sea Level Change. In: Climate Change 2013: The Physical Science Basis. Contribution of Working Group I to the Fifth Assessment Report of the Intergovernmental Panel on Climate Change [Stocker, T.F., Qin, D., Plattner, G.K., Tignor, M., Allen, S. K., Boschung, J., Nauels, A., Xia, Y., Bex V., & Midgley P. M. (eds.)]. Cambridge University Press, Cambridge, United Kingdom and New York, NY, USA.

Gomis, D., Tsimplis, M.N., Martín-Míguez, B., Ratsimandresy, A.W., García-Lafuente, J., & Josey, S.A. (2006). Mediterranean Sea level and barotropic flow through the Strait of Gibraltar for the period 1958–2001 and reconstructed since 1659. Journal of Geophysical Research 111, C11005.

Gomis, D., Ruiz, S., Sotillo, M. G., Álvarez-Fanjul, E., & Terradas, J. (2008). Low frequency Mediterranean sea level variability: the contribution of atmospheric pressure and wind. Global and Planetary Change, 63(2), 215-229.

Hay, C. C., Morrow, E., Kopp, R. E. & Mitrovica, J. X. (2015). Probabilistic reanalysis of twentieth-century sea-level rise. Nature. 517, 481-484.

Hurrell, J.W., & Deser, C. (2009). North Atlantic climate variability: The role of the North Atlantic Oscillation. J. Mar. Syst. 359 78, 28–41.

Isemer, H. J., & Hasse, L. (1985). The Bunker climate atlas of the north Atlantic Ocean. Springer Science & Business Media.

Jordà, G., Gomis, D., & Álvarez-Fanjul, E. (2012a). The VANI2-ERA hindcast of sea level residuals: Atmospheric forcing of sea level variability in the Mediterranean Sea (1958-2008). Scientia Marina (in press).

Jorda, G., Gomis, D., Alvarez-Fanjul, E., & Somot, S. (2012b). Atmospheric contribution to Mediterranean and nearby Atlantic sea level variability under different climate change scenarios. Global and Planetary Change, 80-81, 198–214.

Josey, S.A., Somot, S., & Tsimplis, M. (2011). Impacts of atmospheric modes of variability on Mediterranean sea surface heat exchange. J. Geophys. Res. 116, C02032.

Landerer, F. W., & Volkov, D. L. (2013). The anatomy of recent large sea level fluctuations in the Mediterranean Sea, Geophys. Res. Lett., 40, 553–557.

Marcos, M., & Tsimplis, M.N. (2008). Coastal sea level trends in southern Europe. Geophysical Journal International 175 (1), 70–82.

Marcos, M., Jordà, G., Gomis, D., & Pérez, B. (2011). Changes in storm surges in southern Europe from a regional model under climate change scenarios Global and Planetary Change, 77 (3-4), 116-128.

Marcos, M., Tsimplis, M. N., & Shaw, A. G. P. (2009). Sea level extremes in southern Europe, J. Geophys. Res., 114, C01007.

McGranahan, G., Balk, D., & Anderson, B. (2007). The rising tide: Assessing the risks of climate change and human settlements in low elevation coastal zones, Environ. Urban., 19(1), 17–37.

Menéndez, M., & Woodworth, P. L. (2010). Changes in extreme high water levels based on a quasi-global tide-gauge data set, J. Geophys. Res., 115, C10011.

Mínguez, R., Espejo, A., Tomás, A., Méndez, F.J., & Losada, I.J. (2011). Directional calibration of wave reanalysis databases using instrumental data. J. Atmos. Ocean. Technol. 28, 1466–1485.

Pascual, A., Marcos, M., & Gomis, D. (2008). Comparing the sea level response to pressure and wind forcing of two barotropic models: validation with tide gauge and altimetry data. J. Geophys. Res., 113, C07011.

Pérez, B., Brouwer, R., Beckers, J., Paradis, D., Balseiro, C., Lyons, K., Cure, M., Sotillo, M. G., Hackett, B., Verlaan, M., & Fanjul, E. A. (2012). ENSURF: Multi-model sea level forecast. Implementation and validation results for the IBIROOS and Western Mediterranean regions. Ocean Science 8: 211–226.

Semedo, A., Sušelj, K., Rutgersson, A., & Sterl, A. (2011). A global view on the wind sea and swell climate and variability from ERA-40. Journal of Climate,24(5), 1461-1479.

Sorenson, R. M., Weisman, R. N., & Lennon, G. P. (1984). "Control of Erosion, Inundation and Salinity Intrusion Caused by Sea Level Rise" in Greenhouse Effect and Sea Level Rise, Barth and Titus (eds), Van Nostrand Reinhold Company, Inc.

Stammer, D., Cazenave, A., Ponte, R. M. & Tamisiea, M. E. (2013). Causes for Contemporary Regional Sea Level Changes. Annu. Rev. Mar. Sci. 2013. 5:21–46.

Timm, O., Ruprecht, E., & Kleppek, S. (2004). Scale-dependent reconstruction of the NAO index. J Clim 17(11):2157–2169

Tomas, A., Méndez, F., & Losada, I. (2008). A method for spatial calibration of wave hindcast data bases. Cont. Shelf Res. 28, 391–398.

Trigo, I. F., Bigg, G. R., & Davies, T. D. (2002). Climatology of cyclogenesis mechanisms in the Mediterranean. Monthly Weather Review, 130(3), 549-569.

Tsimplis, M. N. & Baker, T. F. (2000). Sea level drop in the Mediterranean Sea: an indicator of deep water salinity and temperature changes?, Geophys. Res. Lett., 27(12), 1731–1734.

Tsimplis, M. N., & Josey, S. A. (2001). Forcing of the Mediterranean Sea by atmospheric oscillations over the North Atlantic. Geophysical Research Letters 28 (5), 803–806.

Tsimplis, M. N., Álvarez-Fanjul, E., Gomis, D., Fenoglio-Marc, & L., Pérez, B. (2005). Mediterranean Sea level trends: atmospheric pressure and wind contribution, Geophys. Res. Lett., 32, L20602.

Tsimplis, M. N., Calafat, F. M., Marcos, M., Jordà, G., Gomis, D., Fenoglio-Marc, L., Struglia, M. V., Josey, S. A. & Chambers, D. P. (2013). The effect of the NAO on sea level and on mass changes in the Mediterranean Sea, J. Geophys. Res. Oceans, 118.

Wang X. L. L., Zwiers, F. W., & Swail, V. R. (2004). North Atlantic ocean wave climate change scenarios for the twenty-first century. J Clim 17:2368–2383

Wang, X. L., & Swail, V. R. (2006). Climate change signal and uncertainty in projections of ocean wave heights. Clim. Dyn., 26, 109–126.

Wang, X. L., Feng, Y., & Swail, V. R. (2012). North Atlantic wave height trends as reconstructed from the twentieth century reanalysis, Geophys. Res. Lett., 39, L18705.

Wang X. L, Feng, Y., & Swail, V. R. (2014). Changes in global ocean wave heights as projected using multimodel CMIP5 simulations. Geophys Res Lett 41(3):1026–1034

Weisse, R., & von Storch, H. (2010), Marine Climate and Climate Change: Storms, Wind Waves and Storm Surges, 200 pp., Springer, New York.

Wöppelmann, G., & Marcos, M. (2012), Coastal sea level rise in southern Europe and the nonclimate contribution of vertical land motion, J. Geophys. Res., 117, C01007.

Wöppelmann, G., Marcos, M., Coulomb, A., Martín Míguez, B., Bonnetain, P., Boucher, C., Gravelle, M., Simon, B., Tiphaneau P. (2014). Rescue of the historical sea level record of Marseille (France) from 1885 to 1988 and its extension back to 1849–1851. J Geod (2014) 88:869–885

Young, I. R., Ziegler, S., & Babanin, A. V. (2011). Global trends in wind speed and wave height, Science, 332, 451–455.

Chapter 2

Calibration of a new wind-wave hindcast in the Western Mediterranean

— Existe una cosa muy misteriosa, pero muy cotidiana. Todo el mundo participa de ella, todo el mundo la conoce, pero muy pocos se paran a pensar el ella. Casi todos se limitan a tomarla como viene, sin hacer preguntas. Esta cosa es el tiempo.

— Life holds one great but quite commonplace mystery. Though shared by each of us and known to all, it seldom rates a second thought. That mystery, which most of us take for granted and never think twice about, is time.

Michael Ende, Momo (1973)

This chapter has been published in:

- Martinez-Asensio, A., Marcos, M., Jorda, G., Gomis, D., 2013. Calibration of a new wind-wave hindcast in the Western Mediterranean. Journal of Marine Systems 121–122, 1–10.

Abstract

Wave climate in the Western Mediterranean is presented through the calibration of an update wind wave hindcast spanning the period 1958-2008. The hindcast was obtained with the WAM model (spatial resolution of 1/6º) forced with wind fields from the atmospheric model ARPERA. Significant wave heights (SWH) provided by the hindcast were calibrated using buoy observations with the aim of improving the characterization of the wave climate over the region. The methodology is based on a spatial calibration of the statistical distribution of SWH performed through a non-linear transformation of the Empirical Orthogonal Functions of the modelled data that minimizes the differences with observations. This allows the calibration to be implemented not only at buoy locations, but all

over the model domain. The resulting fields were validated against satellite altimetry observations, showing an average reduction of about 76% in the bias and of about 10% in the root mean squared differences with respect to observations.

2.1 Introduction

The study and characterization of wind wave climate is a very relevant issue in coastal design and protection strategies (Mínguez et al., 2011). Most approaches aimed to the characterization of the wave climate of a given region combine field observations from marine buoys (located either at coastal or deep waters) and/or altimetric observations with the use of numerical wind wave hindcasts (see e.g. Cavaleri and Bertotti, 2004; Caires and Sterl, 2005; Cavaleri and Sclavo, 2006; Tomás et al., 2009; Mínguez et al. 2011). While buoys provide high frequency time series at a limited number of locations, altimetry provides a more complete spatial coverage but with a much smaller sampling frequency (typically with a revisiting period between 10 and 30 days). Regarding the time coverage, buoy records typically span from a few years to a few tens of years (sometimes with significant data voids) and are usually consistent throughout the spanned period. Altimetry time series of wave observations along the satellite tracks are available since the 1980s; however, unlike for sea level, for instance, the distinct characteristics and paths of the different satellites altogether with the high temporal variability of the wave field prevent the mapping of the wave field regularly in time.

Numerical models are especially useful in areas where measurements are not available. In addition to a complete and regular spatial coverage they provide continuous high-frequency records that can span several decades. However, wave hindcasts also have major shortcomings. Probably the most important one is that they are often biased with respect to observations because of a poor representation of the forcing wind fields, limitation in the physics of the model and/or the low spatial resolution of the forcing and/or the wave model (Feng et al., 2006).

In order to overcome, or at least to reduce, the limitations of wave hindcasts, the output fields can be calibrated against measurements. Several methodologies aimed at correcting simulated waves through different transformations are described in the literature. Caires and Sterl (2005) proposed a non-parametric method to correct significant wave height (SWH) from the global ERA-40 re-analysis using both altimetric and buoy measurements. Their methodology was based on the error estimation from “analogs” or “learning” data sets, which conditions the comparisons to the existence of such learning periods. In a different approach, Janssen et al. (2007) used simultaneous collocated global observations of buoys and altimetry altogether with a model output with data assimilation to estimate the errors on SWH. Assuming that individual errors are uncorrelated, their estimations were then combined to calibrate the datasets. In the Mediterranean Sea, Cavaleri and Sclavo (2006) combined buoys, altimetry and model data to calibrate modelled wind and wave fields.

A common feature of the methodologies reported above is that all them apply single point calibrations and are therefore limited by the spatial distribution of observations. Instead, Tomas et al. (2008) followed a different approach, based on finding the transformation of the statistical distribution of the hindcasted wave heights at each grid point that best fits the distributions derived from buoy measurements. The implicit assumptions are that SWH follow a given model distribution everywhere in the domain (with different model parameters at different points) and that the parameters of the statistical model vary smoothly in space. This method was further extended by Mínguez et al. (2011) to account for different wave directions and to pay special attention to extreme values by minimizing the differences between quartiles instead of minimizing the parameters of the statistical distribution.

In the present work we calibrate the SWH of a recently released wind wave hindcast in the Western Mediterranean spanning the last five decades (1958-2008). To perform the calibration we followed the methodology proposed by Tomas et al. (2008). A major difference with respect to the reference work is the extension of the spatial and temporal coverage of our calibration: Tomas et al. (2008) focused on a region around the Balearic Islands, while we apply the methodology to the entire Western Mediterranean basin. Furthermore, the updated hindcast used here spans more recent years, which implies that a larger number of buoys with recent observations can be included in the calibration process, and has been validated against all the available observations from satellite altimetry for the period 1992-2008 as independent data. The enlargement of the spatial and temporal coverage also allows us to get more insight on the capabilities and limitations of the methodology.

The paper is organized as follows: in section 2 we describe the wave hindcast and the buoys and altimetric observations used for the calibration and validation. In section 3 we present the methodology of the calibration method. Results and validation are presented in section 4 and discussed in section 5, paying particular attention to the robustness of the solution.

2.2 Data sets

2.2.1 Buoy observations

Wave observations from several buoy networks deployed in the Western Mediterranean Sea were collected from different data providers. The mean depth of the storm wave base (the lowest level at which the motion associated with wind waves is significant) has been estimated in 20-25 m in the Mediterranean Sea (Hernández-Molina et al., 2000). This means that buoys located over shallower water depths could be measuring waves disturbed by the local bathymetry and therefore not to be representative of the large-scale wave field. To avoid such problems, only the 22 buoys located over water depths greater than 50 m were selected (Fig. 2.1 and Table 2.1). Buoy data along the southern and eastern Spanish coasts and around the Balearic Islands (stations numbers 13-20 in Table 2.1) were provided by Puertos del Estado (www.puertos.es), whereas those in the northeastern Spanish coast (numbers 21-22) were obtained from the observational network of the Catalan Government (*Xarxa d'Instruments Oceanogràfics i Meteorològics*, http://www.xiom.cat). Observations from French stations were made available through the *Centre d'Archivage National de Donnés de Houle In Situ* (CANDHIS, http://candhis.cetmef.Developpement-durable.gouv.fr, numbers 1-4) and through the French National Meteorological Service (METEO-FRANCE, http://france.meteofrance.com, number 5). Finally, buoys located along the Italian coasts (numbers 6-12) were obtained from the *Istituto Superiore per la Protezione e la Ricerca Ambientale* (ISPRA, http://www.idromare.it).

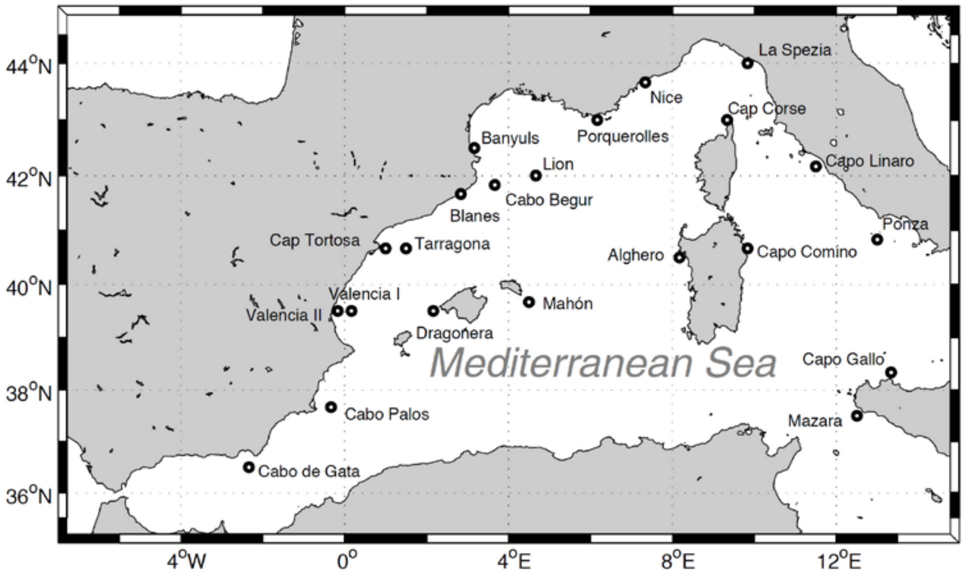

Figure 2.1. Location of the buoys used for the calibration of the Western Mediterranean wind wave hindcast.

The spatial distribution of the buoys is biased towards the northern shores of the basin, with a clear lack of data in the southern shores (Fig. 2.1). The location of the stations, the water depth at the deployment location and the period of operation are all listed in Table 2.1. The length of the time series varies between 1 and 20 years. The buoy data set includes the main wave parameters, namely SWH, mean period and peak period, as well as directional information. The percentage of data gaps for two of the main parameters (SWH and wave direction) has also been quoted in Table 2.1. Sampling rates vary among buoys and also among different time periods for the same instrument, ranging from 30 min to 3h. All time series were homogenized towards a common temporal resolution of 3 h before being used for the calibration.

Table 2.1. Buoy stations with location, water depth, period of operation and percentages of gaps in the SWH and direction records. The wave direction was not available for stations 1-5. The location and distance to the closest model grid point is also listed.

Buoys							Closest grid point	
N	Station	Location (º)	Depth (m)	Period	SWH Gaps (%)	DIR Gaps (%)	Location (º)	Distance (km)
1	Cap Corse	43.06 N 09.27 E	140	Mar-99 / Aug-11	51.4	-	43.00 N 9.33 E	8.27
2	Banyuls	42.48 N 03.16 E	50	Nov-07 / Aug-11	4.5	-	42.50 N 3.17 E	1.17
3	Porquerolles	42.96 N 06.20 E	90	May-92 / Aug-11	32.7	-	43.00 N 6.17 E	4.83
4	Nice	43.63 N 07.22 E	270	Jun-02 / Dec-10	33.48	-	43.67 N 7.17 E	9.09
5	Lion	42.06 N 04.64 E	250	Dec-01 / Dec-08	14.56	-	42.00 N 4.67 E	7.04
6	Mazara	37.51 N 12.53 E	85	Jul-89 / Apr-08	14.74	14.74	37.50 N 12.50 E	3.77
7	Capo Gallo	38.26 N 13.33 E	145	Jan-04 / Mar-08	23.9	23.9	38.33 N 13.33 E	8.16
8	Capo Comino	40.61 N 09.88 E	130	Jan-04 / Sep-05	20.64	20.64	40.67 N 9.83 E	7.24
9	Alghero	40.54 N 08.10 E	85	Jul-89 / Apr-08	8.33	8.33	40.50 N 8.17 E	7.09
10	Ponza	40.86 N 12.95 E	115	Jul-89 / Mar-08	13.18	13.18	40.83 N 13.00 E	5.6
11	Capo Linaro	42.24 N 11.55 E	62	Jan-04 / Sep-06	32.07	32.07	42.17 N 11.50 E	9.24
12	La Spezia	43.92 N 09.82 E	85	Jul-89 / Mar-07	15.26	15.26	44.00 N 9.83 E	8.47
13	Dragonera	39.55 N 02.10 E	135	Nov-06 / Oct-10	9.7	9.7	39.50 N 2.17 E	8.28
14	Cabo de Palos	37.65 N 00.32 W	230	Jul-06 / Aug-11	4.8	4.8	37.67 N -0.33 W	1.87
15	Valencia I	39.46 N 00.26 E	260	Aug-04 / Sep-05	2.6	2.6	39.50 N 0.33 E	9.29
16	Valencia II	39.52 N 00.21 W	50	Sep-05 / Nov-08	12.6	12.6	39.50 N 0.17 E	5.31
17	Mahón	39.71 N 04.44 E	300	Apr-93 / Aug-11	27.02	27.02	39.67 N 4.50 E	7.61
18	Cabo de Gata	36.56 N 02.33 W	536	Mar-98 / Jun-11	65.79	65.79	36.50 N -2.33 W	7.75
19	Tarragona	40.68 N 01.46 E	688	Aug-04 / Aug-11	12.13	12.13	40.67 N 1.50 E	3.58
20	Cabo Begur	41.91 N 03.64 E	1200	Apr-01 / Aug-11	45.36	45.36	41.83 N 3.67 E	9.3
21	Cap de Tortosa	40.72 N 00.98 E	60	May-84 / Aug-11	21.02	21.02	40.67 N 1.00 E	6.29
22	Blanes	41.64 N 02.81 E	74	May-84 / Aug-11	36.68	95.05	41.67 N 2.83 E	2.66

2.2.2 Satellite altimetry observations

Along-track SWH observations with high resolution sampling from satellite altimetry processed and distributed by AVISO (http://www.aviso.oceanobs.com/) were used in the validation. Data from seven altimeters were collected with various spatial and temporal resolutions: Jason-1 (J1), Jason-2 (J2), Topex/Poseidon (TP), European Remote Sensing (ERS-1 and ERS-2), Envisat (EN), and Geosat Follow On (G2). This data set covers sixteen complete years from October 1992 through December 2008. For the detection and removal of anomalous values, a 3σ test was applied, i.e., data with a SWH value larger than 3 times the standard deviation of each satellite track were removed (Queffeulou and Bentamy, 2007). Observations from multisatellite missions need to be combined and homogenized in order to generate a consistent data set (Cotton and Carter, 1994; Challenor and Cotton, 2002; Queffeulou, 2004). Updated corrections outlined in Queffeulou and Croizé-Fillon (2011), obtained from the comparison of altimetric SHW with buoy data as described in Queffeulou (2004), were applied here.

2.2.3 The Wave hindcast

The wind wave hindcast was performed with the WAM model (WAMDI, 1988), a third generation wave model that explicitly solves the wave transport equation. The three source terms (wind input, non-linear energy transfer and white capping dissipation) are explicitly prescribed and integrated using an implicit second order centred differencing scheme. For the propagation term, a first order upwind scheme is applied. More details on the model can be found in WAMDI (1988) or Günther et al. (1992). In the framework of this work, the model has been implemented in the Western Mediterranean (from the Strait of Gibraltar to 17º E) with a spatial resolution of 1/6º (3398 grid points). The model configuration is the same used by Ratsimandresy et al. (2008) to generate the HIPOCAS wave hindcast and the same implemented in the operational wave forecasting system of Puertos del Estado. The wind forcing was obtained from the ARPERA hindcast (Herrmann and Somot, 2008; Jordà et al., 2012), a dynamical downscalling of the ERA40 reanalysis. 10-m winds provided by ARPERA have a temporal resolution of 6 hours, a spatial resolution of ~50km and cover the period 1958-2008. The WAM output parameters are stored every 3 hours and include SWH, wave direction, mean period and peak period.

The grid points of the model closest to each buoy were selected for a first comparison with observations. Their location and distance to the corresponding buoys are listed in Table 2.1. Figure 2.2 shows two representative examples of the comparison between SWH given by the model and buoy observations; both cover a period of 3 months and have been plotted with a temporal sampling of 3 h. While the temporal variability is well captured by the model, model values show an overall underestimation of the observed magnitude of SWH. A similar behaviour is obtained at most locations. Correlation and Root Mean Squared (RMS) differences between the observations and the output of the model at the closest grid points were computed for the overlapping periods. Results, listed in Table 2.2, reveal correlations ranging between 0.70 and 0.94 and being statistically significant in all cases. RMS differences show a higher dispersion among sites, ranging between 0.24 and 0.65 m.

2.3 Methodology of the wave model calibration

The aim of the calibration is to reduce the differences between the SWH hindcasted by the model and the available buoy observations. The major advantage of the method, developed by Tomas et al. (2008), is that it allows the calibration of the whole domain using time series observed at a limited number of points. The assumptions inherent to the method are that SWH follow the same statistical model everywhere in the domain and that the parameters of the statistical model vary smoothly in space. The methodology is summarized in the following for the sake of completeness.

2.3.1 Statistical distribution of SWH

SWH time series corresponding to every grid point of the model (hindcasted SWH) and to buoy records (observed SWH) were monthly aggregated and fitted to a log-normal distribution (Holthuijsen, 2007) whose density function is defined as:

$$f(SWH) = \frac{1}{SWH\sigma\sqrt{2\pi}} \exp\left(\frac{-\left(\ln SWH - \mu\right)^2}{2\sigma^2} \right) \tag{1.1}$$

where μ and σ^2 are the location and scale parameters of the distribution, respectively. In our application, the random variable of the distribution is SWH expressed in meters (though it is treated as a non-dimensional variable in the formulation; if other units were used μ would have a different value, while σ^2 would keep the same value). The separation of the distribution into calendar months is due to the strong seasonal character of the wave properties.

The goodness of the fit was checked for both observations and model data (in the latter case at the grid points closest to the buoy locations). Figure 2.3 shows an example for the buoy of Nice and the months of July and January, which are

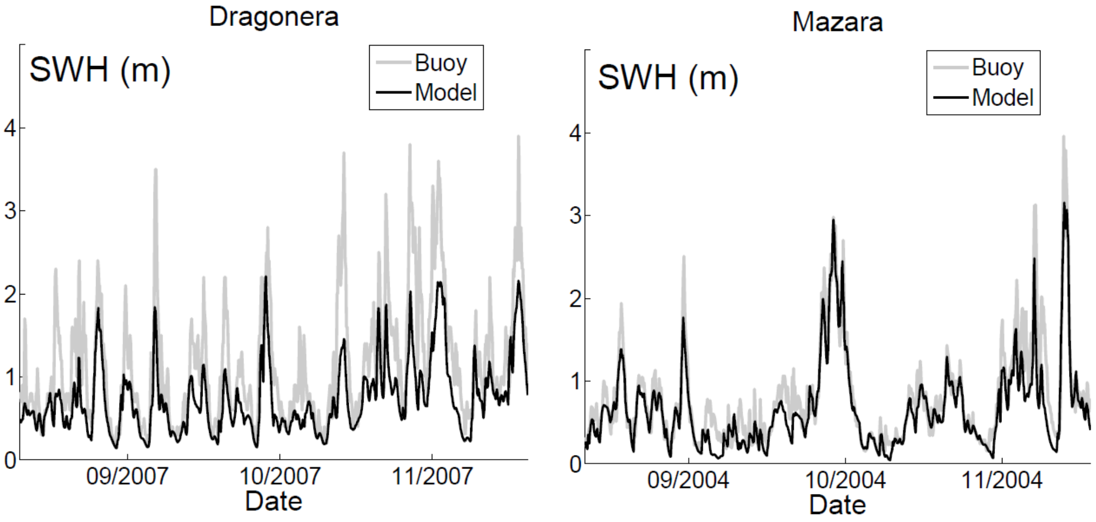

Figure 2.2. Time series of significant wave height at Mazara and Dragonera buoys (grey line) and at the closest gridpoint of the hindcast (black lines). Units are meters.

representative of summer and winter conditions. The plots reveal that the mean regimes of SWH follow the log-normal distribution in both seasons, while extreme values depart significantly from the theoretical model. A related consequence is that the calibration is expected to work properly for the mean regimes (which represents a very large percentage of the time period), but might not do so for extreme events.

Following Tomas et al. (2008), the mean (M) and variance (V) (non-dimensional) parameters of the log-normal distribution can be expressed in terms of the location and scale parameters as:

$$M(x,\tau) = \exp\left(\frac{\mu+\sigma^2}{2}\right)$$

$$V(x,\tau) = \exp\left(2\mu+\sigma^2\right)\left\{\exp\left(\sigma^2\right)-1\right\} \tag{1.2}$$

where it is recalled that all parameters, and therefore M and V, are a function of the location x and of the calendar month τ. For hindcasted values, x runs over the discrete number of grid points, while for the buoys it indicates the location of the buoy. In both cases τ runs from 1 to 12.

Figure 2.4 shows the spatial distributions of the parameters M and V for January and July (i.e., M, V(x, $\tau = 1$) and M,V(x, $\tau = 7$)) obtained from the

Table 2.2. Correlations, RMS differences and bias between modelled (non-calibrated and calibrated) and observed SWH. Buoys for which the RMS difference between the calibrated values and observations is larger than for the non-calibrated values are marked with an asterisk.

Station	Correlation	RMS (m) non-calibrated	RMS (m) calibrated	BIAS (m) non-calibrated	BIAS (m) calibrated
Cap Corse	0.82	0.63	0.53	-0.34	-0.12
Banyuls*	0.86	0.33	0.41	-0.02	0.18
Porquerolles	0.85	0.48	0.4	-0.28	-0.04
Nice*	0.82	0.39	0.44	-0.05	0.12
Lion	0.93	0.28	0.25	-0.22	-0.08
Mazara	0.91	0.3	0.29	-0.15	-0.1
Capo Gallo*	0.93	0.24	0.27	-0.07	0.15
Capo Comino	0.89	0.35	0.29	-0.15	-0.02
Alghero	0.93	0.47	0.38	-0.34	-0.09
Ponza	0.89	0.41	0.35	-0.18	-0.03
Capo Linaro	0.87	0.48	0.42	-0.18	-0.02
La Spezia	0.91	0.58	0.45	-0.27	-0.09
Dragonera	0.89	0.47	0.36	-0.29	-0.06
Cabo de Palos	0.89	0.34	0.27	-0.2	-0.03
Valencia I*	0.76	0.4	0.47	0.03	0.02
Valencia II	0.88	0.41	0.31	-0.17	0
Mahón	0.91	0.32	0.27	-0.2	-0.07
Cabo de Gata*	0.9	0.29	0.31	-0.1	0.16
Tarragona	0.89	0.39	0.29	-0.21	-0.01
Cabo Begur	0.94	0.29	0.25	-0.2	-0.06
Cap de Tortosa	0.74	0.65	0.53	-0.27	-0.1
Blanes	0.7	0.51	0.51	-0.1	0.07
MEAN	0.86	0.41	0.37	-0.18	-0.04

hindcast. The parameters show a smooth behaviour over the entire domain, which is one of the assumptions of the method. For both, M and V, maximum values are restricted to the North central basin in July and occupy the whole central part of the basin in January.

2.3.2 The calibration process

The calibration bases on a transformation of the monthly spatial distributions of the M and V fields in such a way that: i) they better fit the M and V parameters of the log-normal distributions obtained from observations at buoy locations; and ii) the calibrated M and V fields keep the same spatial correlation pattern than the non-calibrated hindcast. This can be achieved by applying first an Empirical Orthogonal Function (EOF) analysis to both the M(x, τ) and V(x, τ) fields and subsequently decomposing them into a set of spatial modes and their associated temporal amplitudes in the way:

$$Y(x,\tau) = \overline{f_Y(x)} + A_1(\tau)f_1(x) + A_2(\tau)f_2(x) + \ldots + A_N(\tau)f_N(x) \tag{1.3}$$

where Y is either M or V, $\overline{f_Y(x)}$ is the time-averaged field, $f_1(x),\ldots, f_N(x)$ are the spatial modes and $A_1(\tau),\ldots, A_N(\tau)$ are the corresponding temporal amplitudes. N is the number of modes, which is equal to the smallest dimension of the singular value decomposition problem. In our case, the temporal dimension (the 12 calendar months) is smaller than the spatial dimension (the number of model grid points), so that N is equal to 12.

An important question is how many of the N modes must be considered. On one hand, the variance accounted for by the representation (1.3) formally increases with the number of considered modes. On the other hand, part of that variance is likely due to errors and to local (spatially uncorrelated) features, so that eliminating high order modes (those with the smallest spatial correlation) usually results in an improvement of the field representation. Conventional tests of statistical significance such as those described by Overland and Preisendorfer (1982) or North et al. (1982) can help to make a decision, but beyond such tests the key problem is identifying the modes that contribute significantly to the spatial coherence at horizontal scales that can be resolved unambiguously from

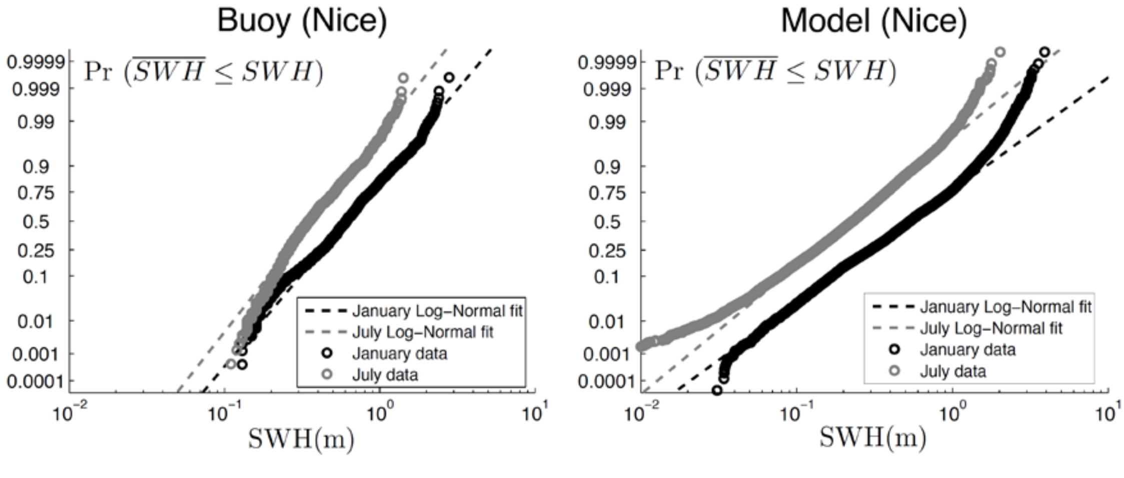

Figure 2.3. Empirical (dots) and fitted (straight line) log-normal distributions computed for the buoy located at Nice (France) and for the closest grid point of the model using January (black) and July (grey) data.

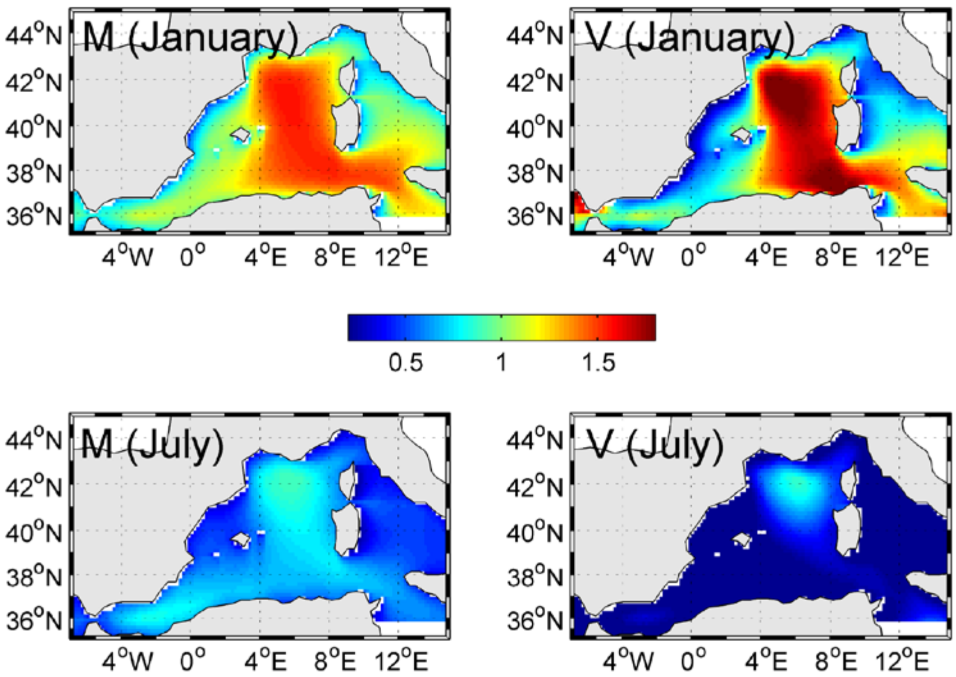

Figure 2.4. Map of the mean (M) and variance (V) parameters of the log-normal distributions fitted to January and July hindcasted data.

the given distribution of observations. After several tests we decided to use 4 modes (plus the mean field), which altogether account for 99.81% and 99.33% of the field variance of M and V, respectively.

The transformation from the non-calibrated to the calibrated representation bases on a linear and potential parameterization of the mean and variance fields as follows:

$$Y_c(x,\tau) = a_0\,\overline{f_Y(x)}^{b_0} + a_1 A_1(\tau)\left|A_1(\tau)\right|^{b_1-1} f_1(x) + a_2 A_2(\tau) f_2(x) + \\ + a_3 A_3(\tau) f_3(x) + a_4 A_4(\tau) f_4(x) \qquad (1.4)$$

where Yc is the calibrated field and the coefficients a_0, a_1, a_2, a_3, a_4 , b_0 and b_1 are to be determined by imposing the minimization of the differences between the $Y_B(x_i, \tau)$ values inferred from buoy measurements and the modelled values at their closest grid point. The role of the lineal coefficients a_0, a_1, a_2, a_3 and a_4 is to increase or decrease the relative importance of the terms in which $Y(x, \tau)$ is decomposed. Thus coefficient a_0 modifies the time-averaged field, while a_1, a_2, a_3 and a_4 modify each of the considered modes. Because a linear transformation is usually not enough to significantly improve the calibration, exponential coefficients (b_0 and b_1) are also introduced. The first coefficient, b_0, acts only on the time-averaged field, so that it distorts (either enhancing or smoothing) the spatial variability of the field. Conversely, the second coefficient, b_1, acts on the temporal amplitude of the leading mode, which accounts for 98% of the variance of the field. It is applied in such a way that the sign of the amplitude $A_1(\tau)$ is always preserved. Subsequent modes account for much smaller percentages of the field variance and therefore only the linear correction is applied. That is, further corrections such as the exponential coefficient used for the leading EOF can be considered of second order when applied to higher order modes.

The function to be minimized is expressed as:

$$J(a_0,a_1,a_2,a_3,a_4,b_0,b_1)=\sum_{i=1}^{Nb}\sum_{j=1}^{12}\left[\frac{Y_B(x_i,\tau_j)-Y_C(x_i,\tau_j)}{\overline{Y_B(x_i)}}\right]^2 \qquad (1.5)$$

where N_b is the number of buoys used for the calibration and the top line denotes time averaging.

Once the calibrated fields $M_C(x, \tau)$ and $V_C(x, \tau)$ were obtained, the next step was to transform the time series of the original hindcast in such a way that the modified time series had mean values and variances equal to $M_C(x, \tau)$ and $V_C(x, \tau)$. To do so, at each grid point x two sets of 50 random time series of 10 years each with a 3-hour sampling rate and following the log-normal distribution were generated, the first set using the parameters $M_C(x, \tau)$ and $V_C(x, \tau)$ and the second set using the non-calibrated parameters $M(x, \tau)$ and $V(x, \tau)$. For each grid point and series the percentiles between the 20th and the 99.5th with a step of –log(-log($\Pr(\overline{SWH} \le SWH)$)) (that is, 25 values with separations ranging from 10 to 0.01) were computed and afterwards averaged over the 50 records for both the calibrated and non-calibrated series. Finally, the relationship between the averaged percentiles of the calibrated ($\mathbf{Pr}_n^{Cal}$) and non-calibrated ($\mathbf{Pr}_n$) time series was assumed to be of the form:

$$\Pr_n^{Cal} = A(x)\,\Pr_n^{\;B(x)} \qquad (1.6)$$

which is a linear relationship in a logarithmic scale. The set of parameters $A(x)$, $B(x)$ will be those used to transform the SWH series of the original hindcast $SWH(x,t)$ into the calibrated series $SWH^{Cal}(x,t)$:

$$SWH^{Cal}(x,t) = A(x)\left[SWH(x,t)\right]^{B(x)} \qquad (1.7)$$

Alternatively, the values of $A(x)$, $B(x)$ could be inferred analytically, by imposing that a log-normal distribution with parameters $M(x, \tau)$ and $V(x, \tau)$ turns into a distribution with parameters $M_C(x, \tau)$ and $V_C(x, \tau)$. This was however discarded due to the complexity of the analytical expressions.

A worth noting feature is that the last percentile used for the calibration is the

99.5^{th}. The reason for discarding higher percentiles is to avoid the influence of extreme events (which have been shown not to follow a log-normal distribution) on the fit.

2.4. Results

1.4.1 The calibrated hindcast

The values of the calibration parameters that minimize expression (1.5) when the 22 buoys from Table 2.1 were used are listed in Table 2.3 for the M and V fields. Examples of the observed, the non-calibrated and the calibrated monthly M and V values are shown in Fig. 2.5 for three buoys, namely Cabo de Palos (station 14), Mahón (station 17) and Nice (station 4). In order to make the modelled and observed parameters directly comparable, the observed M and V have been scaled to the period covered by the model. To do so, the modelled M and V have been first computed for both the entire (M_{model} and V_{model}) and the overlapping (M_{model}^{over} and V_{model}^{over}) periods; then the observed M and V have been multiplied by the ratios M_{model} /M_{model}^{over} and V_{model} /V_{model}^{over}, respectively. In the first two stations, Cabo de Palos and Mahón, the calibrated M and V values are closer to the observed ones than the non-calibrated values. This is especially true for the mean value M, which indicates that the calibration method is able to solve a clear problem of the hindcast: the underestimation of observed SWH (reflected in the bias quoted in Table 2.2).

The improvement is less important for the variance V, indicating that the part of the RMS that is not due to the bias can only be partially overcome by modifying the log-normal distribution. At Nice the result is the opposite: the calibrated values display slightly larger RMS differences with respect to observations than the non-calibrated values. Those stations where the calibration does not improve the hindcast in terms of RMS have been marked with an asterisk in Table 2.2. A common feature of such stations is that the bias of the non-calibrated hindcast is very small (see Table 2.2).

Table 2.3. Calibration parameters obtained for the mean (Mc) and variance (Vc) fields.

	a_0	a_1	a_2	a_3	a_4	b_0	b_1
Mc	1.26	0.33	1.69	2.02	-0.11	0.96	1.42
Vc	0.92	1.16	0.30	0.90	0.88	0.92	0.87

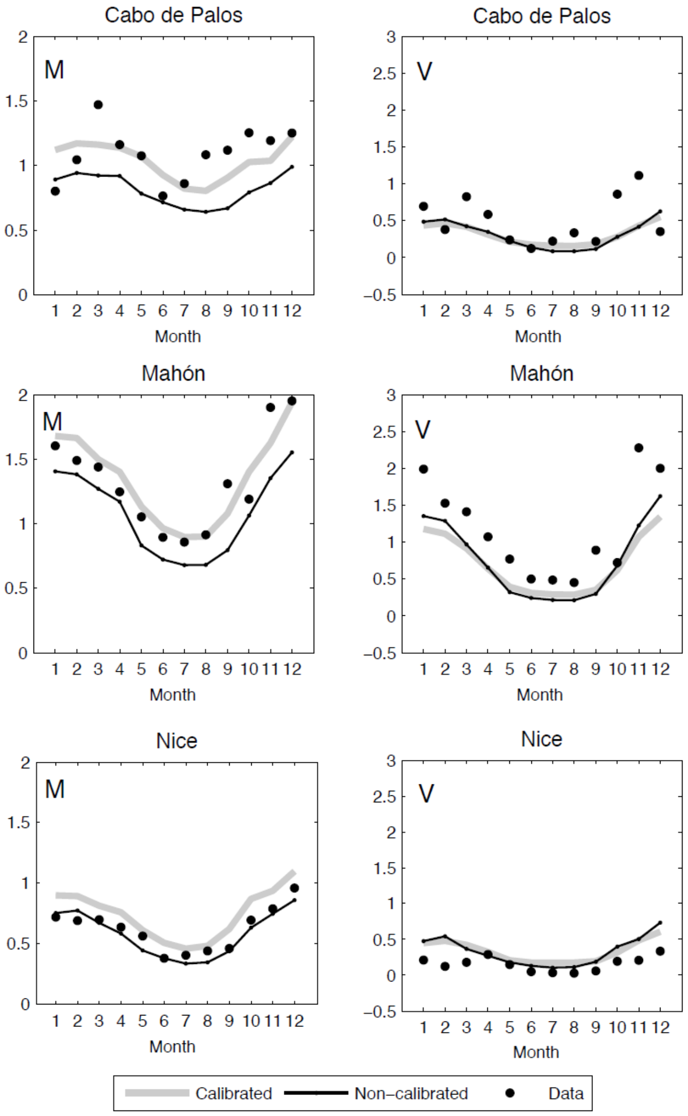

Figure 2.5. Annual cycle of the monthly mean (M) and variance (V) parameters of the log-normal distributions computed from the buoy records of Cabo de Palos, Mahón and Nice (dots) and from the non-calibrated (black lines) and calibrated (grey lines) model data at the closest grid point to each buoy.

The parameters A, B that define the relationship between hindcasted and calibrated SWH time series were calculated as expressed in equation (1.6). Two examples of the fit of the percentiles at two given locations (Mahón and Lion) are shown in Fig. 2.6. The plots illustrate the goodness of the fits; the highest percentiles shown in the Figure depart from the fit because they are actually not considered in the fitting process. Several tests (not shown) demonstrated that the inclusion of the highest order percentiles (99.5< **Pr**<99.999) in the fit resulted in a distortion of the calibration of the mean regime.

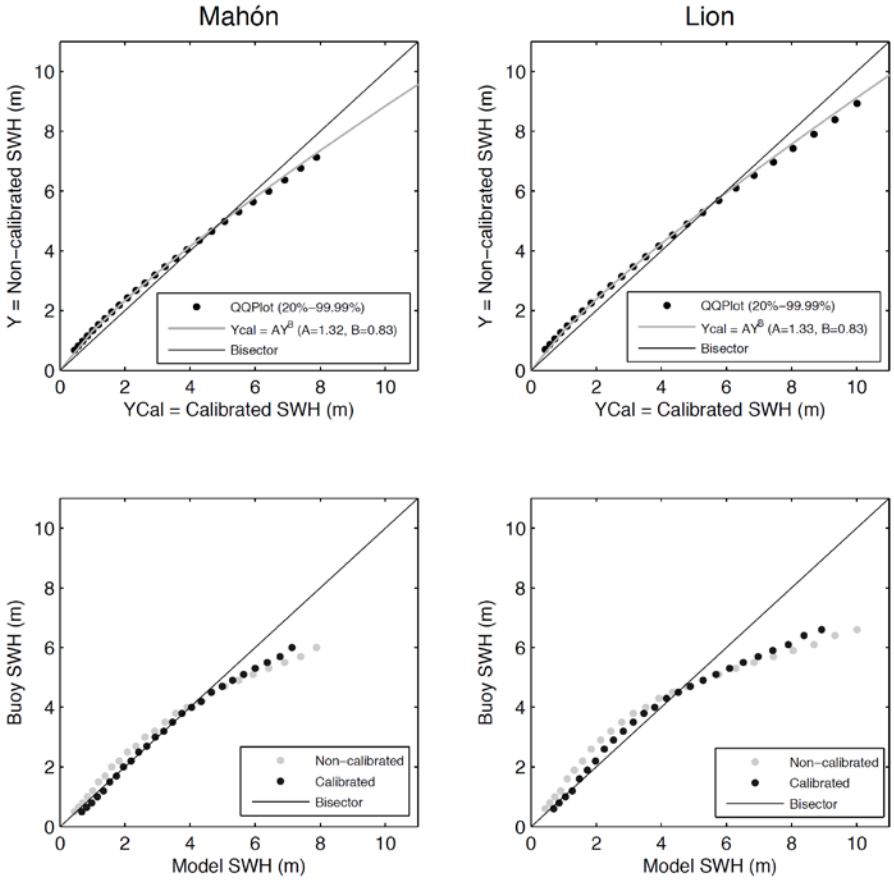

Figure 2.6. (Above) QQ plot of calibrated (Ycal) and non-calibrated (Y) averaged random time series for two stations, Mahón and Lion (dots). The fitting of equation (1.6) is also shown (gray line). Percentiles in the range 20 - 99.999 are plotted, although only those in the range 20 - 99.95 were used for the fit. (Below) Corresponding QQ plots of averaged random time series (non-calibrated (gray dots) and calibrated (black dots)) and observed time series at the two stations.

The spatial distributions of the parameters A and B are mapped in Fig. 2.7. The plots indicate that the calibration does not dramatically modify the hindcasted fields, since both parameters A and B are close to 1 everywhere in the domain. Parameter A is particularly close to 1 in areas where the mean and variance of SWH are low (e.g. near the coast) and higher than 1 where M and V are higher (in the middle of the basin). This parameter is responsible for the SWH increase that intends to overcome the underestimation of the hindcast. Parameter B shows a smoother behavior over the whole basin, ranging from 0.81 near the Iberian Peninsula to 0.83-0.84 over most of the domain. It departs significantly from 1 near the Iberian Peninsula, while it is closer to 1 in the rest of the domain.

The improvement of the calibrated hindcast with respect to the non-calibrated one was quantified in terms of the reduction of the bias and the RMS differences between the hindcasted SWH and the observed SWH at each buoy location for their overlapping periods. Results are listed in Table 2.2. Overall (considering all the buoys) the calibration resulted in a very significant reduction of the bias (by about 76%). At the very few buoys where the bias was initially smaller (in absolute value) than -0.10 m (e.g. Banyuls, Nice, Capo Gallo and Cabo de Gata) the calibration resulted in an overestimation of the SWH and an increase of the initial RMS. On average, the total RMS differences between observed and modelled SWH were reduced by 10%. The overall improvement resulting from the calibration process is illustrated in Fig. 2.8 for the buoy of Cabo de Palos.

2.4.2 Validation with altimetry

SWH from satellite altimetry averaged over the period 1992-2008 is mapped in Figure 2.9a. Values are higher (about 2m) in the middle of the basin and decrease towards the coasts. The SWH averaged over the domain was 1.26 m. Modelled gridded data were interpolated at the same times and locations of satellite track observations for comparison. Non-calibrated and calibrated SWH fields are mapped in Figures 2.9b and 9c respectively. Both show a pattern similar to the observations, but before the calibration SWH was significantly smaller than the observed value (mean value of 0.89 m). The underestimation of the hindcast is similar to that inferred from the comparison between hindcast and buoys. After the calibration, modelled SWH became closer to altimetry observations everywhere in the domain, with a mean value of 1.15 m and maximum values of 2 m in the centre of the basin.

The bias and RMS differences between altimetric observations and modelled data are mapped in Figure 2.10 for both non-calibrated and calibrated SWH. Before the calibration, the bias was negative over the entire domain, with an average value of -0.34 m but reaching -0.5 m in the middle of the basin. Bias was significantly reduced after calibration, resulting in an average value of -0.08 m. The improvement in the RMS differences was less dramatic, changing from 0.75 m to 0.68 m on average. Overall, the comparisons with altimetric observations indicated that both the bias and RMS differences between the hindcast and altimetry data were reduced by about 80% and 9%, respectively.

2.5 Discussion and conclusions

The calibration of SWH following the methodology proposed by Tomas et al (2008) has resulted in a significant improvement of the wind-wave hindcast over the entire domain. Major differences with respect to the results presented by

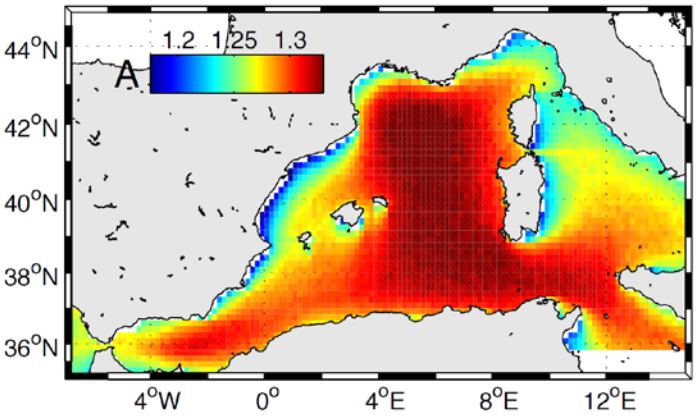

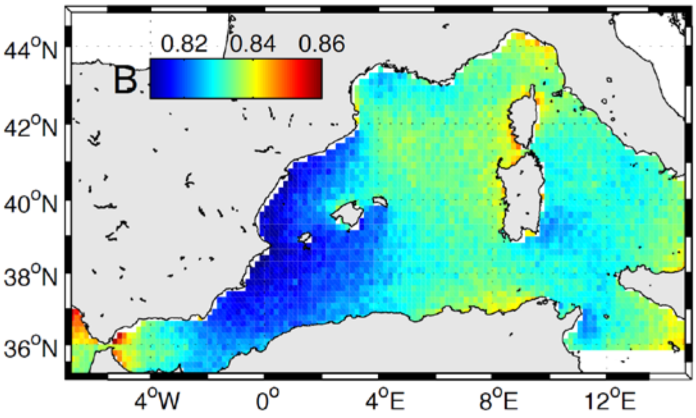

Figure 2.7. Spatial distribution of parameters A and B linking the SWH of the calibrated and non-calibrated wave fields (see Equation (1.7)).

Tomas et al (2008) are the larger domain (the whole Western Mediterranean basin) and the extended temporal coverage (1958-2008). Both conditions allowed increasing the number of buoys used in the calibration (up to 22), which is expected to improve the results. Nevertheless the impact of the number of buoys used in the calibration process was checked by using different subsets of buoys containing from 2 to 22 buoys. All possible combinations were considered, implying a different number of subsets depending on the number of buoys (e.g. 231 combinations of 2 buoys, 1540 combinations of 3 buoys, ... , 22 combinations of 21 buoys and 1 single combination of 22 buoys). For each combination, the RMS differences between the calibrated parameters (Mc and Vc) and those calculated from buoy data were computed. Then, for each group of n buoys (with n ranging from 2 to 22) the averaged RMS difference was obtained for all buoys

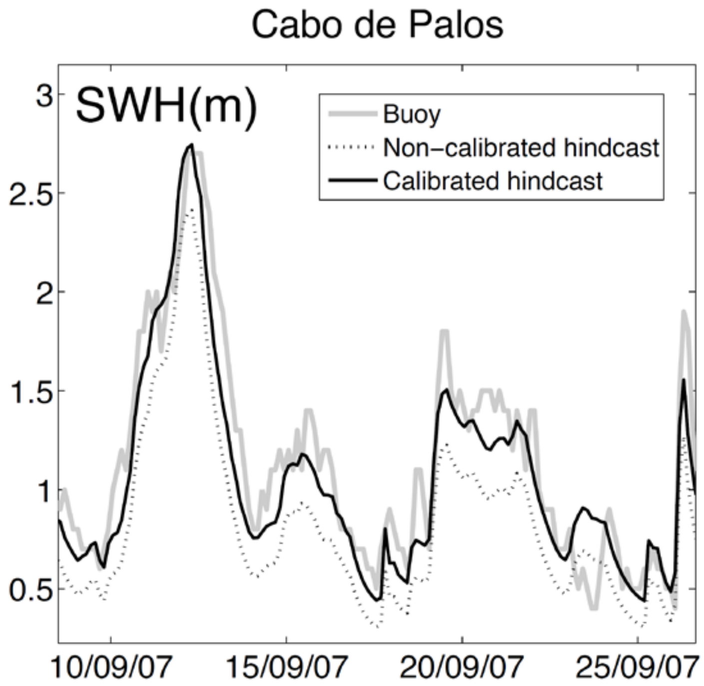

Figure 2.8. Comparison between SWH observed by the buoy of Cabo de Palos (grey line) and SWH at the closest grid point as given by the non-calibrated (black dashed line) and calibrated (black line) hindcasts during September 2007. Units are meters.

and also separately for those buoys used in the calibration and for those not used in the calibration (independent buoys). These averages together with the standard deviations of the RMS differences of each group of n buoys are plotted in Figure 2.11 for the parameter M. The parameter V is not shown, since results were very similar and led to the same conclusions. Results show that the overall RMS difference decreases on average with increasing number of buoys used for calibration (blue dots), as expected intuitively. It is noteworthy that the standard deviation of RMS differences for the independent buoys (green dots) is larger when either very few buoys are used for calibration, due to the poor fit in the rest of locations, or when a large number of buoys are used for the calibration, due to the spatial variability of observations of the remaining independent buoys that leads to a smaller sample size and thus to greater uncertainty.

For each group of n buoys, the optimum subset (defined as the one resulting in the highest reduction of the RMS difference in M, although not necessarily in the highest reduction of the bias) was determined. These optima combinations were then used to generate calibrated SWH time series that were finally compared with altimetric observations. Mean bias and RMS differences for selected groups are listed in Table 2.3. Despite the highest RMS reduction was found for the largest

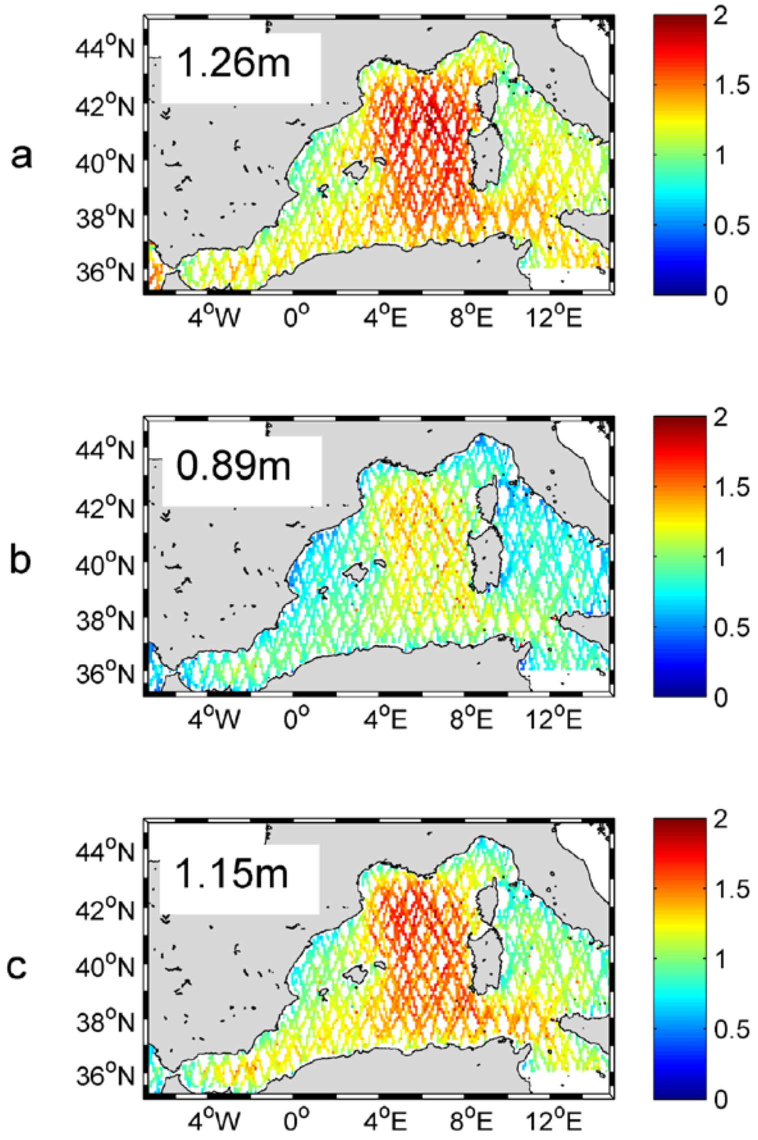

Figure 2.9. (a) SWH observed by satellite altimetry averaged over the period 1992-2008. (b) Hindcasted SWH at the same locations of satellite observations and averaged over the same period. (c) As in (b), but for calibrated SWH. The mean values for each field are also quoted.

number of buoys (22), comparable solutions were obtained with a smaller number of buoys. This result suggest that, in order to apply a spatial calibration of a wind-wave hindcast, a small number of single-point records would suffice, provided that the buoys have an optimum spatial coverage. Conversely, when the worst subset of buoys (in terms of RMS reduction) is chosen, the result of the calibration can even worsen the non-calibrated SWH. This is illustrated with the results using the worst combination with 10 buoys included in Table 2.4. These tests help to detect those buoys that have a negative impact in the calibration

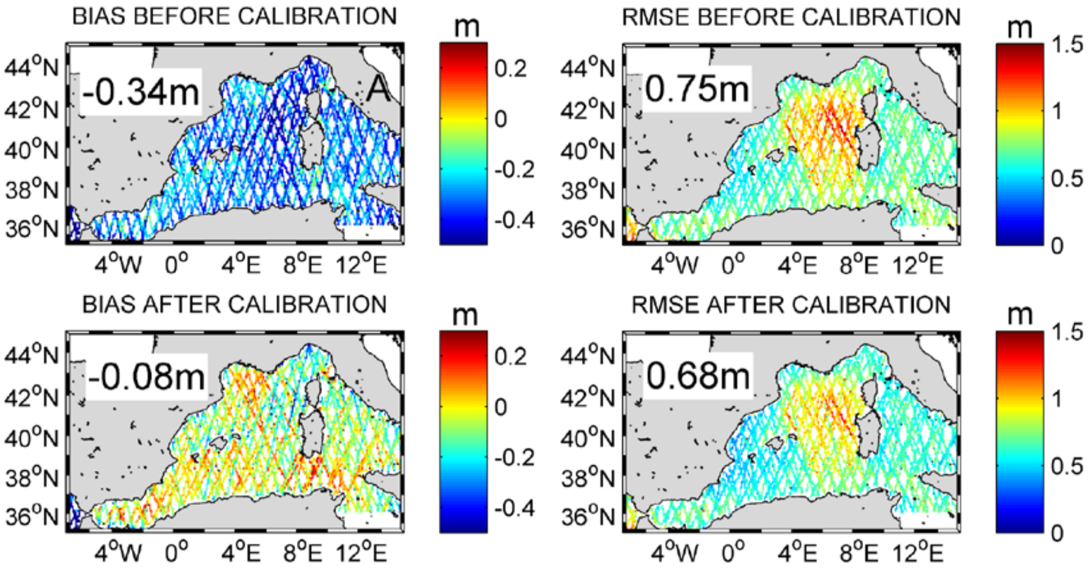

Figure 2.10. Bias and RMS differences between altimetry observations and modelled data before (upper panels) and after (lower panels) the calibration process. The mean values of the fields are given inside the maps.

process. Figure 2.12 represents the location of corresponding buoys to the best (above) and worst (below) combination of 10 buoys, showing a significant difference between them. The buoys corresponding to the best combination are spatially distributed over the basin, while the worst combination presents the buoys grouped at northwest of the basin.

As a general rule and on the basis of these results, therefore, the use of the maximum number of records is advised.

In addition to the subset of buoys used for the calibration, the eventual impact of the number of EOFs considered in the decomposition of the M and V fields was also tested. Thus, by considering an additional mode the reduction of the RMS barely increased in 0.11%. This supports the robustness of the results.

Perhaps the most important limitation of the method is the assumption of a log-normal distribution. It has been shown that the mean wave regime obeys such a distribution, but also that extreme events depart from it. This made that when inferring the calibration parameters $A(x)$, $B(x)$, the highest percentiles were eliminated in order to avoid a distortion of the fit. An obvious, related consequence is that the calibration is only valid for the mean regime, not for extreme events. The exploration of other statistical distribution models is left for further applications. A further eventual improvement could come from allowing the parameters of the distribution to depend not only on the location and time, but also on the mean wave direction.

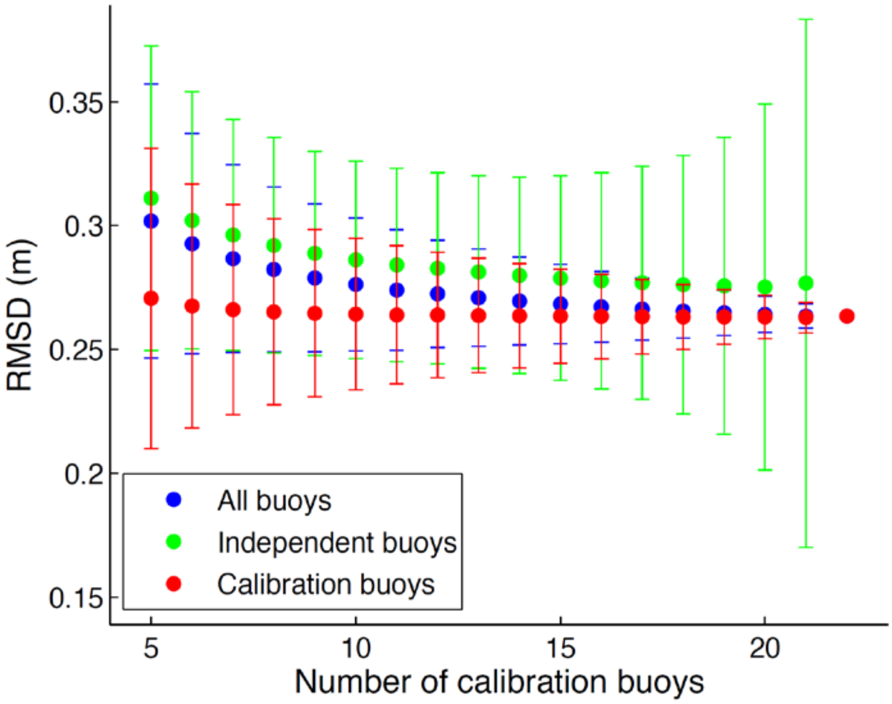

Figure 2.11. Averaged values (dots) and standard deviations (bars) of RMS differences between the calibrated parameter Mc and the parameter inferred from buoy data for different subsets of n buoys (with n ranging from 2 to 22). Values are computed for all buoys (blue), for buoys used in the calibration process (red) and for independent buoys (green).

Table 4. Mean value of the calibrated hindcast and bias and RMS differences with respect to altimetric observations when the calibration is performed with different subsets of n buoys. The average values obtained from the optima combinations on N buoys are quoted. For the subset of 10 buoys, results for the worst (in terms of RMS reduction) combination are also quoted.

N	*Mean value of the calibrated SWH (m) (Observed mean = 1.26m)*	*RMS (m)*	*BIAS (m)*
Before calibration	*0.89*	*0.75*	*-0.34*
5	*1.04*	*0.69*	*-0.2*
10	*1.05*	*0.7*	*-0.18*
15	*1.11*	*0.69*	*-0.12*
20	*1.13*	*0.69*	*-0.1*
22 (all buoys)	*1.15*	*0.68*	*-0.08*
10 (worst)	*1.35*	*0.77*	*0.13*

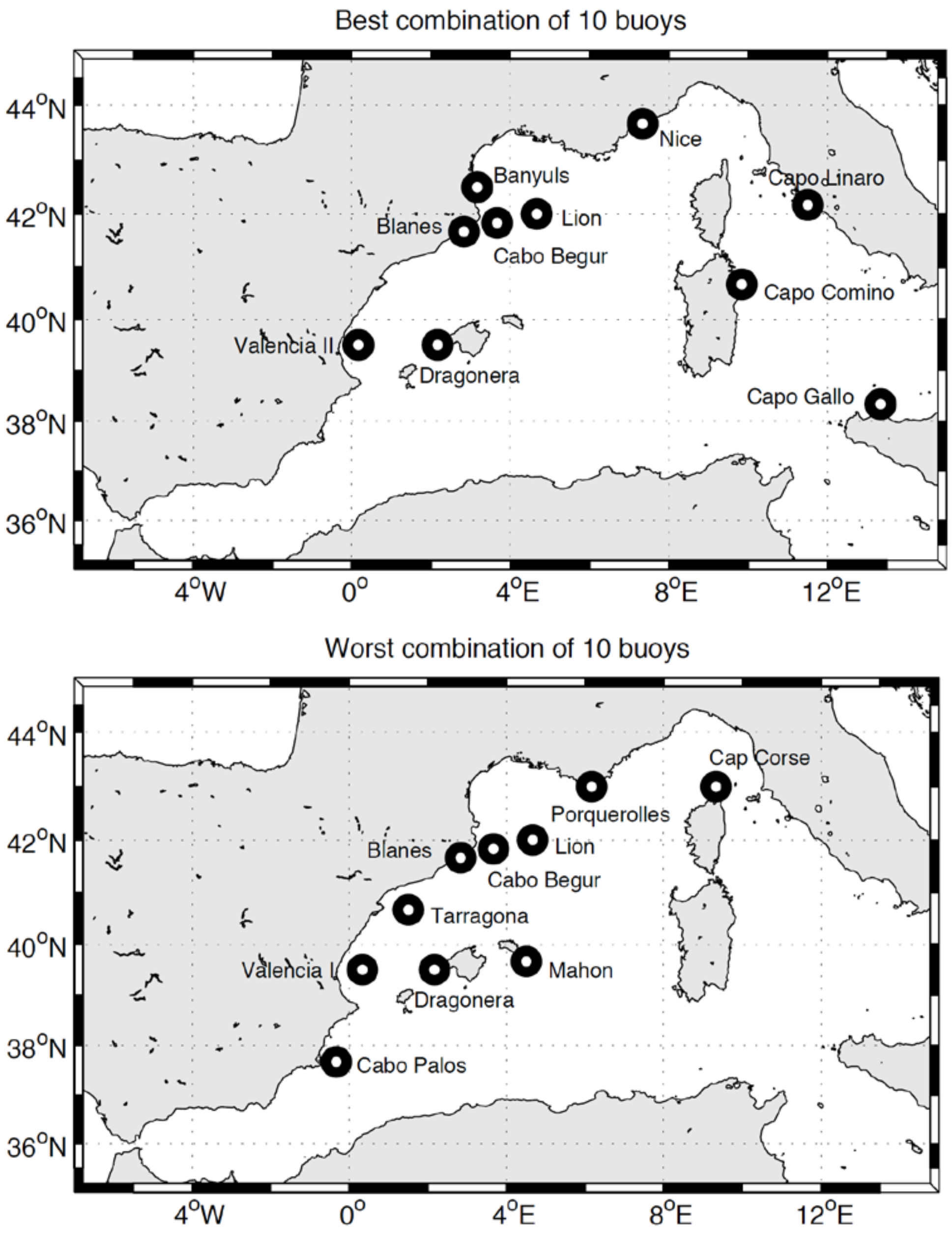

Figure 2.12. Maps of boys corresponding to the best (above) and worst (below) combination of 10 buoys, in terms of RMS reduction.

The overall improvement brought in by the calibration can be summarized in terms of the reduction of the bias and of the total RMS differences between the hindcasted SWH and the observations averaged over the overlapping periods. Since the original hindcasted SWH underestimated observations, the effect of the calibration has been in the sense of increasing SWH values. When compared with independent altimetric observations the reduction of the negative bias was of 76%, whereas the reduction in the RMS differences was 10%. When compared with buoys, the bias was also significantly reduced in the vicinity of most of them (78% on average), the exception being those with a very small bias in the original hindcast. For these ones, the RMS differences between model and observations either slightly increased or remained unchanged after calibration (see Table 2.2). Likewise, for about 4% of satellite locations, corresponding to those areas with initial small biases, the calibration process had a slightly negative impact in terms of bias and RMS differences. The smooth variation in space of the calibration parameters does not enable to obtain a similar improvement in those buoys that show significant differences in terms of bias and are close to each other. This is for example the case of Valencia I and II stations.

Errors in the estimation of SWH from buoy observations have been quantified in about 5 cm including both the instrumental and statistical uncertainties (Puertos del Estado, 1996). Hindcasted SWH time series underestimate buoy observations in the Western Mediterranean by an average value of 18 cm, reaching around 30 cm at several sites. After calibration, the bias between model and observations becomes closer to the error bars, being in general smaller than 10 cm (except for those locations where the calibrated SWH overestimates the observations).

The ultimate result of this work is a more realistic characterization of the wave climate of the Western Mediterranean during the last five decades, which is intended to be distributed to the community of scientists and coastal managers.

Acknowledgments

This work has been carried out in the framework of the projects VANIMEDAT-2 (CTM2009-10163-C02-01, funded by the Spanish Marine Science and Technology Program and the E-Plan of the Spanish Government) and ESCENARIOS (funded by the Spanish *Agencia Estatal de METeorología*). Adrián Martínez acknowledges an FPI grant funded by the Spanish Ministry of Science and Innovation; Marta Marcos acknowledges a “Ramon y Cajal” contract funded by the Spanish Ministry of Science; and Gabriel Jordà acknowledges a “JAE-Doc” contract funded by the Spanish Research Council (CSIC). We want to thank Puertos del Estado, the XIOM of the Catalan Government, CANDHIS, METEO-FRANCE and ISPRA for kindly providing the buoy data. The altimeter products were produced by CLS Space Oceanography Division and distributed by AVISO, with support from CNES. We are grateful to M. Gómez and M. Alfonso for discussion of parts of this work.

Bibliography

Aviso (Archiving, Validation and Interpretation of Satellite Oceanographic data). 2012. DT CorSSH and DT SLA Product Handbook. CLS-DOS-NT-08.341, Ed. 1.9. Available online at: http://www.aviso.oceanobs.com/fileadmin/documents/data/tools/hdbk_dt_corssh_dt_sla.pdf (accessed February 28, 2012).

Caires, S., A. Sterl, 2005. A New Nonparametric Method to Correct Model Data: Application to Significant Wave Height from the ERA-40 Re-Analysis. J. Atm. Oc. Tech., 22, 443-459.

Cavaleri, L., Bertotti, L., 2004. Accuracy of the modelled wind and wave fields in enclosed seas. Tellus 56A, 167–175.

Cavaleri, L, M. Sclavo, 2006. The calibration of wind and wave model data in the Mediterranean Sea. Coast. Eng., 53, 613-627.

Challenor, P.G. and Cotton, P.D., 2002. The joint calibration of altimeter and in-situ wave heights, in Advances in the Applications of Marine Climatology – The dynamic part of the WMO guide to the applications of marine climatology, WMO/TD-No. 1081 JCOMM Tech. Rep. No. 13, World Meteorol. Organ., Geneva.

Cotton, P.D. and Carter, D.J.T., 1994. Cross-calibration of TOPEX, ERS-1, and Geosat wave heights. J. Geophys. Res., 99, 25025-25033. Correction, 1995. J. Geophys. Res., 100, 7095.

Feng, H., D. Vandermark, Y. Quilfen, B. Chapron, B. Beckley, 2006. Assessment of wind forcing impact on a global wind-wave model using TOPEX altimeter. Ocean Eng., 33 (11–12), 1431– 1461.

Günther, H., S. Hasselman, P. A. E. Jansen, 1992. The WAM model cycle, 4. Technical Report 4. DKRZ.

Hernández-Molina, F. J., Fernández-Salas, L. M., Lobo, F. Somoza, L. Somoza, L. Díaz-del-Río, V. Alveirinho Dias, J. M., 2000. The infralittoral prograding wedge: a new large-scale progradational sedimentary body in shallow marine environments. Geo-Marine Letters, 20(2), 109-117.

Herrmann, M., S. Somot, 2008. Relevance of ERA40 dynamical downscaling for modeling deep convection in the Mediterranean Sea. Geophys. Res. Let., 35 (L04607), 1–5.

Holthuijsen, L.H., 2007. Waves in oceanic and coastal waters. Cambridge Univ. Press.

Janssen, P. A. E., S. Abdalla, H. Hersbach, J. R. Bidlot, 2007. Error Estimation of Buoy, Satellite, and Model Wave Height Data. J. Atmos. Ocean. Tech., 24, 1665-1677.

Jordà, G., D. Gomis, S. Somot, E. Álvarez-Fanjul, 2012. Atmospheric contribution to Mediterranean and nearby Atlantic sea level variability under different climate change scenarios. Global Planet. Change, 80-81, 198–214.

Mínguez, R., A. Espejo, A. Tomás, F. J. Méndez, I. J. Losada, 2011. Directional Calibration of Wave Reanalysis Databases Using Instrumental Data. J. Atmos. Ocean. Tech., 28, 1466–1485.

North, G. R., T. L. Bell, R. F. Cahalan, F. J. Moeng, 1982. Sampling errors in the estimation of empirical orthogonal functions. Mon. Wea. Rev., 110, 699–706.

Overland, J. E., R. W. Preisendorfer, 1982. A significance test for principal components applied to a cyclone climatology. Mon. Wea. Rev., 110, 1–4.

Puertos del Estado, 1996. Verificación estadística de la predicción de oleaje. Informe técnico CEDEX 20-496-2-001

Queffeulou, P. 2004. Long-term validation of wave height measurements from altimeters. Mar. Geodes., 27, 495–510.

Queffeulou, P., A. Bentamy, 2007. Analysis of Wave Height Variability Using Altimeter Measurements: Application to the Mediterranean Sea. J. Atm. Oc. Tech., 24, 2078-2092

Queffeulou, P., Croizé-Fillon, D. 2011. Global altimeter SWH data set, version 11, December,
ftp://ftp.ifremer.fr/ifremer/cersat/products/swath/altimeters/waves/

Ratsimandresy, A. W., M. G. Sotillo, J. C. Carretero-Albiach, E. Álvarez-Fanjul, H. Hajji, 2008. A 44-year high-resolution ocean and atmospheric hindcast for the Mediterranean Basin developed within the HIPOCAS Project. Coast. Eng., 55, 827–842.

Tomas, A., F. Méndez, I. Losada, 2008. A method for spatial calibration of wave hindcast data bases. Cont. Shelf Res., 28, 391–398.

WAMDI Group, 1988. The WAM model—a third generation ocean wave prediction model. J. Phys. Oceanogr., 18, 1775–1810.

Chapter 3

Impact of the atmospheric climate modes on Mediterranean sea level variability

> *Momo sabía escuchar de tal manera que a la gente tonta*
> *se le ocurrían, de repente, ideas muy inteligentes.*
>
> *Momo listened in a way that made slow-witted people*
> *have flashes of inspiration.*
>
> Michael Ende, Momo (1973)

This chapter has been published in:

- Martínez-Asensio, A., Marcos, M., Tsimplis, M. N., Gomis, D., Josey, S., Jorda, G., 2014. Impact of the atmospheric climate modes on Mediterranean sea level variability. Global and Planetary Change, 118, 1-15.

Abstract

The relationships of Mediterranean sea level, its atmospherically driven and thermosteric components with the large scale atmospheric modes over the North Atlantic and Europe are explored and quantified. The modes considered are the North Atlantic Oscillation (NAO), the East Atlantic pattern (EA), the Scandinavian pattern (SCAN) and the East Atlantic/Western Russian (EA/WR). The influence of each mode changes between winter and summer. During winter the NAO is the major mode impacting winter Mediterranean sea level (accounting for 83% of the variance) with SCAN being the second (56%) mode in importance.

Both NAO and SCAN effects are partly due to direct atmospheric forcing of sea level through wind and pressure changes. However NAO and SCAN are correlated with each other during winter and they explain the same part of variability. The EA/WR also affects the atmospheric sea level component in winter (13%), acting through atmospheric pressure patterns. In winter, the thermosteric contribution is correlated with the SCAN in parts of the Eastern Mediterranean (9%). The rate of change of the thermosteric component in winter is correlated with the EA (24%). During the summer season, the sea level variance is much reduced and the impact of the large scale modes is in most parts of the Mediterranean Sea non significant.

3.1 Introduction

Sea level integrates changes in the thermohaline characteristics of the ocean waters due to heat fluxes and water advection, changes in the ocean mass either due to redistribution of water in response to the atmospheric mechanical forcing or due to the addition or removal of water from the land and the criosphere, and, depending on the reference system, may also include land movements and changes in the oceanic configuration. With the exception of land movements and changes in the shape of the oceanic basin the other two sea level components (thermohaline and mass) are influenced by the large scale atmospheric climate modes through their effect on atmospheric pressure gradients, wind, heat and freshwater fluxes and changes in the oceanic circulation.

Mediterranean sea level rise observed in the longest tide gauges during the last century (1.1-1.3 mm/year) was significantly lower than the global rate (1.5-1.9mm/year) (Tsimplis & Baker 2000; Church and White, 2011). An increase of the averaged atmospheric pressure over the basin during the period 1960-1990 resulted in negative trends of Mediterranean sea level, while in the Atlantic stations the positive trends were lower for this period (Tsimplis & Baker 2000; Tsimplis & Josey 2001). Global and Mediterranean rates significantly increased during the period 1993-2010 (Church and White, 2011; Cazenave et al.2001; Fenoglio-Marc 2001).

For the Mediterranean Sea, the North Atlantic Oscillation (NAO) is known to affect, primarily, winter sea level variability (Tsimplis and Josey, 2001; Gomis et al 2008; Tsimplis and Shaw, 2008; Criado-Aldeanueva et al., 2008; Tsimplis et al, 2013). In addition to dominating the atmospheric component of sea level, a smaller influence of the NAO has also been suggested on the thermosteric component (Tsimplis and Rixen, 2002; Tsimplis et al., 2006; Tsimplis et al., 2013), and on the net evaporation (Tsimplis and Josey, 2001; Mariotti et al., 2002;

Fenoglio-Marc et al., 2013) of the Mediterranean Sea. The Mediterranean Oscillation Index (MOI) has been successfully correlated with mean sea level changes, especially during the winter season (Gomis et al 2006; Tsimplis and Shaw, 2008); namely it has been shown to explain 46% of the winter sea level variance for the period 1993-2001 (Suselj et al, 2008). It is worth noting, however, that the NAO index and the MOI are not independent and are significantly correlated in winter.

Raicich et al (2003) found that summer sea level atmospheric pressure in the Mediterranean region is correlated with the Indian monsoon and the Sahel rainfall indices, attributed to particular wind regimes over the area which in turn influenced coastal sea level. Tsimplis and Shaw (2008) identified the East Atlantic pattern (EA) as an additional atmospheric mode impacting sea level, but they only found significant correlations in the Adriatic and once the atmospheric pressure effect was removed. Josey et al (2011) suggested that at least in some parts of the Mediterranean Sea there is a distinct contribution to heat fluxes linked with climatic indices different from NAO, such as the East Atlantic (EA) and the East Atlantic/Western Russian (EA/WR) patterns. In particular they identified correlations between the winter basin averaged heat fluxes and EA, especially at Northwestern Mediterranean and Southern Adriatic, while the correlations between each winter subbasin averaged and EA/WR were in opposite sense in each region, with major values at Aegean Sea. The influence of these modes on heat fluxes necessarily poses the question whether such modes affect at least the steric component of sea level.

The present paper assesses and clarifies the influence of the four major atmospheric modes over the North Atlantic, namely the NAO, the EA the EA/WR and SCAN, on Mediterranean sea level as well as its component driven by wind and atmospheric pressure changes and on the thermosteric component. The analysis is performed for different periods dictated by the availability of tide gauge data and altimetry data. The paper is organized as follows: Section 2 introduces the data sets to represent sea level and its components and the climate indices. In Section 3 we present the methodology of the analysis and in Section 4 we show the main results. Finally, a discussion and some concluding remarks are presented in Sections 5 and 6.

3.2 Data sets

Sea level observations and estimates of the various contributions to sea level variability have been obtained from the following data sources.

3.2.1 Tide gauge data

Monthly mean sea level values with benchmark history (Revised Local Reference, RLR) were retrieved from tide gauge records archived at the Permanent Service for Mean Sea Level (PSMSL; Woodworth and Player, 2003). We selected 12 tide gauges distributed along the Mediterranean coasts, each of them spanning more than 35 years of the last decades of the 20th century. The tide gauge stations and their periods of operation are listed in Table 3.1. Finally, a set of atmospherically-corrected tide gauge records was obtained through removing the atmospheric contribution as given by a sea level hindcast, at the closest grid point to each tide gauge. The VANI2-ERA hindcast used is described later.

3.2.2 Altimetry data

Gridded Sea Level Anomaly (SLA) fields were obtained from the merged AVISO products available at http://www.aviso.oceanobs.com. The data consist of monthly multimission (up to four satellites at a given time) gridded global sea surface heights spanning the period 1993-2010, with a spatial resolution of 1/4°×1/4°. This version comes with all the standard geophysical corrections applied including the so called Dynamic Atmospheric Correction (DAC; Volkov et al 2007) that accounts for the effect of atmospheric pressure and wind on sea level. This dataset will be referred to as DAC-altimetry. The DAC correction, as supplied by AVISO, was added back to altimetry in order to create a second data set accounting for the atmospheric pressure and wind effects on sea level. This will be called altimetry. Note that because the dataset is a combination of observations from different platforms there is significant uncertainty for the trends derived especially for the last mission. In addition, the applied GIA corrections also introduce significant errors in trends (Ablain et al., 2012). However we do not consider these uncertainties as capable of affecting the correlation with the various atmospheric modes because the variance linked to long term trends is much smaller than the interannual variability analized here.

3.2.3 Atmospherically-induced sea level

The meteorological contribution to sea level caused by the combined action of atmospheric pressure and wind was quantified from the VANI2-ERA data set (Jordà et al., 2012). VANI2-ERA data are 6-hourly sea surface heights obtained with a barotropic version of the HAMSOM model forced with atmospheric pressure and winds from a dynamical downscaling of the ERA40 reanalysis. The data span the period 1958-2008 and cover the Mediterranean Sea and a sector of the NE Atlantic Ocean with a spatial resolution of 1/6°×1/4°. Two additional

Table 3.1. List of tide gauges, location, periods of operation and percentage of gaps

Station Name	Area	Latitude (º, Min)	Longitude (º, Min)	Period	Gaps (%)
Malaga	W. Med.	36 43 N	04 25 W	1950-2010	15.00
Alicante	W. Med.	38 20 N	00 29 W	1960-1997	2.70
Marseille	W. Med.	43 18 N	05 21 E	1950-2011	0.00
Genova	W. Med.	44 24 N	08 54 E	1950-1997	6.38
Venice	Adriatic	45 26 N	12 20 E	1950-2000	2.00
Trieste	Adriatic	45 39 N	13 45 E	1950-2011	1.64
Rovinj	Adriatic	45 05 N	13 38 E	1955-2008	1.89
Bakar	Adriatic	45 18 N	14 32 E	1950-2008	1.72
Split I	Adriatic	43 30 N	16 23 E	1952-2008	1.79
Split II	Adriatic	43 30 N	16 26 E	1954-2008	1.85
Dubrovnik	Adriatic	42 40 N	18 04 E	1956-2008	1.92
Alexandria	E. Med.	31 13 N	29 55 E	1950-1989	2.56

runs were also performed: one forced only by wind and the other forced only by atmospheric pressure variations. Model hourly outputs were converted into monthly fields at each grid point.

3.2.4 Hydrographic data and thermosteric sea level

Ocean temperature (T) fields from Ishii and Kimoto (2009; version 6.12) were used to compute thermosteric sea level in the Mediterranean Sea (download website: http://rda.ucar.edu/datasets/ds285.3/). The data set consists of monthly T fields over a 1ºx1º global grid down to 1500m and spanning the period 1950-2011. Thermosteric sea level was computed at each grid point over the Mediterranean Sea by vertically integrating the specific volume anomaly at each grid cell down to 300 m. The reference level at 700 m was also sued for comparison, but the results did not differ. Therefore the 300 m reference level was preferred because there are a higher number of observations at upper levels. Depths deeper than 700 m were not considered due to the scarcity of observations. Salinity (S) values are also available in the same dataset. However, because S measurements are highly sparse and uncertain over the entire basin (Jordà and Gomis, 2013), thermosteric sea level was preferred instead of steric sea level. For the calculation of the thermosteric height changes S was considered constant to the 1950 value at each depth.

3.2.5 Atmospheric variables

Mean sea level atmospheric pressure, 2m air temperature, net heat fluxes and

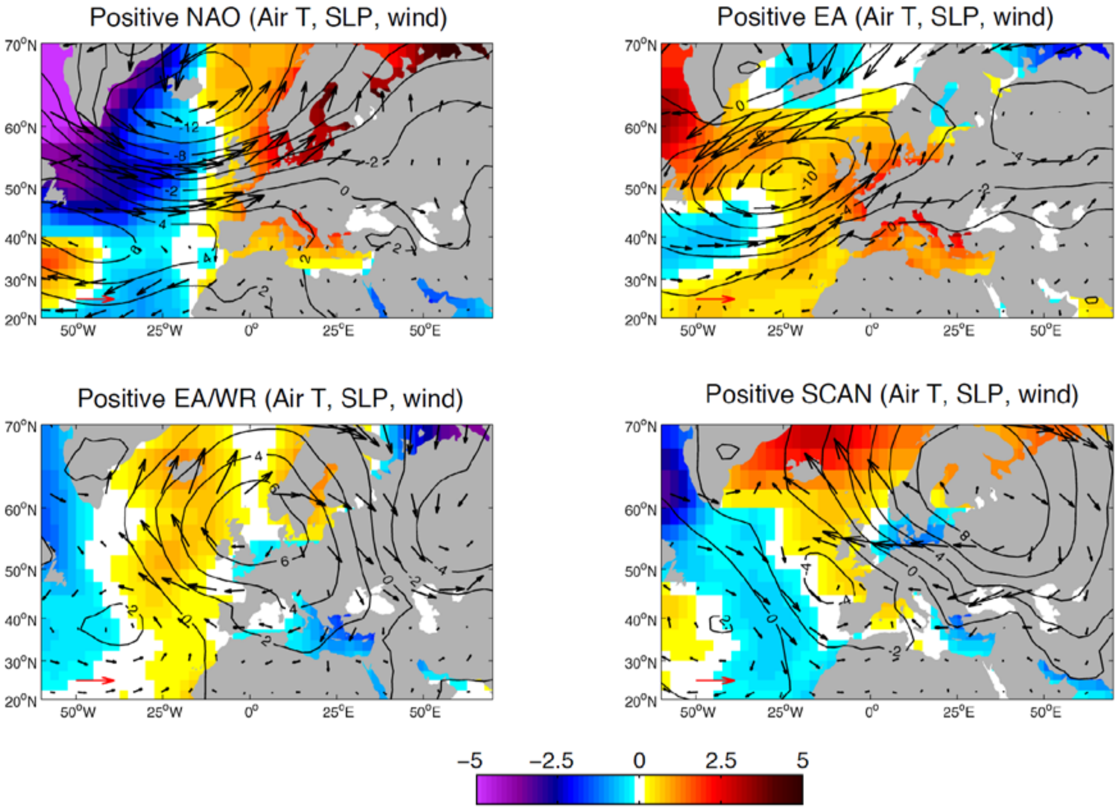

Figure 3.1. Winter (Dec-Mar) NCEP 2m air temperature anomalies (coloured field, ºC), 10m wind speed anomalies (vectors) and sea level pressure anomalies (contours) for a unit value of the positive index of: (a) NAO, (b) EA, (c) EA/WR and (d) SCAN. Note that the horizontal vector (red arrow) is for scale and indicates a wind speed of 5m/s.

10m wind velocity, were obtained from NCEP/NCAR atmospheric reanalysis (Kistler et al., 2001). We used monthly mean values obtained from the 6h output fields with a spatial resolution of 2.5ºx2.5º over the period 1950-2011.

3.2.6 Climate indices

The leading atmospheric climate modes used, namely NAO, EA, EA/WR and SCAN, as computed for the period 1950-2011 were downloaded from the NOAA Climate Prediction Centre (http://www.cpc.ncep.noaa.gov/data/teledoc/telecontents.shtml). These modes were obtained through a rotated principal component analysis (Barnston and Livezey, 1987) of the monthly mean standardized 500-mb height anomalies in the Northern Hemisphere. This ensured that they are orthogonal (independent) to each other at a monthly scale. The source of the data is the same as that used by Josey et al (2011) although the period covered in this study is longer. Our

Table 3.2. Correlation coefficients between winter (upper right triangle of the matrix) and summer (lower left triangle of the matrix, in italic) climate indices for the period 1950-2012. Boldface values denote statistical significance at 95% level.

	NAO	EA	EA/WR	SCAN
NAO	1	0.11	0.05	**-0.42**
EA	*-0.2*	1	0.02	0
EA/WR	*0.2*	***-0.37***	1	-0.16
SCAN	*0.17*	***-0.27***	***0.25***	1

approach has considered the sea level impacts of the four leading modes of atmospheric variability that have an influence in the Mediterranean Sea region as identified by the NOAA Climate Prediction Centre analysis. Other patterns can be defined but they are likely to reflect a combination of the modes that we have already employed. Hence, our focus has been on these four modes. Future research that considers Mediterranean sea level impacts of other patterns of variability should be careful to identify the extent to which the other patterns are dependent on those already considered here.

3.3 Methodology

Winter and summer averages, defined as the mean values over the period December to March and June to August, respectively, were computed for each climate index. The correlations among the seasonal averages of the climate indices used are listed in Table 3.2. The NAO and SCAN are anticorrelated in winter. In the summer the EA, EA/WR and SCAN are all correlated with each other.

Composite fields of 2m air temperature, sea level pressure and wind anomalies were used to develop spatial patterns of the relevant atmospheric field corresponding to the high and low values of each index. The composite fields were built as follows: first, monthly fields of the atmospheric variables coinciding with a climate index larger than 1.5 (or lower than -1.5) were selected. Each monthly field was then multiplied by the corresponding index value and the resulting time series was weighted averaged. The pattern obtained in this way can be considered associated with a unit positive value of the climate index. Using different thresholds for the climate indices did not alter significantly the results. The resulting patterns for the positive phase of each index are shown in Figure 3.1.

Table 3.3. Mean and standard deviation of winter and summer variance of each data set. For tide gauges and atmospherically-corrected tide gauges the variance of each tide gauge was calculated and then the average value and the STD are shown. For sea level altimetry, DAC-Altimetry, atmospheric component, pressure-only and wind-only components and thermosteric sea level the variance at each grid point has been calculated and then the average and STD are shown. The lowest and highest variances of each data set are also shown (in brackets). (*) The units for the thermosteric rate of change are cm/month.

	Winter Variance (cm2)	Summer Variance (cm2)
Tide gauges	32±10 (17-44)	7±2 (2-10)
Atm-Corr. Tide gauges	11±2 (5-15)	5±2 (1-10)
Altimetry	19±7 (6-73)	6±6 (1-64)
DAC-Altimetry	11±7 (3-81)	6±6 (1-63)
Atmospheric component	6.1±2.1 (2.2-13.7)	0.6±0.1 (0.2-1.2)
Pressure-only component	3.3±1.5 (0.5-6.3)	0.4±0.1 (0.1-0.6)
Wind-only component	0.7±0.2 (0.4-2.8)	0.1±0.0 (0.1-0.4)
Thermosteric component	0.9±0.5 (0.0-2.5)	1.5±0.8 (0.0-4.6)
Thermost. rate of change*	0.2±0.1 (0.0-0.5)	0.4±0.1 (0.0-0.5)

Seasonal averages were calculated for the tide gauge records for the period December to March (winter) and for the period June to August (summer). For the gridded data, seasonally basin averaged time series, for the same periods, were obtained by calculating averages over the whole Mediterranean basin as well as over the eastern and western sub-basins (the Sicily Strait has been used as the separation line between the eastern and western basins). Seasonal variances of the different data sets are listed in Table 3.3. The values correspond to the basin averaged variance and its standard deviation. The lowest and highest value for each data set is also shown for comparison.

All time series were detrended and the seasonal cycle was removed before the regression analysis. The relationship between the various climate indices and sea level was explored on the basis of the correlation and linear regression values between the seasonal (winter and summer) anomalies of each variable and the corresponding seasonal time series of each index. The trend removed corresponded to the common period of the time series and the corresponding index. Significance was set at the 95% level.

Multiple linear regression analysis was, in addition, performed with sea level or one of its components as the dependent parameter and all four indices as independent parameters. Note that the correlation between the seasonal values of the indices (Table 3.2) indicates that there is the possibility that the same variance in sea level can be accounted for by more than one index. Forward stepwise multiple linear regression analysis (Draper and Smith, 1998) was used to select the statistically significant contributors. This procedure selects the most correlated dependent variable and removes its influence through a regression analysis. Then it checks for correlation between the rest of the dependent parameters and the residual signal, until the correlation becomes non-significant. Where more than one index can account for the same part of variability the regression model favours the index that accounts for the highest percentage of total variability.

3.4 Results

3.4.1 Observed sea level from tide-gauges

Correlations between seasonal climate indices and tide gauge records and atmospherically corrected tide gauge records are shown in Figure 3.2. For some of the indices significant differences can be found between eastern and western basins. The winter NAO is found to be correlated with observed winter sea level at all sites. In the Adriatic it was also correlated during summer at most stations. SCAN was positively correlated during winter in the Adriatic stations as well as in Marseille and Genova. These similarities are in agreement with the negative correlation of -0.47 found between winter NAO and SCAN (Table 3.2). EA/WR was correlated with sea level during winter, in the Adriatic Sea and Alexandria at the Eastern Mediterranean. The removal of the atmospheric forcing component using VANI2-ERA hindcast reduced the correlation coefficients but did not make the correlations statistically insignificant.

During the summer season the NAO is correlated with sea level in some Adriatic stations. The EA is correlated in the Adriatic stations and Genova. The removal of the atmospheric forcing component increased the correlation with the EA in the Adriatic.

The variance accounted for by the indices at each tide gauge record and the corresponding atmospherically corrected tide gauge record are listed in Table 3.4.

The results of the regression analysis against the four modes are shown at Table 3.4. The results for the multiple regression are shown in parenthesis. Note that although SCAN accounts for a significant amount of the variance for the Adriatic stations and Genoa and Marseille in the multiple regression model it is

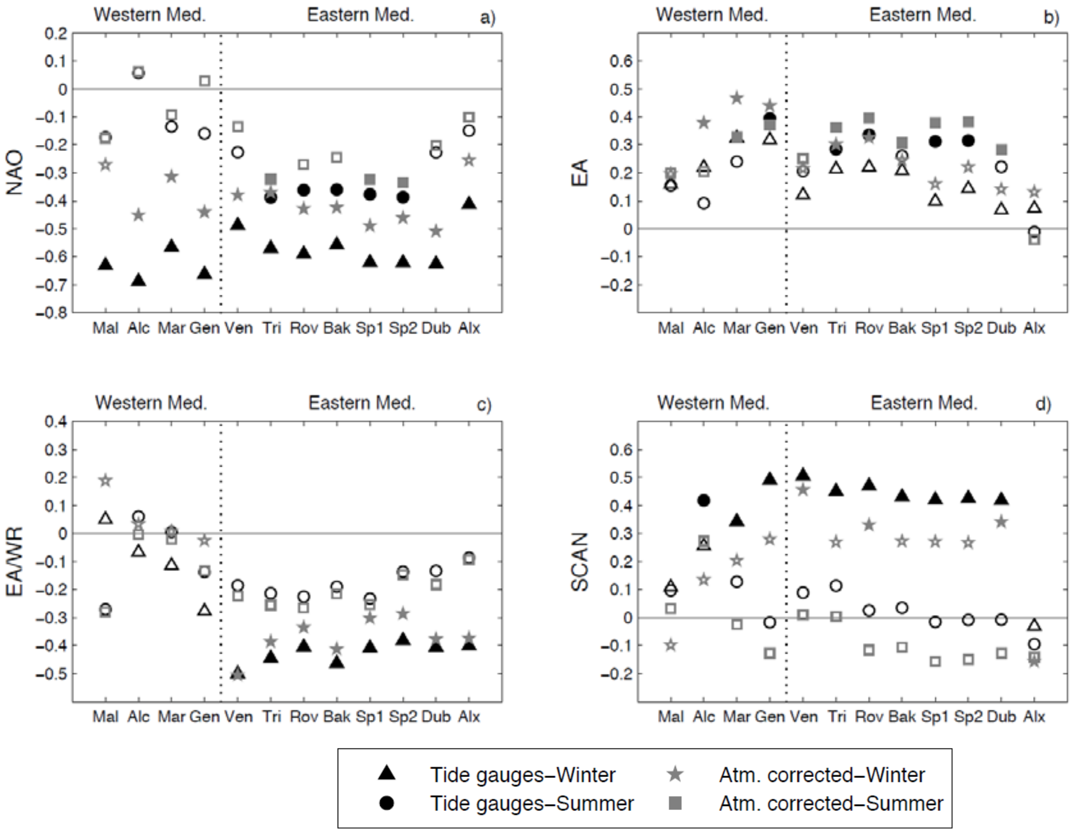

Figure 3.2. Dec-Mar (triangles and stars) and Jun-Aug (circles and squares) correlation coefficients between NAO (a), EA (b), EA/WR (c), SCAN (d) and tide gauges (black) and atmospherically corrected tide gauges (grey) for the common period 1958-2008. Filled symbols denote statistically significance at 95% level. Site names are listed in Table 3.1.

considered redundant by the selection process at most of the tide gauges except in Venice and Rovinj. This is probably a consequence of the inter-dependence of winter averaged NAO and SCAN.

The results of multiple regression indicate that the NAO is the leading mode for winter sea level in the Mediterranean Sea, accounting for 13% to 47% of the variance of observed sea level and for 7% to 26% of the variance of atmospherically corrected sea level. The EA/WR accounts for 6% to 22% in the Adriatic and the eastern sub-basin and conserves similar values when the atmospheric correction is applied (8% to 19%). The EA accounts for 6%-18% of the variance of corrected sea level. Overall, the climate indices account for 39%-56% of the total inter-annual sea level variability in winter and for 14%-41% when the atmospheric correction is applied. The multiple regression models are shown in Fig.3.3.

Table 3.4. The percentage of the variance accounted for by each climatic index at each tide gauge for winter (above) and summer (below) for a regression model in which only one index is the independent parameter. In brackets the corresponding variance for the multiple regression model.

	Variance accounted for							
	Winter sea level				Winter atmospherically-corrected sea level			
	NAO	EA	EA/WR	SCAN	NAO	EA	EA/WR	SCAN
Málaga	40 (40)	3 (0)	0 (0)	1 (0)	7 (0)	4 (0)	4 (0)	1 (0)
Alicante	47 (47)	5 (0)	0.4 (0)	7 (0)	20 (15)	14 (9)	0 (0)	2 (0)
Marseille	32 (29)	10 (7)	1 (0)	12 (0)	10 (7)	22(18)	0 (0)	4 (0)
Genova	44 (43)	10 (0)	8 (6)	24 (0)	19 (14)	19 (14)	0 (0)	8 (0)
Venice	24 (13)	1(0)	25(18)	25 (9)	14 (0)	5 (0)	26 (19)	21 (14)
Trieste	33 (33)	5 (0)	20 (20)	20 (0)	14 (11)	9 (6)	15 (14)	7 (0)
Rovinj	35 (26)	5 (0)	16 (14)	22 (5)	18 (16)	11 (7)	11 (11)	11 (0)
Bakar	32 (32)	4 (0)	22 (22)	19 (0)	18 (18)	6 (0)	17 (17)	7 (0)
Split 1	39 (39)	1 (0)	17 (17)	18 (0)	24 (24)	3 (0)	9 (9)	7 (0)
Split 2	39 (39)	2 (0)	15 (15)	18 (0)	21 (21)	5 (0)	8 (8)	7 (0)
Dubrovnik	40 (40)	0 (0)	17 (17)	18 (0)	26 (26)	2 (0)	14 (14)	12 (0)
Alexandria	17 (16)	1 (0)	16 (15)	0 (0)	7 (0)	2 (0)	14 (14)	2 (0)

	Summer sea level				Summer atmospherically-corrected sea level			
	NAO	EA	EA/WR	SCAN	NAO	EA	EA/WR	SCAN
Málaga	3 (0)	2 (0)	7 (0)	1 (0)	3 (0)	4 (0)	8 (0)	0 (0)
Alicante	0 (0)	1 (0)	0 (0)	18 (18)	0 (0)	4 (0)	0 (0)	7 (0)
Marseille	2 (0)	6 (0)	0 (0)	2 (0)	1 (0)	11 (11)	0 (0)	0 (0)
Genova	3 (0)	16 (16)	2 (0)	0 (0)	0 (0)	14 (14)	2 (0)	2 (0)
Venice	5 (0)	6 (0)	6 (0)	1 (0)	2 (0)	6 (0)	5 (0)	0 (0)
Trieste	15 (15)	8 (0)	5 (0)	1 (0)	10 (0)	13 (13)	7 (0)	0 (0)
Rovinj	13 (10)	11 (8)	5 (0)	0 (0)	7 (0)	16 (16)	7 (0)	1 (0)
Bakar	13 (13)	7 (0)	4 (0)	0 (0)	6 (0)	9 (9)	5 (0)	1 (0)
Split 1	14 (14)	10 (0)	5 (0)	0 (0)	11 (1)	14 (11)	6 (0)	2 (0)
Split 2	15 (15)	10 (0)	2 (0)	0 (0)	11 (7)	15 (11)	2 (0)	2 (0)
Dubrovnik	5 (0)	5 (0)	2 (0)	0 (0)	4 (0)	8 (8)	3 (0)	2 (0)
Alexandria	2 (0)	0 (0)	1 (0)	1 (0)	1 (0)	0 (0)	1 (0)	2 (0)

During summer the influence of climates modes in sea level variability from tide gauges is smaller. In the Adriatic the NAO accounted for 13% to 15% of the variance. The correlation with the other indices seems random (Table 3.4 and Figure 3.3). However, the summer EA accounts for 8% to 16% of the variance at Genova, Marseille and the Adriatic tide gauges when the atmospheric contribution is removed.

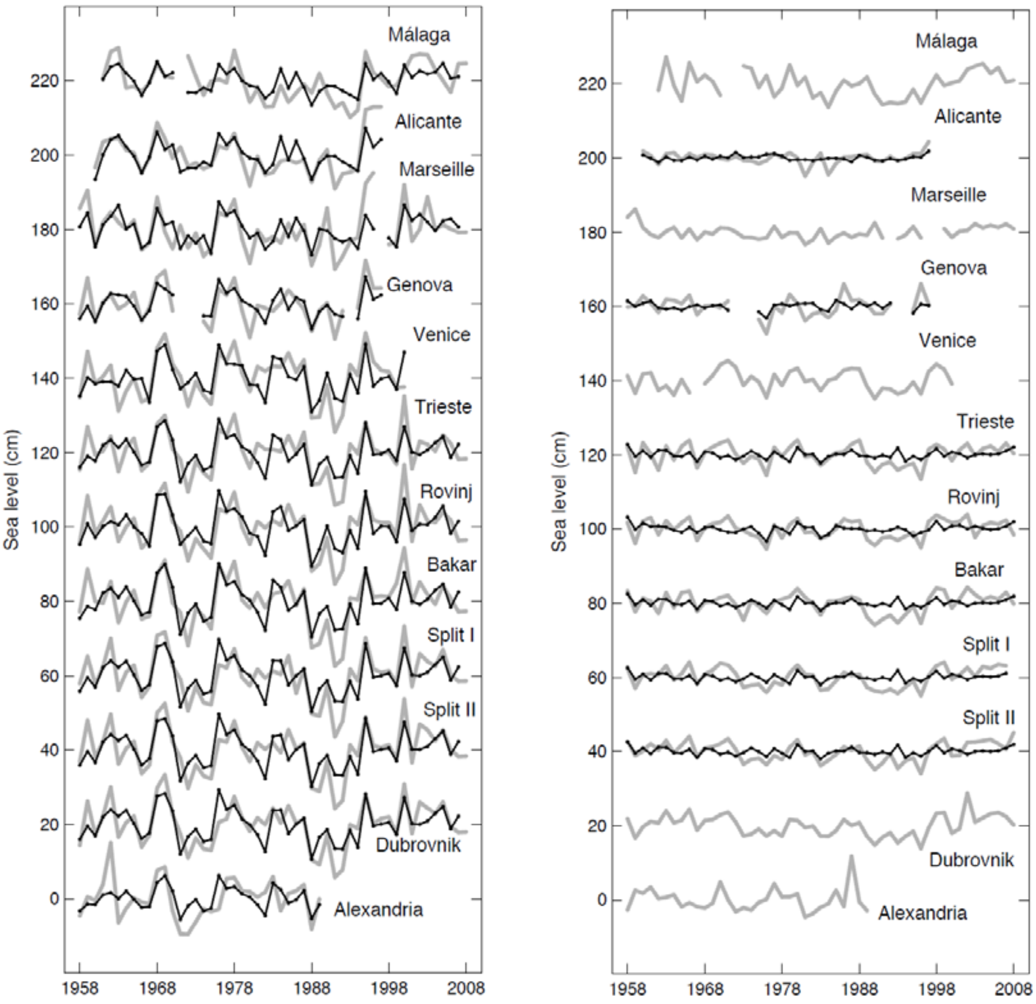

Figure 3.3. Winter (left) and summer (right) sea level at tide gauges (in grey) and time series reconstructed using the multiple regression model (black lines) with the corresponding indices (Figure 3.2 and Table 3.4).

3.4.2 Observed sea level from altimetry

Statistically significant winter correlations between the climate indices and altimetry are mapped in Figure 3.4 (left column). The corresponding basin averaged correlation and the variance accounted for is listed in Table 3.5. Summer maps are not shown because no statistically significant correlation has been identified. The correlations with tide gauges, but computed for the same period as the altimetry are also mapped for completeness (Figure 3.4, left). The highest correlation for basin average was found between altimetry and NAO (-0.91). The correlation with SCAN was slightly lower (0.75).

The multivariate regression model selects the NAO as the independent parameter while the SCAN mode becomes redundant. For this reason the variance accounted for by SCAN is zero in Table 3.5. The winter NAO accounts for 77% of the variance followed by EA/WR (7%) (Table 3.5 and Figure 3.5 top). These values are consistent with the variances of tide gauges accounted for by the indices. However, the NAO accounts for more variance during the altimetric period than for the tide-gauge period whereas the opposite is true for EA/WR.

Note that the EA/WR correlations are below the significance level for most of the domain. Nevertheless it accounts for a small fraction of the variability. The multiple regression model accounts for 83% of the basin averaged winter variance of sea level.

Winter correlations between climate indices and DAC-altimetry are represented in Figure 3.4 (right). The correlations with atmospherically corrected tide gauges are also mapped over the DAC-altimetry maps. Basin and sub-basin averages of correlations and variances accounted for by the indices according to the multiple regression model are listed in Table 3.5. No significant correlations were found in summer (not shown). The highest correlation (in absolute values) was obtained with NAO (-0.9) SCAN having the second largest (0.6). The correlation with EA was also significant over part of the western sub-basin, with an average value of 0.5.

The multiple regression model considered SCAN redundant. The contribution of each independent mode to winter atmospherically-corrected sea level variability averaged over the entire basin is represented in Figure 3.5 (bottom), being the NAO the only significant mode, accounting for 78% of the variance. In the western sub-basin EA accounted for around 12% of the variance.

It is worth to clarify that the difference in winter variances found between tide gauges (32±10 cm2) and altimetry (19±7 cm2) listed in Table 3.3 is attributed to the different periods considered and to the fact that the altimetry average covers the whole basin, while the tide gauge value is point-wise. Indeed, when the winter variance of altimetry is calculated by averaging only the closest grid points to tide gauges and limiting the tide gauge average to the altimetry period this difference is significantly reduced (11±4 cm2 and 14±9 cm2, respectively).

3.4.3 Atmospherically forced sea level

Seasonal correlations between climate indices and atmospherically-induced sea level as given by the barotropic hindcast forced by pressure and wind are mapped in Figure 3.6 for winter (a-d) and summer (i-l). Basin averaged correlations and the corresponding variances accounted for are listed in Table 3.6. With the exception

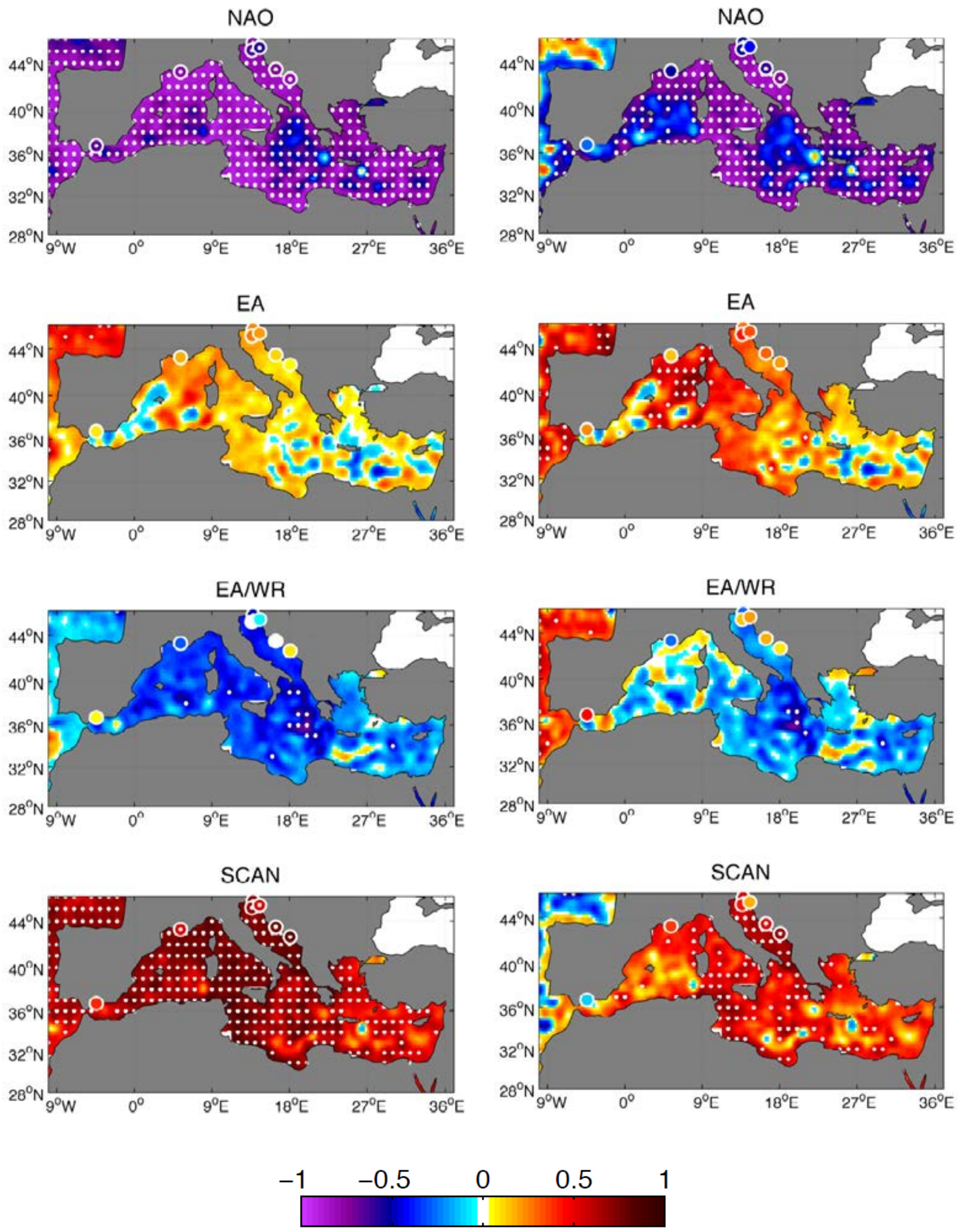

Figure 3.4. Maps of the correlation coefficient between winter climate indices and winter altimetry (left) and DAC-altimetry (right) for the period 1993-2010. Dotted areas denote significant correlation at 95% level. Correlations with tide gauges are also shown for the same period (coloured circles). Only those tide gauges longer than 10 years of data during 1993-2010 are shown.

of the EA, all other are correlated with the winter atmospheric component of sea level. The highest correlation (-0.7) is with NAO. For the winter season about 50% of the variance is accounted for by the NAO index and 11% by the EA/WR. The correlation with SCAN was found redundant. Overall the variance accounted

Table 3.5. Correlation coefficients and the variance accounted for, by the regression model in which each climate index has been regressed against the corresponding sea level parameter. Results for winter are shown. The variance accounted for by the multiple regression model is shown in brackets. Boldface values denote statistically significance at 95% level. Western and Eastern Mediterranean values are also shown.

		NAO		EA		EA/WR		SCAN	
		Corr	EV (%)	Corr	EV (%)	Corr	EV (%)	Corr	EV (%)
Altimetry	Med	**-0.91**	83 (77)	0.1	1 (0)	**-0.36**	13 (7)	**0.75**	56 (0)
	WMed	**-0.9**	81 (76)	0.19	4 (0)	**-0.35**	12 (7)	**0.78**	61 (0)
	EMed	**-0.89**	79 (73)	0.08	1 (0)	**-0.36**	13 (7)	**0.73**	53 (0)
DAC Altimetry	Med	**-0.89**	79 (79)	0.26	7 (0)	-0.2	4 (0)	**0.57**	32 (0)
	WMed	**-0.8**	64 (52)	**0.49**	24 (12)	-0.05	0 (0)	**0.48**	23 (0)
	EMed	**-0.89**	79 (79)	0.21	4 (0)	-0.23	5 (0)	**0.6**	36 (0)

for by the climate modes was about 60%. The statistical model for the averaged basin sea level for the NAO alone and the NAO and EA/WR are shown in Figure 3.7 (top). It must be remarked however, that the atmospherically-induced sea level variability is much smaller in summer than in winter; thus, the impacts of the climate modes are also smaller in absolute terms.

During summer, SCAN explains 14% of the variance; the other modes do not show statistically significant correlations (Table 3.6). Despite the low correlation obtained with NAO (-0.19 over the basin), this mode accounts for 8% of the variability in the eastern sub-basin, according to the regression model. The corresponding time series of the summer atmospherically-induced sea level and the regression model are plotted in Figure 3.7 (bottom).

Regression and correlation analysis was also performed for wind-only and pressure-only forced sea level (Table 3.6). Seasonal correlations for wind-only forced sea level are mapped at Figure 3.6 for winter (e-h) and summer (m-p). During winter, the NAO is the leading mode for wind and pressure only forced sea level with very similar basin averaged correlations (–0.67 and 0.68) and corresponding variances accounted for between 45% and 49%.

For the multiple regression model of pressure-only forced sea level all four independent modes contribute to winter basin-averaged sea level variability, reaching an overall value of 60%.

For the multiple regression model for wind-only forced sea level the EA/WR is the only pattern which, together with NAO, contributed to the winter variance

(51%). Although both EA and SCAN were correlated with wind sea level component at western subbasin and overall the basin, respectively, they were considered redundant.

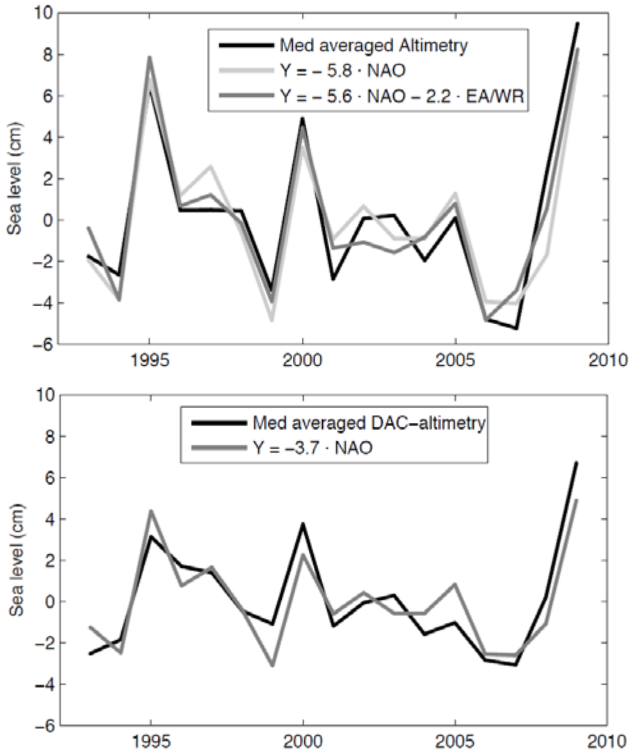

Figure 3.5. Overall contribution of independent modes to winter basin average altimetry (top) and winter basin average DAC-altimetry (bottom).

Results for the summer season are different. The pressure only forced sea level is correlated with NAO at some areas of northern Adriatic and at 20-30ºE area of Eastern sub-basin, while SCAN is correlated at western sub-basin. Interestingly, sea level forced by wind only in summer is correlated only to the EA mode in almost all of the basin. However the variance accounted for is only 9%.

3.4.4 Thermosteric sea level

Thermosteric sea level has much smaller variance than the observed sea level and the atmospherically-corrected sea level (Table 3.3). Thus any significant correlation found should be interpreted in this context.

The results for winter correlations between climate indices and thermosteric sea level are represented in Figure 3.8 (left) and Table 3.7. During winter, SCAN is the index that displays higher correlation, concentrated over the central and eastern regions of the Mediterranean, with an average value of 0.30. SCAN explains about 9% of the winter basin averaged thermosteric sea level variance. NAO is also correlated with the thermosteric sea level over a fraction of the eastern sub-basin. The time series of the averaged thermosteric sea level and the resulting regression models are plotted in Figure 3.9. No significant correlations were found for the summer.

Changes in thermosteric sea level, at each part of the basin, result from atmospheric heat fluxes and lateral heat advection. Significant correlation (0.59) was found between net heat fluxes and the seasonal average of the time derivative of thermosteric sea level (0.59) averaged over the basin for the period 1950-2008. Note that the seasonal average of the time derivative of thermosteric sea level is the change in thermosteric sea level between November and March divided by four, and between August and May divided by three. The correlations with indices during winter and summer are mapped in Figure 3.8 (center and right columns) and the averaged correlations and variances accounted for are listed in Table 3.7. During winter, only EA is correlated over most of the western sub-basin and over the Adriatic with an average value of 0.49 over all the basin. EA/WR shows correlations in the most western and eastern parts of Mediterranean. However, the averaged values have opposite sign depending on the sub-basin (0.30 and -0.22, respectively). SCAN show correlations only in the central parts of the eastern sub-basin (0.30). EA is the only mode that explains part of the variance of the winter basin averaged rate of change of thermosteric (17%). However, combined with EA/WR account for a 21% of the variability of the basin, while combined with EA/WR and SCAN account for the 23% of the eastern averaged. These results are consistent with Josey et al (2011) who showed that EA is the mode driving air-sea net heat fluxes variability over the Mediterranean, especially over western sub-basin, while the NAO and SCAN play much smaller role; EA/WR also plays an important role, but generates a dipole with opposite signal on western and eastern sub-basins. During summer only EA/WR is correlated with thermosteric rate of change at the south part of the eastern sub-basin, however it is correlated with the basin averaged (-0.35) accounting for 12% of the variance. SCAN appears correlated at southern part of the western sub-basin (-0.29), where it explains about 9% of the variance.

3.5 Discussion

The Mediterranean Sea level variance is larger in winter than in the summer. According to altimetry it is about three times larger; according to coastal tide gauge records it is about five times larger. The statistical modelling of this

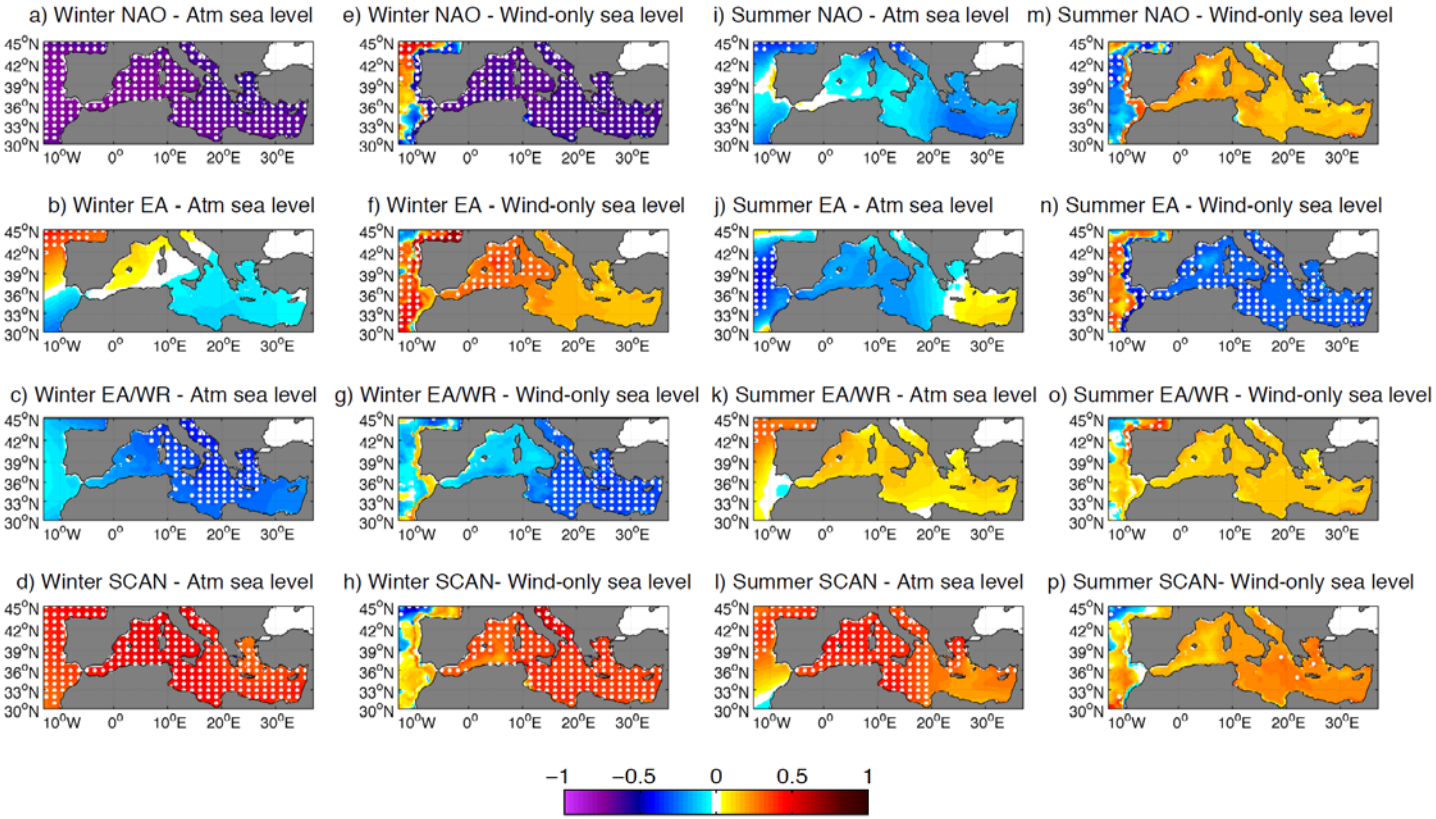

Figure 3.6. Dec-Mar and Jun-Aug maps of correlation coefficients between climate modes and atmospherically-induced sea level and wind-only induced sea level for the period 1958-2008. Dotted areas denote significant correlation at 95% level.

Table 3.6. Correlation coefficients and the variance accounted for, by the regression model in which each climate index has been regressed against the atmospherically-induced sea level, pressure only-induced sea level and wind only-induced sea level. Results for winter (above) and summer (below) are shown. The variance accounted for by the multiple regression model is shown in brackets. Boldface values denote statistically significance at 95% level. Western and Eastern Mediterranean values are also shown.

		NAO		EA		EA/WR		SCAN	
		Corr	EV (%)	Corr	EV (%)	Corr	EV (%)	Corr	EV (%)
Winter Atmospheric	Med	**-0.71**	50 (50)	-0.01	0 (0)	**-0.32**	10 (11)	**0.47**	22 (0)
	Wmed	**-0.73**	53 (42)	0.03	0 (0)	**-0.26**	7 (5)	**0.49**	24 (4)
	Emed	**-0.67**	45 (45)	-0.04	0 (0)	**-0.35**	12 (13)	**0.43**	18 (0)
Winter Pressure-only	Med	**-0.68**	46 (49)	-0.12	1 (4)	**-0.33**	11 (12)	**0.47**	22 (0)
	Wmed	**-0.70**	49 (38)	-0.06	0 (0)	**-0.30**	9 (7)	**0.51**	26 (5)
	Emed	**-0.63**	39 (44)	-0.15	2 (6)	**-0.35**	12 (13)	**0.4**	16 (0)
Winter Wind-only	Med	**-0.67**	45 (45)	0.21	4 (0)	-0.25	6 (7)	**0.42**	18 (0)
	Wmed	**-0.67**	45 (45)	**0.28**	8 (0)	-0.10	1 (0)	**0.34**	12 (0)
	Emed	**-0.65**	42 (42)	0.17	3 (0)	**-0.30**	9 (9)	**0.44**	19 (0)
Summer Atmospheric	Med	-0.19	4 (0)	-0.1	1 (0)	0.09	1 (0)	**0.38**	14 (14)
	Wmed	-0.09	1 (0)	-0.18	3 (0)	0.12	1 (0)	**0.41**	17 (17)
	Emed	-0.22	5 (8)	-0.07	0 (0)	0.07	0 (0)	**0.35**	12 (16)
Summer Pressure-only	Med	**-0.30**	9 (13)	0.03	0 (0)	0.04	0 (0)	**0.34**	12 (16)
	Wmed	-0.21	4 (8)	-0.08	1 (0)	0.09	1 (0)	**0.42**	18 (22)
	Emed	**-0.32**	10 (14)	0.07	0 (0)	0.02	0 (0)	**0.31**	10 (13)
Summer Wind-only	Med	0.14	2 (0)	**-0.31**	10 (10)	0.12	1 (0)	0.21	4 (0)
	Wmed	0.19	4 (0)	**-0.29**	8 (8)	0.13	2 (0)	0.18	3 (0)
	Emed	0.12	1 (0)	**-0.31**	10 (10)	0.12	1 (0)	0.22	5 (0)

variance on multiple regression models both for tide gauges and altimetric data show that the NAO can account for most of the winter variability. The use of the atmospherically forced sea level hindcast shows that the NAO influence is due both to the atmospheric pressure forcing and to wind forcing. The sea level correlation with the NAO remains after the DAC correction is applied. This means that the NAO influence on the Mediterranean is not restricted to the local atmospheric pressure and wind effects.

Although SCAN and NAO are monthly independent, they are correlated in winter. All modes show influence in the pressure driven part of the atmospheric forcing, hardly surprising as they are determined on the basis of pressure changes. However only the NAO and SCAN are correlated with the wind driven part of sea level in the winter. The EA is the only mode influencing the wind driven sea

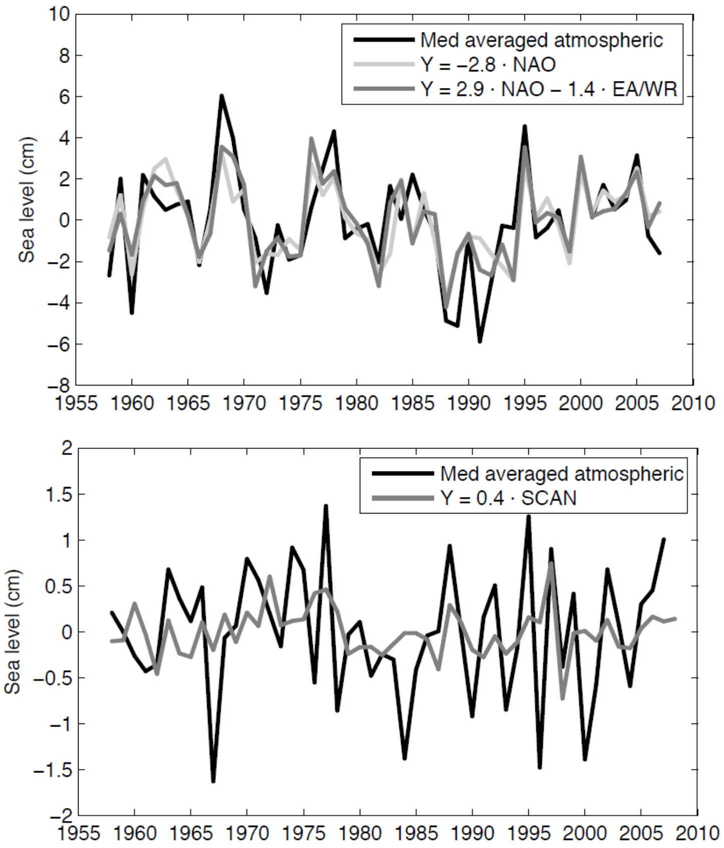

Figure 3.7. Overall contribution of independent modes to winter (top) and summer (bottom) basin average atmospherically induced sea level variability.

level in the whole of the Mediterranean Sea during the summer season.

The relationship between thermosteric sea level and the other large scale climate modes considered in this study is not clearly demonstrated and the results found are spatially restricted to certain areas. Changes in the seasonally averaged rate of change of the thermosteric sea level can be partly accounted for by the EA (21% in winter and 12% in summer) but with differences between the western and eastern sub-basins. The physical mechanisms through which the atmospheric climate modes impact on Mediterranean sea level and its contributions can be discussed further using composite maps of anomalies of sea level components, wind speed and mean sea level pressure for each pattern corresponding to index values higher than 1.5 or lower than -1.5.

Figure 3.10 shows the composite maps of atmospherically forced winter sea level during the positive and negative NAO phases and the corresponding map for EA/WR, the only two indices we found accounting for the variance in the relevant multiple regression model. Note that pressure and winds mapped here are not anomalies as in Figure 3.1. The spatial pattern of the atmospheric component

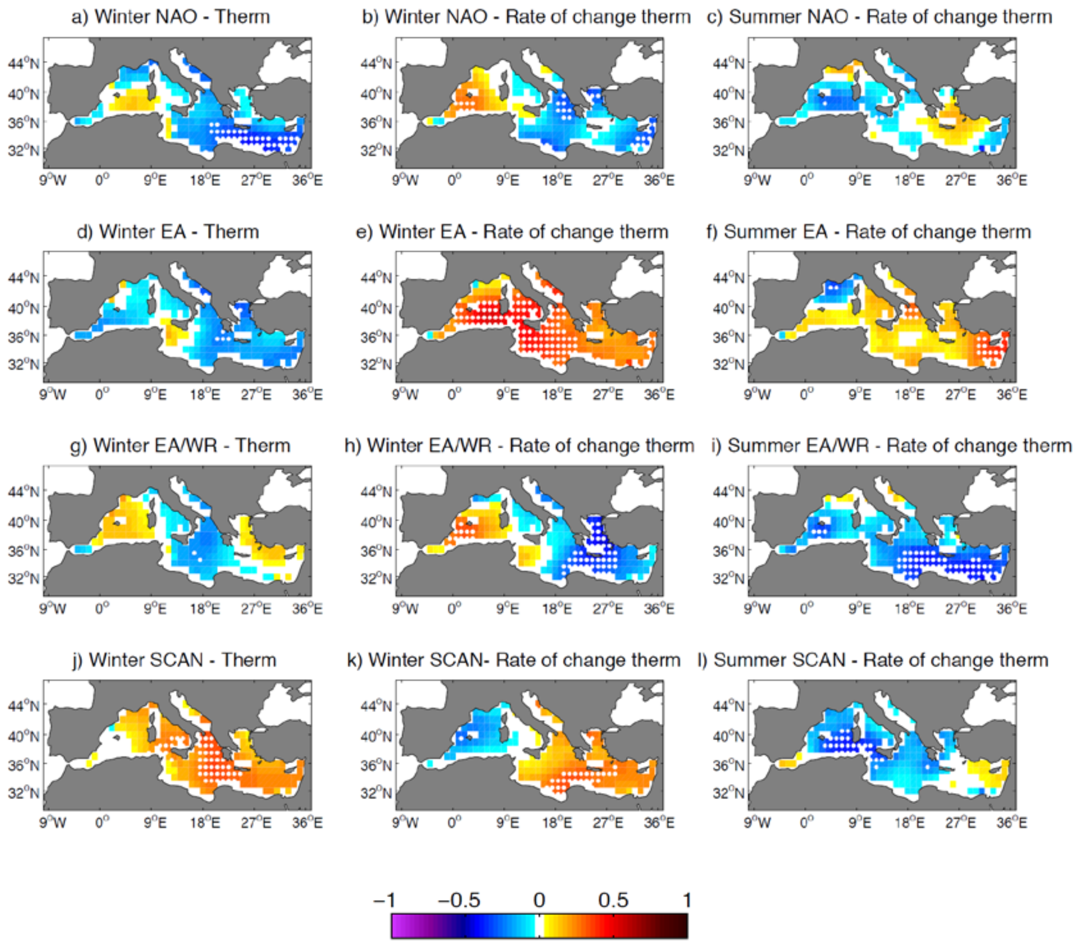

Figure 3.8. Dec-Mar and Jun-Aug maps of correlation coefficients between the climate indices and the thermosteric sea level (left) and the rate of change of thermosteric sea level (center and right) for the period 1950-2011. Dotted areas denote significant correlation at 95% level.

of sea level reflects that of the atmospheric pressure: during a positive phase atmospheric pressure displays a meridional gradient with lower values in the eastern sub-basin mimicked by the sea level response. On the contrary, during a negative NAO phase, atmospheric pressure is lower and more homogeneous within the basin and consequently sea level values are higher. The winds associated with the NAO mode contribute in the same sense than atmospheric pressure to the atmospherically-induced winter sea level. Fukumori et al. (2007) have shown that winds around the Strait of Gibraltar can produce significant basin-wide oscillations in the Mediterranean. Winds associated to the NAO negative phase are prone to induce a net mass flux through the Strait of Gibraltar, so inducing a sea level increase in the basin (Fukumori et al., 2007).

Table 3.7. Correlation coefficients and the variance account for, by the regression model in which each climate index has been regressed against the thermosteric sea level and the monthly rate of change of thermosteric sea level. Results for winter are shown. Results for summer are shown only for the rate of change of thermosteric. The variance accounted for by the multiple regression model is shown in brackets. Boldface values denote statistically significance at 95% level. Western and Eastern Mediterranean values are also shown.

		NAO		EA		EA/WR		SCAN	
		Corr	EV (%)	Corr	EV (%)	Corr	EV (%)	Corr	EV (%)
Winter Thermosteric	Med	-0.23	5 (0)	-0.20	4 (0)	-0.04	0 (0)	**0.30**	9 (9)
	Wmed	-0.02	0 (0)	-0.10	1 (0)	0.05	0 (0)	0.15	2 (0)
	Emed	**-0.28**	8 (0)	-0.21	4 (6)	-0.06	0 (0)	**0.32**	10 (12)
Winter Rate of change	Med	-0.18	3 (0)	**0.49**	24 (17)	-0.22	5(4)	0.21	4 (0)
	Wmed	0.09	1 (0)	**0.44**	19 (16)	0.10	1 (0)	-0.14	2 (0)
	Emed	**-0.25**	6 (0)	**0.40**	16 (11)	**-0.30**	9 (6)	**0.30**	9 (4)
Summer Rate of Change	Med	0.06	0 (0)	0.13	2 (0)	**-0.35**	12 (12)	-0.19	3 (0)
	Wmed	-0.05	0 (0)	-0.06	0 (0)	-0.09	1 (0)	**-0.29**	9 (9)
	Emed	0.09	1 (0)	0.18	3 (0)	**-0.37**	14 (14)	-0.09	1 (0)

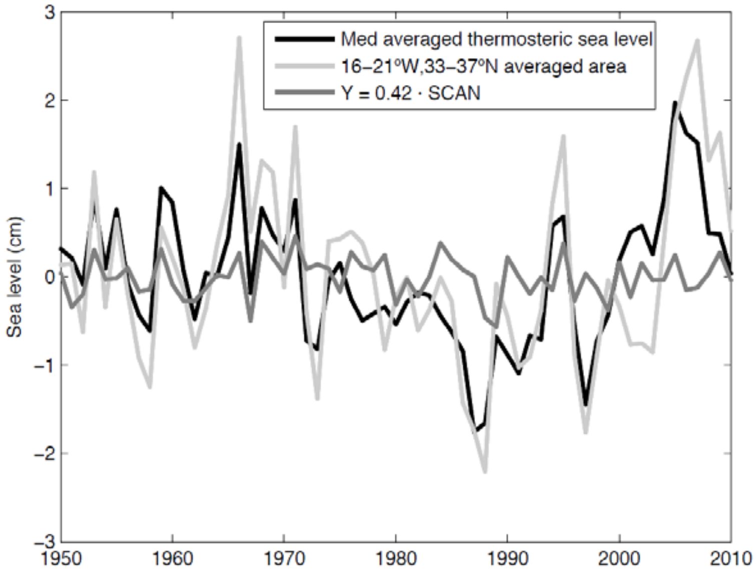

Figure 3.9. Dec-Mar contribution of the SCAN to the winter basin averaged thermosteric sea level. Averaged thermosteric sea level of the highest correlated area is also shown for comparison (light-grey line).

The second mode correlated with winter sea level and its atmospheric component, in the multiple regression model, was the EA/WR. This mode was

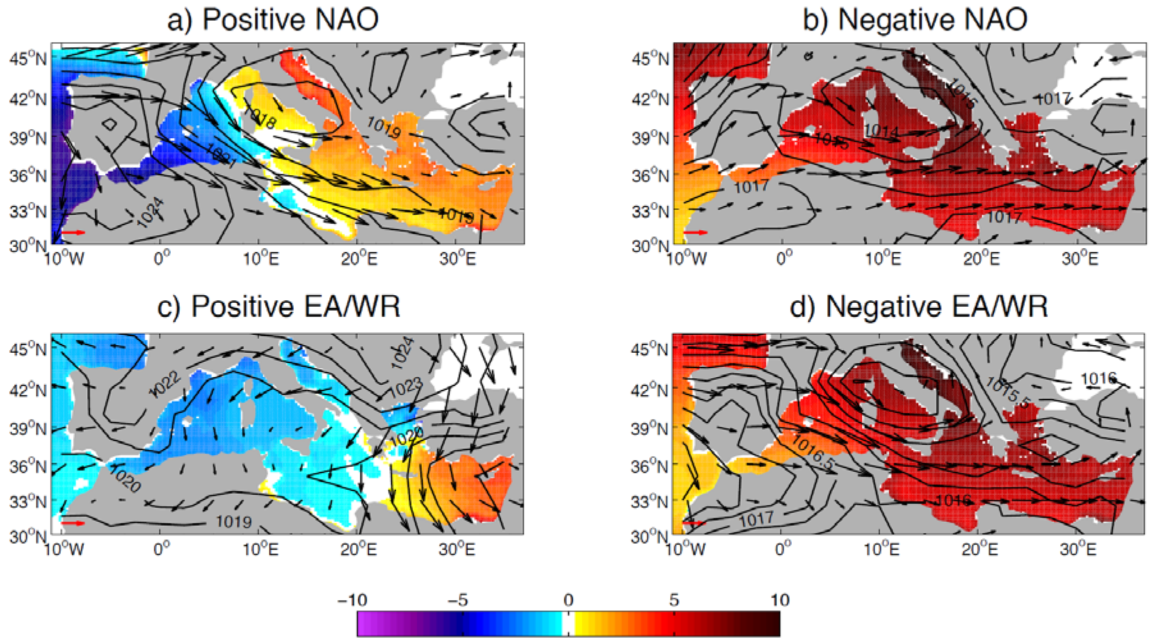

Figure 3.10. Winter (Dec-Mar) atmospherically-induced sea level (cm) and 10m wind speed (vectors) averaged for a winter NAO (top) and EA/WR (bottom) indices: (a,c) positive state, (b,d) negative state. Corresponding averaged sea level pressures are contoured in intervals of 1 mb. Note that the horizontal vector (red arrow) is for scale and indicates a wind speed of 2m/s.

not significant for the atmospherically-corrected sea level (Table 3.5), indicating thus that the influence on sea level was exclusively through the atmospheric pressure and the local wind forcing. Wind anomalies composites (Figure 3.1) suggested that positive phases of EA/WR favour northerly strong winds, over the eastern basin. During a positive phase of EA/WR, the atmospherically-induced sea level associated with this mode displays an E-W gradient in response to the atmospheric pressure pattern over the Mediterranean (Figure 3.10c). During the negative phase of EA/WR (Figure 3.10d), the spatial pattern of atmospherically-induced sea level is more uniform and dominated by westerly winds.

In Figure 3.11 composite maps for the anomalies in the rate of change of thermosteric sea level are shown. As seen previously (Fig. 3.8), the NAO is only correlated with parts of the Eastern Mediterranean. The winter EA is the mode most closely correlated with the rate of change of thermosteric sea level. This is despite the fact that the EA does not correlate with atmospherically-induced sea level in general but does correlate with the wind driven part of the sea level. The underlying correlation between the wind field over the Mediterranean and the EA is important for the heat fluxes. In its positive phase, EA is characterized by an atmospheric pressure anomaly pattern with very weak gradients over the

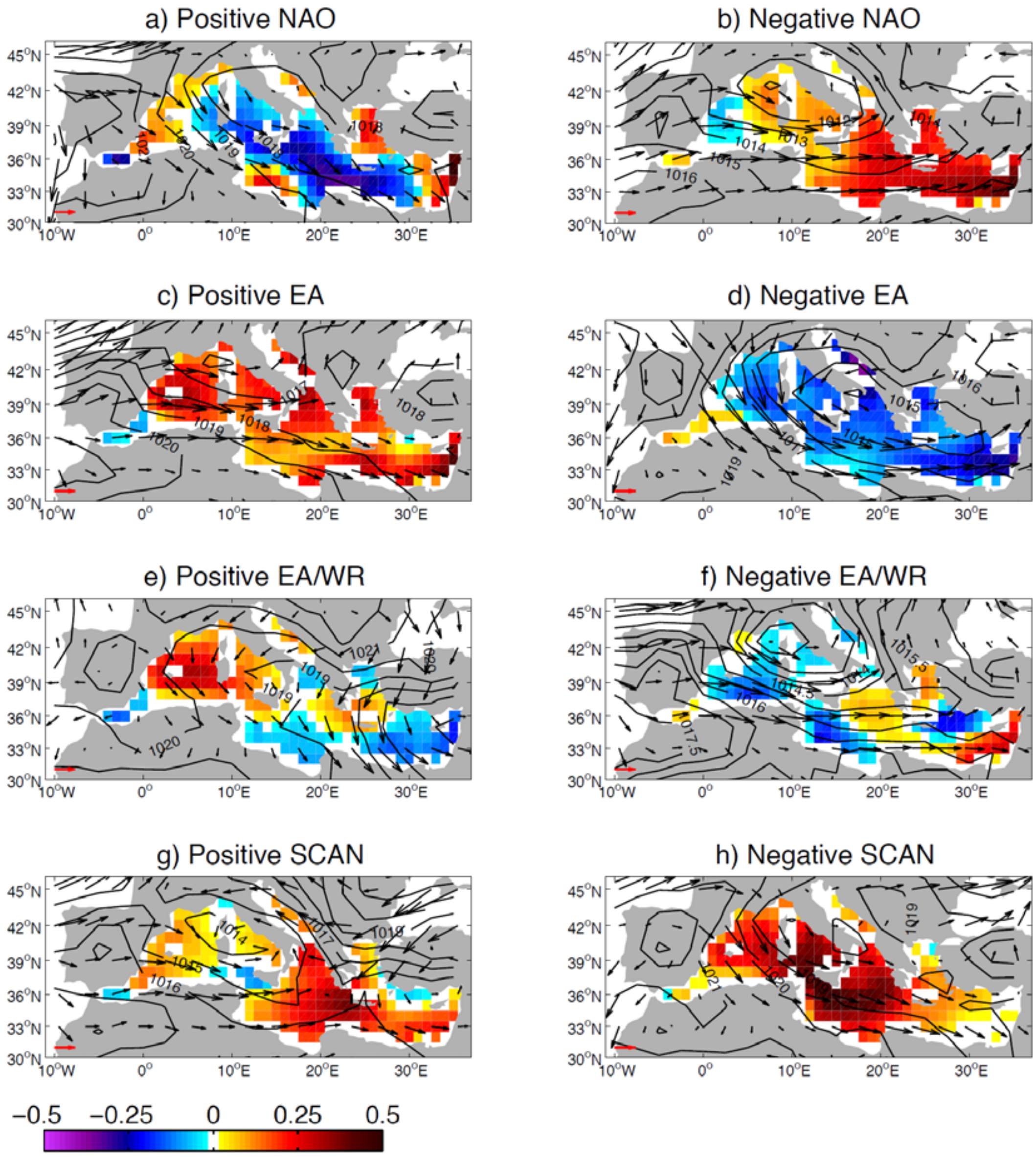

Figure 3.11. Winter (Dec-Mar) rate of change of thermosteric sea level anomalies (cm) and 10m wind speed (vectors) averaged for winter NAO (a,b), EA (c,d), EA/WR (e,f) and SCAN (g,h) indices under a positive state (left) and a negative state (right). Corresponding averaged sea level pressures are contoured in intervals of 1 mb. Note that the horizontal vector (red arrow) is for scale and indicates a wind speed of 2m/s.

Mediterranean Sea and the nearby Atlantic (Figure 3.1). The circulation associated with the positive EA state involved westerly winds coming from the Atlantic, while the negative phase northerly winds coming over the Gulf of Lions, in agreement with the results presented by Josey et al (2011). As heat fluxes are always negative in winter, this translates into smaller than average heat losses,

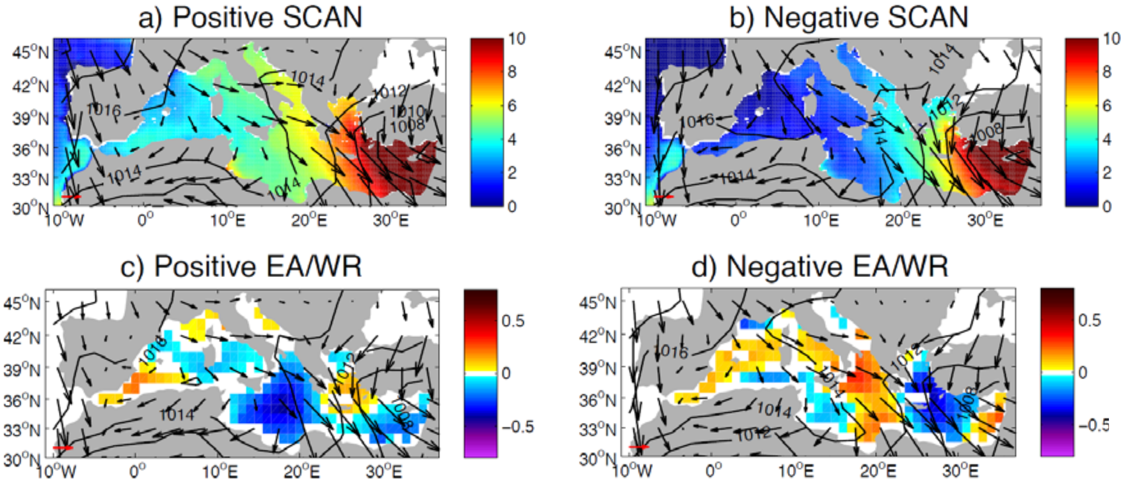

Figure 3.12. Summer (Jun-Aug) atmospherically induced sea level (cm) averaged for a summer SCAN positive and negative phases (above). Rate of change of thermosteric sea level anomalies (cm) averaged for a summer EA/WR positive and negative phases (below). Corresponding 10m wind speed (vectors) and sea level pressure are contoured in intervals of 1 mb. Note that the horizontal vector above Figure 3.12a is for scale and indicates a wind speed of 2m/s.

especially over the western sub-basin (Figure 3.11c). Likewise, the EA negative phase in winter is associated with northerly winds and colder air T, resulting in larger than average ocean heat losses and more negative anomalies of the rate of change of thermosteric sea level (Figure 3.11d). The rates of change of thermosteric sea level were found to be also related with EA/WR and SCAN at some areas of the basin (Table 3.7 and Figure 3.11).

The associated with EW/WR winter wind fields show that during the positive phase of EA/WR northerly winds bring cold air over some areas of the eastern sub-basin resulting in a higher than normal heat loss (Figure 3.11e) while in the western part of the basin winds coming from the west contributes to a lower than normal heat loss. The opposite effect occurs during the negative phase of EA/WR, when a westerly flow of warmer air contributes to decreasing the rates of change of the thermosteric component (Figure 3.11f). The positive phase of SCAN is associated with a westerly flow of warm air that induces lower than normal decreasing of thermosteric sea level, mostly over the central-eastern Mediterranean. In its negative phase, there is a pattern of warmer north-westerly winds due to the absence of the low-pressure conditions over the western sub-basin and the result is a much lower decreasing of thermosteric sea level than in the positive phase.

Table 3.8. Variance accounted for by the regression model in which each climate index has been regressed against the sea level and its components for the altimetry period (1993-2008). The variances of the altimetric sea level accounted for by the atmospheric and thermosteric components are also shown. Results for winter and summer are shown. The variance accounted for by the multiple regression model is shown in parentheses. The lowest and highest variances accounted for by each tide gauge are also shown for the altimetry period (in brackets).

	Altimetry		DAC-Altimetry		Atmospheric component		Thermosteri component		Tide gauges		Atm-corrected tide gauges	
	Win	Sum	Win	Sum	Win	Sum	Win	Sum	Win	Sum	Win	Sum
NAO (%)	86(86)	0(0)	72(72)	0(0)	70(0)	1(0)	2(0)	6(0)	[31-64]([0 45])	[0-15]	[7-56]([0-54])	[0-2](0)
EA (%)	0(0)	5(0)	1(0)	3(0)	3(0)	0(0)	0(0)	6(0)	[0-4](0)	[0-16]	[2-14](0)	[0-7](0)
EA/WR (%)	1(0)	0(0)	0(0)	1(0)	2(0)	2(0)	19(0)	2(0)	[0-7](0)	0	[0-5](0)	[0-3](0)
SCAN (%)	60(0)	0(0)	25(0)	1(0)	80(80)	10(0)	2(0)	0(0)	[10-65]([0 63])	[0-18]	[1-37](0)	[0-5](0)
Atmospheric Component (%)	74	42	-	-	-	-	-	-	-	-	-	-
Thermosteric Component (%)	0	0	0	1	-	-	-	-	-	-	-	-

During the summer season, SCAN was the only relevant mode for summer atmospherically-induced sea level, accounting for only 14% of the variance (1.0±0.2 cm2) on average over the basin. Figure 3.12a and 2.12b show that the mechanism through which the SCAN pattern impacts on the atmospheric contribution is its associated atmospheric pressure pattern for both the positive and negative phases, as the atmospherically-induced pattern follows that of the atmospheric pressure. EA/WR and, to a lesser extent, SCAN patterns influenced the rates of change of thermosteric sea level during summer. For both positive and negative phases, EA/WR induce northerly winds over the Mediterranean (Figure 3.12c, d); however, air T over Europe is colder (warmer) than average during the summer positive (negative) phase (not shown), which explains lower (higher) rates of change of thermosteric sea level.

3.6 Conclusions

The four independent large scale modes dominating the atmospheric variability over the North Atlantic and Europe (NAO, EA/WR, SCAN and EA), impact differently on sea level and its components. Table 3.8 summarizes the results presented throughout the paper for each sea level contribution.

The major conclusions of this work are summarized in the following:

- The NAO is the main mode in terms of impacts on winter Mediterranean sea level variability (-5.6 cm of altimetry sea level per unit NAO with a correlation of -0.91) as a result of two physical processes that contribute to amplify the atmospheric signal: i) the direct forcing of atmospheric pressure and wind within the basin (-2.9 cm per unit NAO with a correlation of -0.71) which induces changes in the flux through Gibraltar, and ii) the forcing of Gibraltar mass exchanges caused by winds near the Strait. In addition Calafat et al. (2012) demonstrated that wind driven baroclinic circulation in the Atlantic also impact on Mediterranean sea level. Positive/negative winter NAO phases induce lower/higher Mediterranean sea level as a result of these two mechanisms.

- The SCAN pattern is significantly correlated with winter Mediterranean sea level (0.89). However, it has been found to be redundant with winter NAO, as the atmospheric patterns associated with these two modes are very similar over the Mediterranean (confirmed by the correlation between winter NAO and SCAN modes). Otherwise, SCAN is the only mode that contributes to the winter thermosteric sea level with 0.4 cm per unit index.

- EA/WR is the second large scale mode in importance for Mediterranean sea level (-2.2 cm of altimetry sea level per unit index and a correlation of -0.36) , and acts mainly by forcing the atmospheric sea level component, more particularly by atmospheric pressure changes.

- The EA mode impacts on the rate of change in winter thermosteric sea level.

- In summer the variance of atmospherically induced sea level is much lower than in winter (1.0±0.2 cm2). SCAN is correlated with atmospheric summer sea level (0.38, 0.6 cm/unit) and the effect is solely attributed to pressure. The EA is the only mode that contributes to the wind-only induced sea level (-0.31) with -0.2 cm per unit index but the correlation is not significant for the atmospheric component as a whole or for the observed sea level.

This work demonstrates that the study of the large-scale atmospheric variability can help to understand sea level changes at a regional scale, at least for some of the sea level components. Most notably, this is the first study that offers a complete overview of the relationships between the major large-scale atmospheric patterns and Mediterranean sea level and its components over the last decades. Our results provide both the relative and overall contribution of atmospheric patterns to sea level variability in Mediterranean Sea, an information that could be used for the study of past and future scenarios.

Acknowlegdments

This work has been carried out in the framework of the projects VANIMEDAT-2 (CTM2009-10163-C02-01, funded by the Spanish Marine Science and Technology

Program and the E-Plan of the Spanish Government) and ESCENARIOS (funded by the Agencia Estatal de METeorología). A. Martínez-Asensio acknowledges an FPI grant associated with the VANIMEDAT-2 project, M. Marcos acknowledges a “Ramón y Cajal” contract funded by the Spanish Government and G. Jordà acknowledges a JAE-Doc contract funded by the Spanish Research Council (CSIC) and the European Science Foundation. We are grateful to Météo-France for providing atmospheric reanalyses. Finally we thank A. Sánchez-Román for his comments and data providers such as AVISO for providing altimetry data, PSMLS for tide gauges data and NOAA for the climate indices and the atmospheric reanalysis. We thank Piero Lionello and another anonymous reviewer for their constructive comments.

Bibliography

Ablain, M., Philipps, S., Urvoy, M., Tran, N. and Picot,N., 2012. Detection of Long-Term Instabilities on Altimeter Backscatter Coefficient Thanks to Wind Speed Data Comparisons from Altimeters and Models. Marine Geodesy 35:sup1, 258-275

Barnston, Anthony G., Robert E. Livezey, 1987. Classification, Seasonality and Persistence of Low-Frequency Atmospheric Circulation Patterns.Mon. Wea. Rev., 115, 1083–1126.

Calafat, F. M., G. Jordà, M. Marcos, and D. Gomis, 2012. Comparison of Mediterranean sea level variability as given by three baroclinic models, J. Geophys. Res., 117.

Cazenave A., Cabanes, C., Dominh, K. & Mangiarotti, S., 2001. Recent sea level changes in the Mediterranean Sea revealed by TOPEX/POSEIDON satellite altimetry, Geophys. Res. Lett., 28(8), 1607–1610.

Church, J. A. and N.J. White, 2011. Sea-level rise from the late 19th to the early 21st Century. Surveys in Geophysics, 32, 585-602.

Criado-Aldeanueva, F., Del Río Vera, J., García-Lafuente, J., 2008. Steric and mass-induced Mediterranean sea level trends from 14 years of altimetry data, Global and Planetary Change, 60, 3–4.

Draper, N. R. and Smith. H., 1998. Applied Regression Analysis. Hoboken, NJ: Wiley-*Interscience, 1998. pp. 307–312.*

Fenoglio-Marc, L., 2001. Analysis and representation of regional sea-level variability from altimetry and atmospheric–oceanic data. Geophys. J. Int., 145. 1–18.

Fenoglio-Marc, L., Mariotti, A., Sannino, G., Meyssignac, B., Carillo, A., Struglia, M.V., Rixen, M. 2013. Decadal variability of net water flux at the Mediterranean Sea Gibraltar Strait, Global and Planetary Change, 100, 1-10.

Fukumori , Menemenlis, D. and Lee, T. 2007. A Near-Uniform Basin-Wide Sea Level Fluctuation of the Mediterranean Sea. Journal of Physical Oceanography 37:2, 338-358

Gomis, D., Tsimplis, M.N., Marcos, M., Fenoglio-Marc, L., Pérez, B., Raicich F., Vilibić I., Wöppelmann, G., Monserrat S., 2011. Sea Level Rise and its Forcing in the Mediterranean Sea. In: The Mediterranean climate from the present to the future, Lionello P. (ed.), Elsevier.

Gomis, D., S. Ruiz, M. García-Sotillo, E. Álvarez-Fanjul, and J. Terradas 2008. Low frequency Mediterranean sea level variability: The contribution of atmospheric pressure and wind, Global Planet. Change, 63, 215-229.

Ishii, M. and M. Kimoto, 2009: Reevaluation of Historical Ocean Heat Content Variations With An XBT depth bias Correction. J. Oceanogr. 65, 287299, doi:10.1007/s10872-009-0027-7.

Jordà, G., Gomis, D., 2013. Reliability of the steric and mass components of Mediterranean sea level as estimated from hydrographic gridded products. Geophys. Res. Letters (40) 1–6, doi:10.1002/grl.50718

Jordà, G., Gomis, D., Álvarez-Fanjul, E., 2012. The VANI2-ERA hindcast of sea-level residuals: Atmospheric forcing of sea-level variability in the Mediterranean Sea (1958-2008). Scientia Marina, 76, 133-146.

Josey, S. A., S. Somot, and M. Tsimplis. 2011. Impacts of atmospheric modes of variability on Mediterranean Sea surface heat exchange, J. Geophys. Res., 116, C02032, doi:10.1029/2010JC006685

Kistler, R., E. Kalnay, W. Collins, S. Saha, G. White, J. Wollen, M. Chelliah, W. Ebisuzaki, M. Kanamitsu, V. Kousky, H. van den Dool, R. Jenne, and M. Fioriono, 2001: The NCEP/NCAR 50-year reanalysis: Monthly means CD-ROM and documentation. Bull. Am. Meteorol. Soc., 82, 247–267

Mariotti, A, Struglia, M. V., Zeng, N. and Lau, K-M., 2002: The Hydrological Cycle in the Mediterranean Region and Implications for the Water

Budget of the Mediterranean Sea. J. Climate, 15, 1674–1690.

Raicich, F., N. Pinardi, A. Navarra, 2003. Teleconnections between Indian monsoon and Sahel precipitation and the Mediterranean.Int. J. Clim., 23, 173-186

Suselj, Kay, Tsimplis, Michael N., Bergant, Klemen, 2008. Is the Mediterranean Sea surface height variability predictable? Phys.And Chem. Of the Earth, 33, 3-4, 225-238 DOI: 10.1016/j.pce.2006.12.001

Tsimplis MN, Baker TF (2000). Sea level drop in the Mediterranean Sea: an indicator of deep water salinity and temperature changes. Geophys. Res. Lett. 27(12):1731-1734.

Tsimplis, M.N. and S.A. Josey, 2001. Forcing of the Mediterranean Sea by Atmospheric Oscillations over the North Atlantic. Geophysical Research Letters,28(5), 803-806.

Tsimplis, M.N. and M. Rixen, 2002, Sea Level in the Mediterranean Sea: The contribution of temperature and salinity changes, Geophys. Res. Let.,29(23), 2136-2140.

Tsimplis, M.N., A.G.P. Shaw, 2008. The forcing of mean sea level variability around Europe. Global and Planetary Change 63, 196–202, doi:10.1016/j.gloplacha.2007.08.018.

Tsimplis, M., Shaw, A., Flather, R. and Woolf, D. 2006. The influence of the North Atlantic Oscillation on the sea level around the northern European coasts reconsidered: the thermosteric effects. Phil. Trans. R. Soc. A.364(1841), 845–856.

Tsimplis, M. N., F. M. Calafat, M. Marcos, G. Jordà, D. Gomis, L. Fenoglio-Marc, M. V. Struglia, S. A. Josey, and D. P. Chambers (2013), The effect of the NAO on sea level and on mass changes in the Mediterranean Sea, J. Geophys. Res. Oceans, 118, doi:10.1002/jgrc.20078.

Volkov, D. L., G. Larnicol, and J. Dorandeu (2007), Improving the quality of satellite altimetry data over continental shelves, J. Geophys. Res., 112, C06020, doi:10.1029/2006JC003765.

Woodworth, P.L., Player, R., 2003. The permanent service for mean sea level: an update to the 21st century. J. Coast. Res. 19 (2), 287–295.

Chapter 4

Response of the North Atlantic wave climate to atmospheric modes of variability

> *—Además, ¿a qué os referís con verdadero y falso?*
> *¿Quién puede saber lo que ocurrió aquí hace mil o dos mil años? ¿Lo sabéis vosotros?*
>
> *— Besides, what do you mean by true and untrue?*
> *Who can be sure what happened here a thousand or two thousand years ago? Can you?*
>
> Michael Ende, *Momo* (1973)

This chapter has been published in:

- Martínez-Asensio, A., Tsimplis, M.N., Marcos, M., Feng, X., Gomis, D., Jordà, G. & Josey, S. (2015). Response of the North Atlantic wave climate to atmospheric modes of variability. International Journal of Climatology (accepted).

Abstract

This study investigates the relationship between the wind wave climate and the main climate modes of atmospheric variability in the North Atlantic Ocean. The modes considered are the North Atlantic Oscillation (NAO), the East Atlantic pattern (EA), the East Atlantic Western Russian pattern (EA/WR) and the Scandinavian pattern (SCAN). The wave data set consists of buoys records, remote sensing altimetry observations and a numerical hindcast providing significant wave height (SWH), mean wave period (MWP) and mean wave direction (MWD) for the period 1989-2009. After evaluating the reliability of the hindcast, we focus on the impact of each mode on seasonal wave parameters and on the relative importance of wind-sea and swell components. Results demonstrate that the NAO and EA patterns are the most relevant, whereas EA/WR and SCAN patterns have a weaker impact on the North Atlantic wave climate variability. During their positive phases both NAO and EA are related to winter SWH at a rate that reaches 1 m per unit index along the Scottish coasts (NAO) and Iberian coasts (EA). In terms of winter MWD the two modes induce a counter-clockwise shift of up to 65º per negative NAO (positive EA) unit over West European coasts. They also increase the winter MWP in the North Sea and in the Bay of Biscay (up to 1s per unit NAO) and along the western coasts of Europe and North Africa (1s per unit EA). The impact of winter EA on all wave parameters is mostly caused through the swell wave component.

4.1 Introduction

Changes in the wave climate, represented by significant wave height, dominant wave direction and wave period, can modify erosion and accretion processes at the shore, cause serious damages to coastal and offshore structures and influence navigation and harbour operations. Changes in the wave climate parameters are related to changes in the wind forcing, either locally orremotely. Due to its large potential impact along the coast, the influence of atmospheric variability on wave climate has been investigated in many different regions worldwide and using quite different methodologies such as visual observations from ships (Gulev and Grigorieva, 2006), wave hindcasts or re-analysis (Kushnir et al., 1997; Cotton et al., 1999; Bauer, 2001; Tsimplis et al., 2005; Dodet et al., 2010; Le Cozannet et al., 2011; Semedo et al., 2011; Charles et al., 2012; Bertin et al., 2013; Shimura et al., 2013), satellite altimetry (Cotton and Challenor, 1999; Woolf et al., 2002; Tsimplis et al., 2005; Izaguirre et al., 2011), in situ observations from wave buoys (Dupuis et al., 2006) and ocean weather stations (Feng et al., 2014a, 2014b). At climate scales, the understanding of the links between the large-scale atmospheric variability and the regional wave climate is indeed a necessary step to describe the processes that have an impact on the wave parameters.

The North Atlantic Ocean is one of the regions that have been extensively investigated due to the relatively large amount of available observations, its importance for navigation and the fact that changes in the Atlantic wave climate affect the highly populated and developed coastal regions of both North-eastern America and Western Europe. In one of the first works, Bacon and Carter (1993) identified a positive correlation between the north-south gradient of sea level atmospheric pressure and the annual averaged wave height at particular sites of the North Atlantic. Likewise, the significant increase in the wave heights recorded between the 1960s and the early 1990s in the North Atlantic has received much attention due to its associated risks for the marine and coastal environment (Carter and Draper, 1998; Woolf et al., 2001; Gulev and Grigorieva, 2006; Semedo et al, 2011). After the 1990s, trends in North Atlantic mean wave height are no longer clear (Young et al, 2011), although an increase in the extreme regime has been reported for the period 1985-2008.

The main mode of atmospheric variability over the North Atlantic is the North Atlantic Oscillation (NAO, see e.g. Rogers et al., 1990) and it has already been reported to have a strong influence on storm tracking and wave climate, especially during the winter season (Woolf et al., 2002; Bertin et al., 2013). The NAO consists of an oscillating pattern with a positive phase characterized by a stronger and northward displaced latitudinal pressure gradient and a negative phase characterized by a weaker and south-westward displaced pressure gradient. Woolf et al. (2002) found evidence that, over the eastern North Atlantic, the inter-annual variability of significant wave height (SWH) during the period 1985-1997 was influenced by the NAO and probably by the East Atlantic pattern (EA), especially along the continental shelves of Western Europe (up to 0.3-0.4m/unit of winter NAO index). The EA pattern is the second mode in atmospheric variability over the North Atlantic (Rogers et al., 1990). Its positive phase is associated with a strong latitudinal pressure gradient located at about 36-48ºN, a region where there is no impact of the NAO in any of its phases.

The influence of climate modes on the mean wave direction (MWD) and mean wave period (MWP) has received less attention so far. The influence of the NAO on MWD (rotation of 20 degrees clockwise/ unit of winter NAO index) has been demonstrated around southern England on the basis of a wave model (Tsimplis et al., 2005). The influence of the NAO on MWP was established in the Bay of Biscay using a 20-year wave buoy record (Dupuis et al., 2006).

Subsequent studies covering the same areas have confirmed the previous results: Dodet et al. (2010) showed that the winter NAO significantly contributes to the inter-annual variability of SWH, MWD and MWP over the Northeast Atlantic on the basis of a wave hindcast of the last five decades; Charles et al. (2012) have shown that inter-annual variability of SWH, MWD and MWP is also related to the EA patterns; and Le Cozannet et al. (2011) have shown that the occurrence of different sea states during winter is related to the NAO, the EA and also to the East Atlantic-Western Russian pattern (EA/WR). Izaguirre et al. (2011) used altimetry to link extreme events of SWH with the Arctic Oscillation (AO), NAO, EA, EA/WR and Scandinavian pattern (SCAN) indices over the North Atlantic during 1992-2010. More recently, Shimura et al. (2013) have established the relationship between winter SWH and the first nine modes of atmospheric variability in the Northern Hemisphere and the El Niño 3.4 index using a hindcast covering 1960-1990. Bertin et al. (2013) have established the relationship between the NAO and the annual mean of SWH during the whole 20th century using a hindcast of the North Atlantic.

Our study focuses on the relationships between the large scale atmospheric patterns with major influence over the North Atlantic (NAO, EA, EA/WR and SCAN) and wave climate parameters (SWH, MWD and MWP) during the last two decades (1989-2009). In particular, we aim at establishing the relationships for both the swell and wind-sea components, as well as for total wave height. The earlier studies mentioned above have partly addressed these issues; however, no one has so far provided a complete picture including the four major climate indices, the three wave parameters and the separation between wind-sea and swell components over the entire North Atlantic and for the four seasons separately.

The paper is organized as follows: Section 2 introduces the data sets used to represent the wave climate, to obtain the climate indices and to evaluate the wave hindcast. Section 3 is dedicated to the methodology and Section 4 to the hindcast evaluation. Results are presented in Section 5 and discussed in Section 6. Conclusions are outlined in Section 7.

4.2 Data sets

4.2.1 Wind-wave hindcast

Wave fields over the North Atlantic region were simulated with the state of the art WAM model (WAMDI, 1988), a third generation wave model that explicitly solves the wave transport equation. The three source terms (wind input, non-linear transfer, and white capping dissipation) which are prescribed explicitly, are integrated by means of an implicit secondorder, centered difference scheme. For the propagation term, a first order upwind scheme is applied. For further details of the model, readers are referred to works of the WAMDI (1988) and Günther et al. (1992). The model domain and the varying spatial resolution employed to generate the wind-wave hindcast are mapped in Figure 4.1. This is the configuration routinely used by the Spanish Port Authority for operational purposes; the model implements different nested grids, with spatial resolution ranging from 2.5 km to 50 km, linked through a two-way nesting scheme. The highest resolution has been set along the Spanish coasts because the wind-wave hindcast is part of a set of numerical simulations developed in the framework of a project aimed at investigating changes in marine variables along the Spanish coasts (ESCENARIOS project).

Table 4.1. Buoy stations with location, water depth, period of operation and percentage of gaps in the SWH, MWD and MWP records. The wave direction was not available for stations 12-14. The location and distance to the closest model grid point are also listed.

Buoys								Closest grid point	
N	Station	Location (º)	Depth (m)	Period	SWH Gaps (%)	MWD Gaps (%)	MWP Gaps (%)	Location (º)	Distance (km)
1	Bilbao Vizcaya	43.64 N 03.05 W	600	Nov-90 / Jul-12	28.21	34.17	28.11	43.75 N 03.00 W	12.89
2	Cabo de Peñas	43.74 N 06.17 W	615	Jun-97 / Jul-12	20.83	21.35	20.79	43.75 N 06.25 W	6.52
3	Cabo Silleiro	42.12 N 09.43 W	600	Jul-98 / Jul-12	13.62	46.73	13.62	42.00 N 09.50 W	14.55
4	Estaca de Bares	44.12 N 07.67 W	1800	Jul-96 / Jul-12	25.98	29.1	25.98	44.00 N 07.75 W	14.81
5	Golfo de Cádiz	36.48 N 06.96 W	450	Aug-96 / Jun-12	13.48	57.04	12.62	36.50 N 07.00 W	4.21
6	Mar de Alborán	36.27 N 05.03 W	585	Feb-97 / Feb-06	49.13	80.39	28.76	36.25 N 05.00 W	3.49
7	Gran Canaria	28.20 N 15.80 W	780	Jun-97 / Jul-12	13.66	63.43	13.65	28.17 N 15.83 W	4.94
8	Tenerife Sur	27.99 N 16.58 W	710	Apr-98 / Jul-12	17.91	55.13	15.28	28.00 N 16.58 W	1.16
9	Villano Sisargas	43.50 N 09.21 W	386	May-98 / Jul-12	27.14	27.14	27.14	43.50 N 09.25 W	3.22
10	Faro	36.90 N 07.90 W	93	Sep-86 / Jan-96	11.1	13.78	0.04	36.92 N 07.92 W	2.37
11	Sines	37.92 N 08.93 W	97	May-88 / Jan-96	0.18	0.01	0.01	38.00 N 09.00 W	10.81
12	SW Grand Banks	44.30 N 53.60 W	1412-1500	Nov-98 / Mar-12	2.04	100	5.91	44.00 N 54.00 W	46.2
13	Tail of the Bank	43.30 N 51.45 W	70 -1500	Sep-90 / Sep-12	9.08	100	2.62	43.00 N 51.00 W	49.46
14	MEDS016	47.64 N 52.47 W	168	Jun-72 / Feb-97	4.55	100	6.3	48.00 N 53.00 W	58.1

The wave model was forced with 6-hourly surface wind fields obtained from the European Centre for Medium-Range Weather Forecasts (ECMWF) ERA-Interim Re-Analysis (Dee et al. 2011) spanning the period 1989-2009. The spatial resolution of the wind forcing was 0.75x0.75 degrees except in a region covering Southern Europe (marked in Fig. 4.1) where a dynamical downscaling was carried out with the regional atmospheric model RCA3.5 (Samuelsson et al., 2011). In that region the resolution was set to 25 km.

The output of the simulation consisted of 3-hourly SWH, MWP and MWD of total waves as well as of wind-sea and swell components. The separation of the wind-sea and swell components of the wave field is performed as in Hasselmann et al. (1996): the peaks (local maxima) of the directional wave spectrum are identified and attributed either to the sea or to the swell component depending on the period and direction of each peak. When the peak is in the same direction of the wind stress and the period is lower than 10 s, the waves are considered to be part of the wind-sea component; otherwise they are identified as swell. Since this study focuses on climate scales, the output fields were first interpolated onto a regular 1x1 degree grid and they were then monthly averaged.

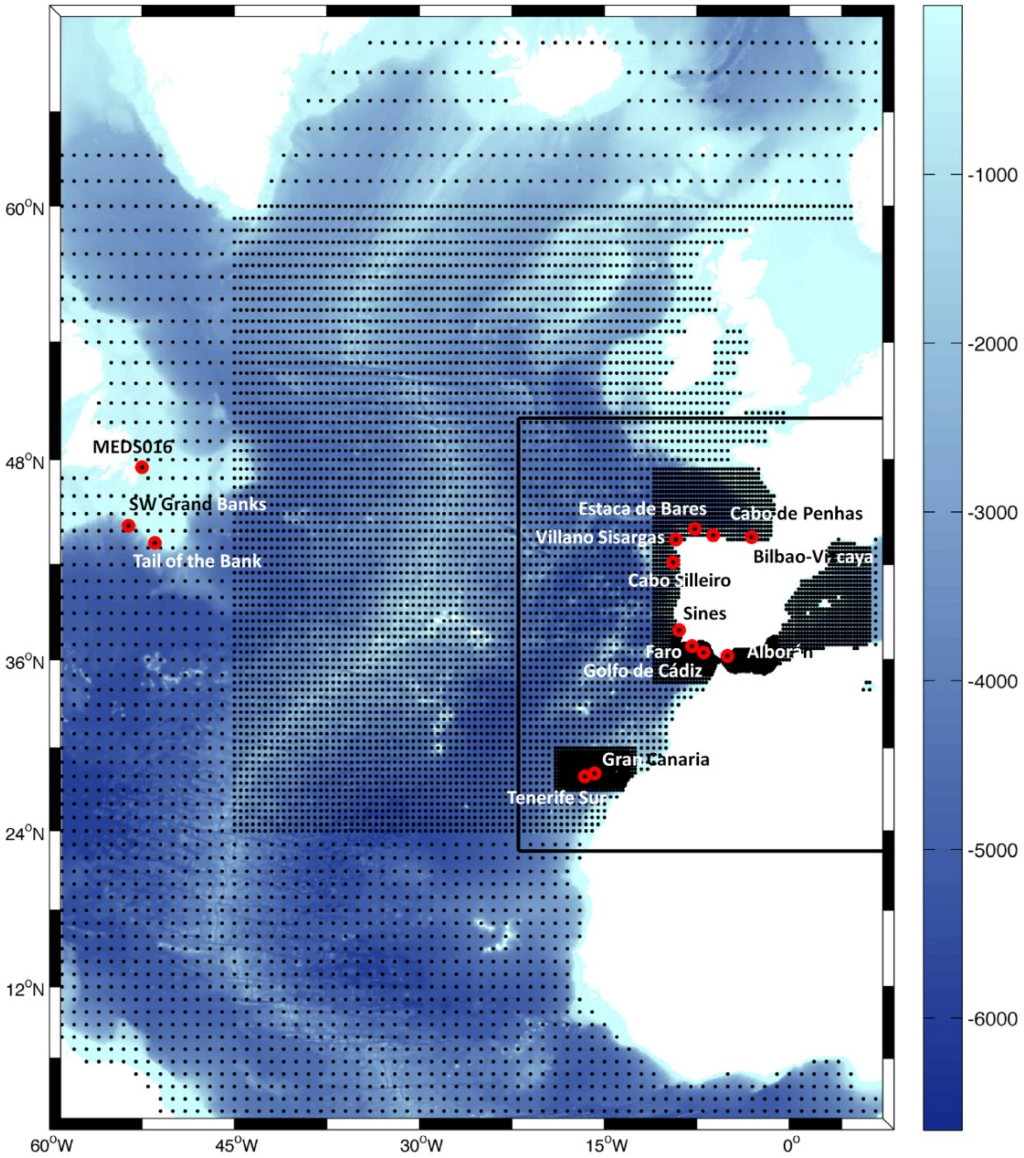

Figure 4.1. Domain of the wind-wave hindcast in the North Atlantic and location of the buoys used for the evaluation (red circles). Grid points of the wind-wave hindcast in the North Atlantic, with the different resolutions used in different regions (black dots). The squared region is the domain where the spatial resolution of the winds around Europe has been increased to 25 km through dynamical downscaling. Bathymetry is also shown (units are meters).

It must be mentioned that a second wind-wave hindcast carried out with the same model configuration but forced with fields from ERA-40 Reanalysis (Uppala et al. 2005) (1958-2002) was also obtained. The longer period covered by ERA-40 could make it more suitable for climate studies; however, the short overlap with observations prevented a proper evaluation of the hindcast. In addition to this, ERA-40 is known to underestimate high wind speeds (Caires and Sterl 2003).

This altogether has prevented an extensive use of the hindcast forced with ERA-40, but it will be used to check the robustness of some of the results obtained with ERA-Interim (see below and Supplementary information).

4.2.2 Wind-wave observations from buoys.

Wave observations from buoys deployed in the North Atlantic were collected from various data providers (Fig. 4.1 and Table 4.1). Data from buoys along the Spanish coasts (station numbers 1-9 in Table 4.1) were provided by the Spanish Port Authority (Puertos del Estado; www.puertos.es). Observations from Portuguese stations (numbers 10-11 in Table 4.1) were obtained from the Instituto Hidrográfico - Portuguese Navy (IH, www.hidrografico.pt/). Finally, stations located along the east coast of Canada (numbers 12-14 in Table 4.1) were obtained from the Integrated Science Data Management (ISDM, www.meds-sdmm.dfo-mpo.gc.ca/isdm-gdsi/waves-vagues/index-eng.htm). The location of buoy stations and the distance to the closest grid point of the wave model are also listed in Table 4.1. All wave observations are freely-available from the operators except those corresponding to stations 10 and 11.

The quality control of buoy observations was as follows. First, all time series were homogenized to a common temporal resolution of 3h and then they were monthly averaged, discarding those months with a percentage of data gaps larger than 30%. In order to identify the influence of the atmospheric forcing modes on the observed wave climate, winter (DJFM) averages were obtained by selecting those winters with at least three (out of four) months of data. The evaluation of the hindcast consisted of comparing observed and modelled monthly wave parameters (from buoys and from the corresponding closest model grid points, respectively) for the overlapping periods.

Note that during their deployment period two of the three Canadian buoys were moved between different locations. The distance of the various deployment sites with respect to their average position ranged between 55 and 91 km for the Tail of the Bank Station (station number 13) and between 46 and 69 km for the SW Grand Banks station (station number 12). These distances are considered small, taking into account that the deployment sites are located well offshore and that monthly time scales are analysed. Correlations between the closest grid point of the hindcast to the average position and the closest grid point to the different deployment sites were calculated, resulting in averaged values of 0.97 for SWH and 0.82 for MWP. Because of the significant correlation and the fact that we use a 1x1 degree grid which, at the latitude of the mean position, corresponds to 111.3 km, a single time series combining all observations was considered for each of these buoys.

4.2.3 Satellite altimetry observations

The along-track high resolution SWH used to validate the wave hindcast were obtained from the Ifremer altimeter Hs database (Queffeulou and Croizé-Fillon, 2010; ftp://ftp.ifremer.fr/ifremer/cersat/products/swath/altimeters/waves), which is regularly updated and calibrated as described in Queffeulou (2004). The altimeter-derived SWH combine measurements from seven altimeters with various spatial and temporal resolutions, namely Jason-1, Jason-2, Topex/Poseidon, ERS-1, ERS-2, Envisat and Geosat Follow-On. The data set used covers the period January 1991 to December 2009. The along–track observations were averaged to a regular 1x1 degree grid covering the model domain. Only grid points with more than 10% of the maximum number of available observations per cell were selected.

4.2.4 Climate indices

Monthly climate indices associated with the leading atmospheric modes in the North Atlantic (NAO, EA, EA/WR and SCAN) and spanning the period 1950-2012 were downloaded from the NOAA Climate Prediction Centre (http://www.cpc.ncep.noaa.gov/data/teledoc/telecontents.shtml). The indices are obtained through a rotated principal component analysis (Barnston and Livezey, 1987) of the monthly mean standardized 500-mb height anomalies in the Northern Hemisphere in such a way that the orthogonality (independence) of the modes is ensured at a monthly scale. The Northern Hemisphere Annular Mode (NAM, also known as Arctic Oscillation, AO) is the major mode of atmospheric variability over the entire Northern Hemisphere. However the NAM is highly correlated with the NAO, especially in winter (Thompson and Wallace, 1998). Some researchers have questioned the physical sense of the NAM (Deser et al, 2000) and a debate on whether NAM and NAO can be considered as different expressions of the same physical phenomenon has arisen (Itoh et al., 2007). This close relationship between both modes (monthly correlation of 0.63) led to the exclusion of the NAM mode for the present study.

4.2.5 Atmospheric variables

Mean sea level atmospheric pressure (MSLP) and 10m wind speed (U10) were obtained from the NCEP/NCAR atmospheric reanalysis (NCEP) (Kistler et al., 2001). Monthly fields with a spatial resolution of 2.5x2.5 degrees over the period 1989-2009 were used to characterize the atmospheric circulation in the different phases of the indices. This atmospheric re-analysis was preferred instead of ERA-Interim because it is the one used to compute the climate indices by the NOAA CPC. Nevertheless, this choice is not critical, as both atmospheric re-analyses are in a very good agreement: the correlation is higher than 0.85 over 80% of the domain for monthly U10 values, while it is higher than 0.85 over 99% of the domain for monthly MSLP values.

4.3 Methodology

Winter averages of buoy records, grid point wave model parameters, climate indices and grid point of MSLP and U10 were computed by averaging the monthly values from December to March (DJFM). We used extended winters (four months) because this is the period when the NAO has the strongest signature (Hurrell et al., 2003). We also used an extended summer average, from June to September (JJAS), for coherence. Averaged directions were calculated by treating each directional observation as a unit vector. First, zonal and meridional components of the unit vectors were obtained by calculating both sine and cosine components of each observational direction. Second, averaged sine and cosine were obtained and then divided to calculate the tangent. Finally, the mean direction was given by the quadrant-specific inverse of the tangent. It is worth mentioning that although climate indices are uncorrelated at a monthly scale, they are not necessarily at seasonal scale. In particular, winter averaged NAO and SCAN indices are significantly anti-correlated (-0.36). Seasonal averaged anomalies were also computed for modelled and observed wave parameters. They were obtained first removing the climatological monthly mean from the monthly values and then computing the seasonal average.

The relationship between wave parameters and climate indices was studied using correlations and linear regressions between seasonal anomalies of wave parameters and seasonal averaged climate indices which approximately vary from -2 to 2. All seasonal averaged time series were detrended for the common period before any correlation and regression coefficient was estimated. The level of significance used for the correlation and regression coefficients was always 95%. For completeness, a linear regression model including the four seasonal climate indices was carried out at each grid point in order to fit the seasonal wave parameters. To do that, a forward/backward stepwise regression was applied at each grid point in order to determine the number of climate indices to be included (Draper and Smith, 1998) and their corresponding coefficients.

Composite fields of wave anomaly parameters, MSLP and U10 were used to obtain the spatial patterns that represent the atmospheric forcing associated with high and low values of each index. The composite fields were obtained by first selecting the monthly fields of wave anomaly parameters, MSLP and U10 (from the corresponding season) coinciding with an index value higher than 1.5 (or lower than -1.5). Next, a weighted mean was calculated multiplying each selected field by the corresponding monthly value of the index. The spatial pattern

Table 4.2. Monthly correlation, RMS differences and bias between hindcasted and observed SWH, DIR and MWP during the overlapping period. Winter correlation (in brackets). Monthly mean and standard deviations of observed SWH, DIR and MWP are also shown. Positive mean DIR values indicate clockwise direction from north and negative values indicate a counter-clockwise direction.

	SWH				MWD				MWP			
Station	Corr.	RMSD (m)	Bias (m)	Mean/ St. Dev.(m)	Corr.	RMSD (º)	Bias (º)	Mean/ St. Dev.(º)	Corr.	RMSD (s)	Bias (s)	Mean/ St. Dev.(s)
Bilbao Vizcaya	0.98 (0.91)	0.3	-0.24	1.93 ± 0.67	0.85 (0.95)	5.07	0.26	132.87 ± 9.22	0.94 (0.97)	0.47	0.26	6.23 ± 0.96
Cabo de Peñas	0.98 (0.57)	0.25	-0.19	1.96 ± 0.63	0.86 (0.96)	6.91	-0.11	147.82 ± 10.68	0.85 (0.63)	0.62	0.31	6.23 ± 0.99
Cabo Silleiro	0.98 (0.97)	0.29	-0.22	2.29 ± 0.71	0.93 (0.73)	7.16	1.2	131.16 ± 13.72	0.96 (0.98)	0.27	0.05	6.32 ± 0.84
Estaca de Bares	0.99 (0.77)	0.4	-0.35	2.44 ± 0.77	0.95 (0.99)	7.03	0.62	140.30 ± 20.86	0.95 (0.95)	0.31	0.16	6.22 ± 0.83
Golfo de Cádiz	0.96 (0.99)	0.12	-0.06	1.19 ± 0.36	0.78 (-)	24.78	0.06	74.38 ± 39.36	0.94 (0.90)	0.37	0.22	4.54 ± 0.68
Mar de Alborán	0.83 (-)	0.15	-0.09	0.71 ± 0.18	0.87 (-)	20.82	-9.92	-26.68 ± 25.11	0.28 (-)	0.43	0.13	3.74 ± 0.30
Gran Canaria	0.89 (0.97)	0.38	-0.37	1.62 ± 0.23	0.94 (-)	4	-0.11	-165.80 ± 11.46	0.60 (0.38)	0.79	-0.56	5.56 ± 0.63
Tenerife Sur	0.63 (0.78)	0.43	-0.41	0.92 ± 0.17	0.61 (-)	18.25	-0.39	-69.07 ± 21.22	0.41 (0.22)	0.51	-0.45	4.14 ± 0.23
Villano Sisargas	0.99 (0.98)	0.38	-0.33	2.42 ± 0.73	0.92 (0.95)	9.21	4.14	143.95 ± 19.82	0.95 (0.91)	0.29	0.12	6.13 ± 0.79
Faro	0.97 (-)	0.12	-0.09	0.96 ± 0.33	0.75 (-)	18.37	-1.92	46.28 ± 23.81	0.94 (-)	0.36	-0.11	4.69 ± 0.62
Sines	0.98 (-)	0.21	-0.14	1.72 ± 0.60	0.88 (-)	6.95	-0.02	120.87 ± 6.35	0.97 (-)	0.52	-0.41	6.69 ± 1.20
SW Grand Banks	0.83 (-)	0.75	0.48	2.51 ± 0.86	-	-	-	-	0.73 (-)	3.13	-3.06	9.79 ± 0.81
Tail of the Bank	0.96 (0.78)	0.63	-0.55	2.57 ± 0.83	-	-	-	-	0.81 (0.65)	4.62	-4.58	10.15 ± 0.99
MEDS016	0.91 (-)	0.33	0.05	2.17 ± 0.60	-	-	-	-	0.87 (-)	4.2	-4.15	10.13 ± 1.25
MEAN	0.92 (0.86)	0.38	-0.29	1.81 ± 0.58	0.84 (0.92)	16.71	-0.04	61.46 ± 21.62	0.80 (0.73)	1.32	-0.94	6.47 ± 0.86

obtained in this way can be considered as the one associated with a unit positive (or negative) value of the climate index. The use of other thresholds different from ±1.5 did not significantly alter the results.

4.4 Evaluation of the wind-wave hindcast

The wave hindcast was explored and compared with buoy and altimetry observations in order to ensure its reliability prior to the investigation of the relationships with large scale climate modes. The correlation coefficient at 95% level of significance, the root mean squared difference (RMSD) and the bias between observed and modelled monthly wave parameters were calculated for each buoy and for each altimetry grid point for their respective overlapping periods. Results, listed in Table 4.2, revealed significant correlations for SWH (from 0.63 to 0.99) and MWP (from 0.61 to 0.95) for all buoys. Lower but still significant correlations were found for MWD (from 0.28 to 0.96). RMSD displays a larger spread of values among sites. Higher RMSD values were found where standard deviation is higher. The highest values correspond to Canadian stations, especially for MWP (from 0.27 to 4.62 s).

It is worth noting that a considerable part of the RMSD between modelled and observed SWH (0.38m on average) and MWP (1.32s) is accounted for by the bias (-0.29m and -0.94s, respectively). For MWD the contribution of the bias (-0.04º) to the RMS differences (16.71º) is much lower (Table 4.2). The negative SWH bias found at all sites points to an overall underestimation of the observed SWH by the model.

When altimetry observations were used, high correlations between modelled and observed SWH were found over all the domain (0.79 on average) except in the Gulf of Guinea, where lower but still significant values were found (see Supplementary information, Fig. 4.S1). The lower quality in that region is probably induced by the lack of appropriate lateral boundary conditions at the southern boundary. The RMSD (is 0.55 m when averaged over the whole domain, ranging from 0.1 to 1.3 m at individual grid points; the averaged bias is -0.43 m, ranging from -1.2 to 0.2 m at particular grid points. Highest RMSD and most negative SWH bias were found at the northern sector of the North Atlantic, where the variability of SWH is higher, in agreement with the results derived from the buoys.

The spatial patterns of the climatological fields of wave parameters were also explored and compared with earlier works. Climatological winter means and standard deviations (std) of SWH, MWP, MWD, U10 and wind direction are shown in Fig. 4.2. The winter wave climate (Figs. 4.2a,b) shows a northern sector influenced by the westerly winds and characterized by high (up to 4.0 m), long-period (up to 7.9 s) waves that turn to be more north-easterly above 60ºN (Fig. 4.2h,g), coinciding with the winter averaged wind speed (Fig. 4.2c). These patterns and values are comparable to those shown by Dodet et al. (2010) by forcing the wave model WAVEWATCH (Tolman, 2009) with wind fields from the NCEP/NCAR Reanalysis (Kalnay et al., 1996) and Semedo et al. (2011) by using wave fields from ERA-40. The southern sector is dominated by the trade winds and shows lower SWH (up to 2.4 m), slightly shorter periods (up to 7.4 s) and southerly waves, also in agreement with earlier works (Dodet et al., 2010; Semedo et al., 2011). The northern sector is also where the standard deviations of SWH and wind speed are higher during the winter season (Figs. 4.2d,f). The maximum winter inter-annual variability of SWH is found to the northwest of the British Isles, with std values of up to 0.8 m (Fig. 4.2d). Overall, the MWP std is larger in the eastern sector of the North Atlantic, especially in the Bay of Biscay, Strait of Gibraltar, Canary Islands and in the latitudinal band 0ºN-12ºW, showing values of up to 1.1 s (Fig. 4.2e). The inter-anual variability of winter MWD is larger over the north-western sector of the Atlantic, where std approaches 90º (Fig. 4.2g). The variability of MWD does not necessarily correspond to changes in the direction of collocated winds (Fig. 4.2h), because MWD reflects the effect of both

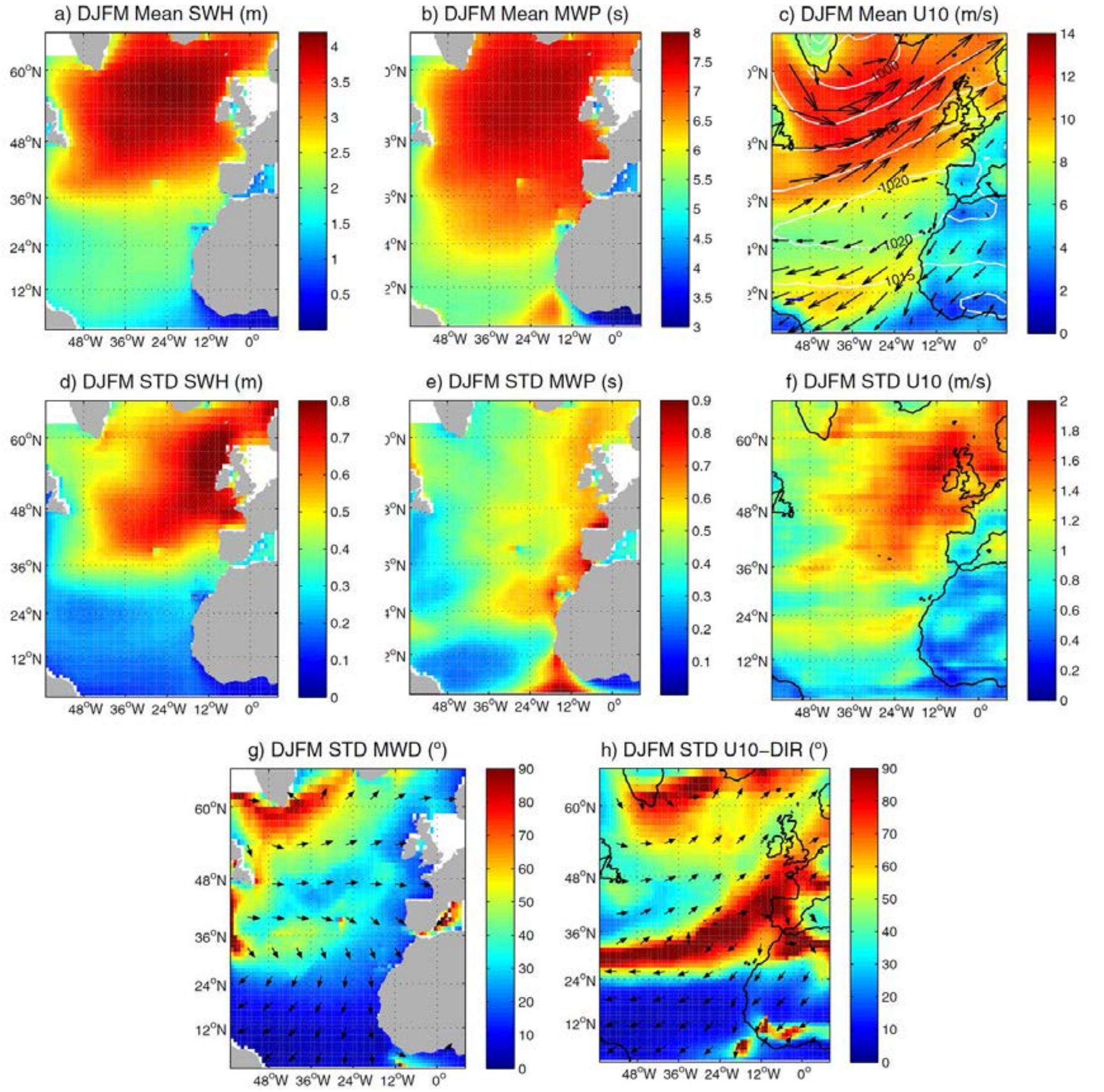

Figure 4.2. Winter averages of SWH (a), MWP (b) and U10 (c) (coloured areas denote the averaged U10 speed) and white lines denote winter averaged SLP. Winter standard deviation of deseasonalized SWH (d), MWP (e) and U10 (f) (coloured areas denote the standard deviation of U10 speed). Winter averaged MWD (arrows) and standard deviation of deseasonalized winter MWD (coloured areas) (g). Standard deviation of deseasonalized winter wind direction (coloured areas) (h).

local and remote wind forcing.

Overall, the performance of the wind-wave hindcast during the winter season shows a good agreement with observations for all wave parameters, particularly for SWH. Likewise, the climatological patterns are consistent with earlier results. Moreover, it is worth noting that model biases do not affect the conclusions of this study as we mainly work with correlations, which are independent of biases.

During the summer season (JJAS), spatial patterns of wave climate are similar to those obtained for winter but with larger SWH values in the region affected by the trade winds and lower SWH values in the region affected by the westerlies (not shown). Overall, the mean values of SWH (1.4 m) and MWP (5.1 s) are lower than in the rest of the seasons.

4.5 Impact of atmospheric climate modes on seasonal wave climate

4.5.1 Relation between atmospheric climate indices and seasonal wave climate

With the aim of establishing how the large-scale atmospheric climate modes influence wave fields, correlations and regression coefficients between seasonally averaged wave anomaly parameters and climate indices were computed.

Regression coefficients of winter SWH, MWP and MWD with the climate indices are mapped in Fig. 4.3. Dots correspond to grid points that are significantly correlated. The NAO and EA are the patterns with the largest influence on North Atlantic winter wave climate, both having an impact over most of the region. The regression patterns between the NAO and both SWH and MWP are very similar: positive values (of up to 0.9m and 0.8s per unit NAO) were found over the north-eastern sector, while negative values (of up to -0.5 m and -0.7 s per unit NAO) were found over the western and southern sectors. For the MWD, positive values (up to 65º per unit NAO) were found over the southern sector and negative values (up to -69º per unit NAO) were found over the northern sector except at the highest latitudes (above 60ºN), where values turn to be positive (up to 88º per unit index). The regression coefficients between EA and both SWH and MWP show a similar pattern, with positive significant values (up 0.4 m and 0.5 s per unit EA, respectively) over mid-latitudes. For MWD the correlation is negative over most of the domain, with some positive areas in the north-western sector. Significant values between EA/WR and SWH were found only at lower latitudes, reaching values of up to -0.3 m per unit EA/WR along the coasts of the Iberian Peninsula and Northwest Africa. Finally, SCAN has some influence on SWH and MWP only over the north-easternmost part of the domain (up to -0.8 m and -0.6 s per unit SCAN, respectively) and in some areas along the north-western coasts of Africa (up to 0.3 m and 0.5 s per unit SCAN). In order to check the influence of the limited length of the hindcast in these results, the same computations were carried out using the 1958-2002 hindcast

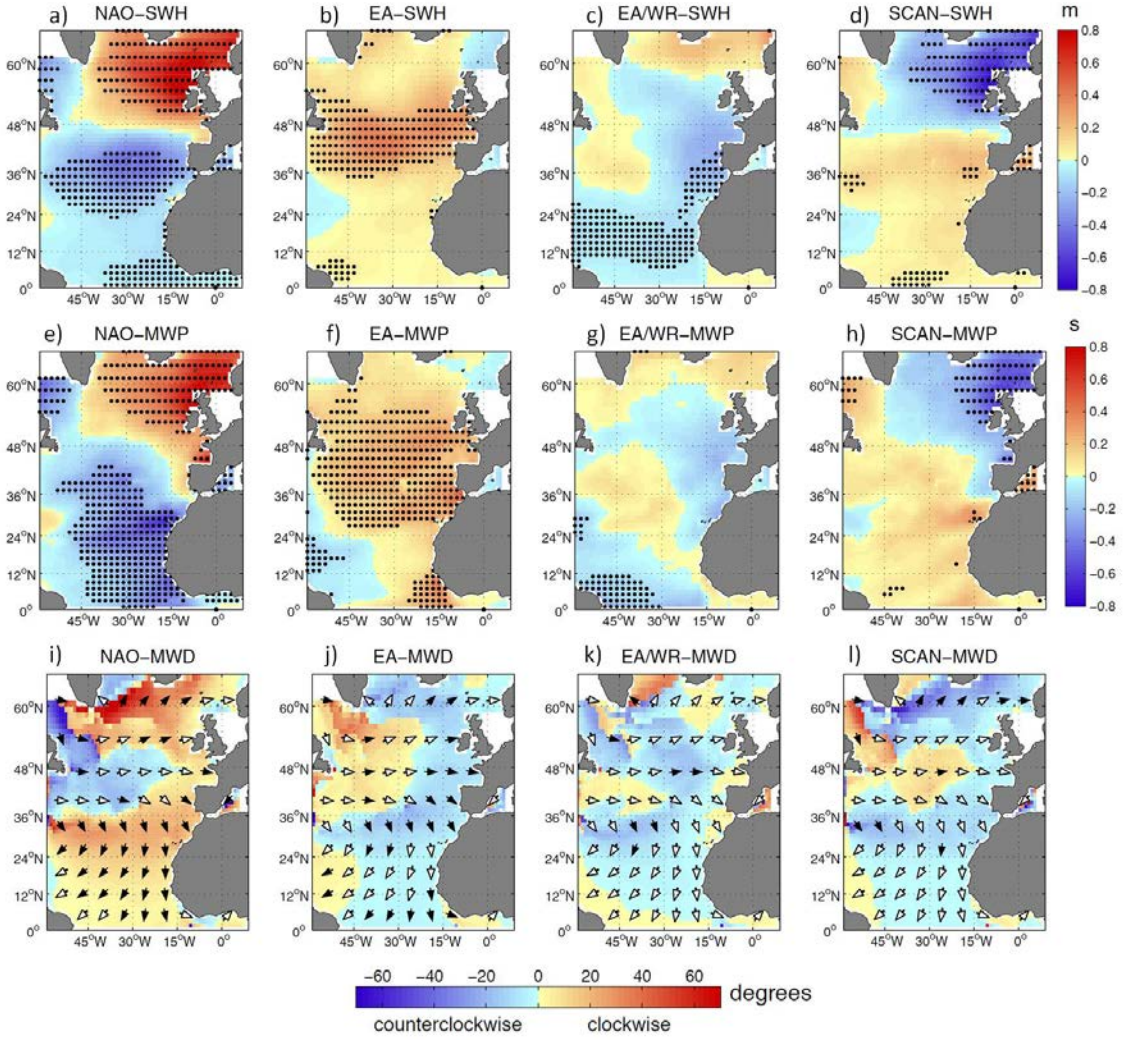

Figure 4.3. Winter (DJFM) regression coefficient between climate indices and hindcasted SWH, MWP and MWD anomalies for the period 1989-2009. Black dots and black arrows denote a minimum 95% level of significance. Arrows indicate winter averaged MWD and coloured areas denote the change in direction from the winter averaged value in both clockwise (red) and counter-clockwise sense (blue). Units are m per unit index, s per unit index and degrees per unit index.

forced with ERA40. The results obtained were very similar in terms of magnitude and patterns (Fig. 4.S2), thus suggesting that the regressions mapped in Fig. 4.3 are robust.

Similarly to the results presented for winter, the relationships were also explored for the summer (JJAS) season for completeness (Fig. 4.S3). Although the wave parameters show some sensitivity to climate indices, this is statistically significant only over small areas and in any case it is much lower than during the winter season: by a factor 1/4 in the case of SWH and MWP and by a factor 1/2 for MWD. This is a direct consequence of the lower summer wave climate variability, whereas indices variability remains nearly unchanged. For this reason, the summer season will not be discussed. The relationships for spring and autumn were also explored for completeness, finding intermediate characteristics between those found for winter and summer. (see Figs. 4.S4 and 4.S5 in Supplementary information).

An important feature to be commented is that the sensitivity of the wave climate to different phases of climate indices is asymmetric in terms of magnitude. This is reflected in the composite Figures 4.4-4.6 for winter SWH, MWP and MWD, respectively. The impact of the indices on winter SWH is shown in Fig. 4.4. During its positive phase, winter NAO induces higher than average SWH over the northeast Atlantic, with maximum values near the Scottish coasts of up to 1.0 m per positive unit NAO (Fig. 4.4a). Conversely, between 30-40ºN SWH are smaller than average during positive NAO phases. The pattern is almost the opposite during the negative phase, with increasing SWH (up to 0.6 m per negative unit NAO) between 30-40ºN and decreasing SWH at higher latitudes, mainly to the northeast (Fig. 4.4b). The positive phase of EA induces higher than average SWH between latitudes 36ºN and 48ºN, mostly affecting the Iberian Peninsula, France and the south of the British Isles (values of up to 0.9 m per positive unit EA, see Fig. 4.4c). Conversely, the impact of the negative phase of EA on SWH is smaller (Fig. 4.4d). SWH decreases (of up to 0.9m per positive unit EA/WR) are induced during the positive phase of EA/WR along the western European coasts (Fig. 4.4e) while SWH increases (of up to 0.4m per negative unit EA/WR) over are induced during its negative phase at higher latitudes. During its winter positive phase, SCAN induces positive SWH anomalies (up to 0.5 m per positive unit SCAN) at the coasts of the Iberian Peninsula and Canary Islands and negative anomalies in the Northern sector of the domain (Fig. 4.4g). During its negative phase SCAN induces positive anomalies over most of the domain, with maximum values (0.9 m per negative unit SCAN) to the west of the British Isles and in the Gulf of Biscay (Fig. 4.4h).

The impacts of NAO and EA on MWP (Fig. 4.5) have spatial patterns similar to those of SWH. Winter NAO induces maximum departures from the mean MWP (up to 1.7s per positive unit NAO) to the west of the British Isles and in the Bay of Biscay (Figs. 4.5a,b). For negative phases the largest increase is obtained at lower latitudes, especially around the Canary Islands (up to 0.8 s per negative unit NAO). Major changes associated with a positive EA phase are found between latitudes 24ºN and 36ºN (Fig. 4.5c) with up to 1.1 s per positive unit EA. Winter EA/WR induces negative MWP anomalies (up to -0.8m per negative unit EA/WR) over Western European coasts. During its winter positive

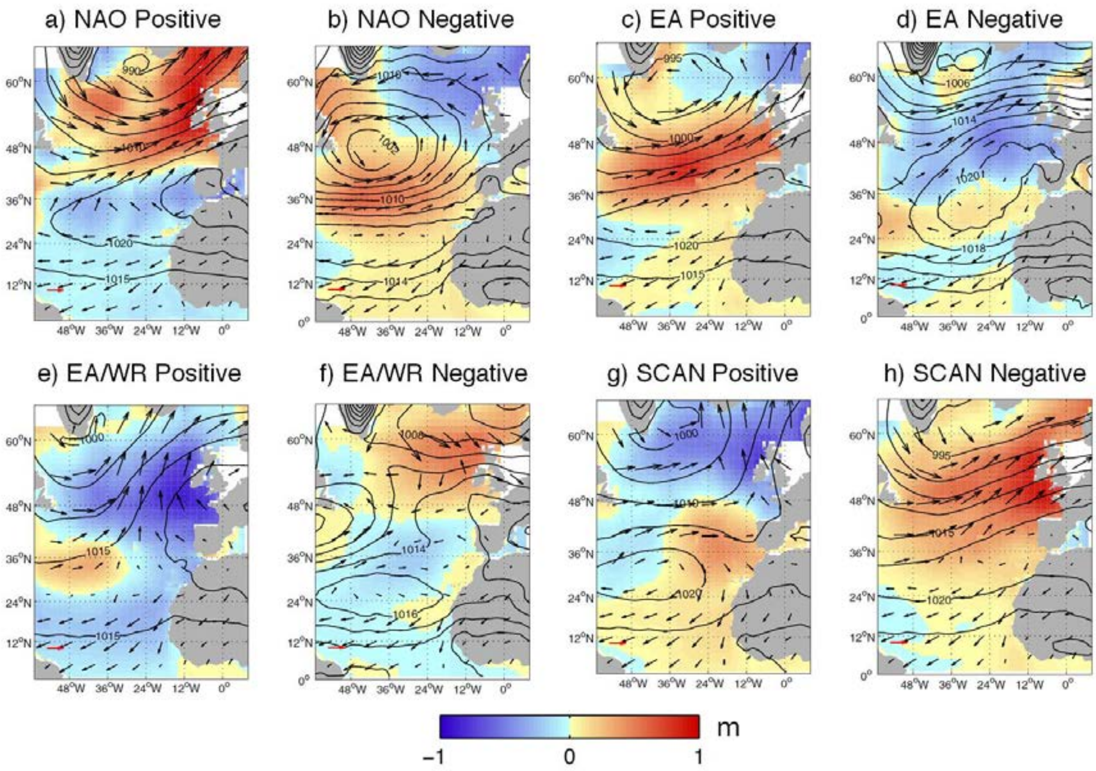
a) NAO Positive
b) NAO Negative
c) EA Positive
d) EA Negative
e) EA/WR Positive
f) EA/WR Negative
g) SCAN Positive
h) SCAN Negative

Figure 4.4. Winter (DJFM) SWH anomalies (m per unit index) and 10m wind speed (vectors) averaged for winter NAO (a,b), EA (c,d), EA/WR (e,f) and SCAN (g,h) indices under a positive state (left) and a negative state (right). Corresponding averaged sea level pressures are contoured (black lines). The horizontal red vector is for scale and indicates a wind speed of 10m/s.

phase, SCAN induces positive MWP (up to 0.6s per positive unit SCAN) at the coasts of the Iberian Peninsula and Canary islands, and negative anomalies in the Northern sector of the domain (Fig. 4.5g). During its negative phase SCAN induces positive MWP anomalies over most of the domain, with maximum values at the European and African coasts (up to 0.8 s per negative unit SCAN).

Finally, the impact on MWD is also explored. Over most of the North Atlantic positive phases of winter NAO induce clockwise rotations with respect to the mean direction over most of the domain but especially at 30º N and 60ºN latitudes (Fig. 4.6a). Conversely, negative NAO phases are related to counter-clockwise anomalies in MWD over most of the North Atlantic (Fig. 4.6b), with values of about 40º (60º) per negative unit NAO around 30ºN (60ºN) (Fig. 4.6b).

The pattern associated with positive phases of EA (Fig. 4.6c) shows that they induce counter-clockwise changes of around 20º per positive unit EA along the European coasts, reaching 60º at 60ºN. Also, clockwise changes of more than 60º

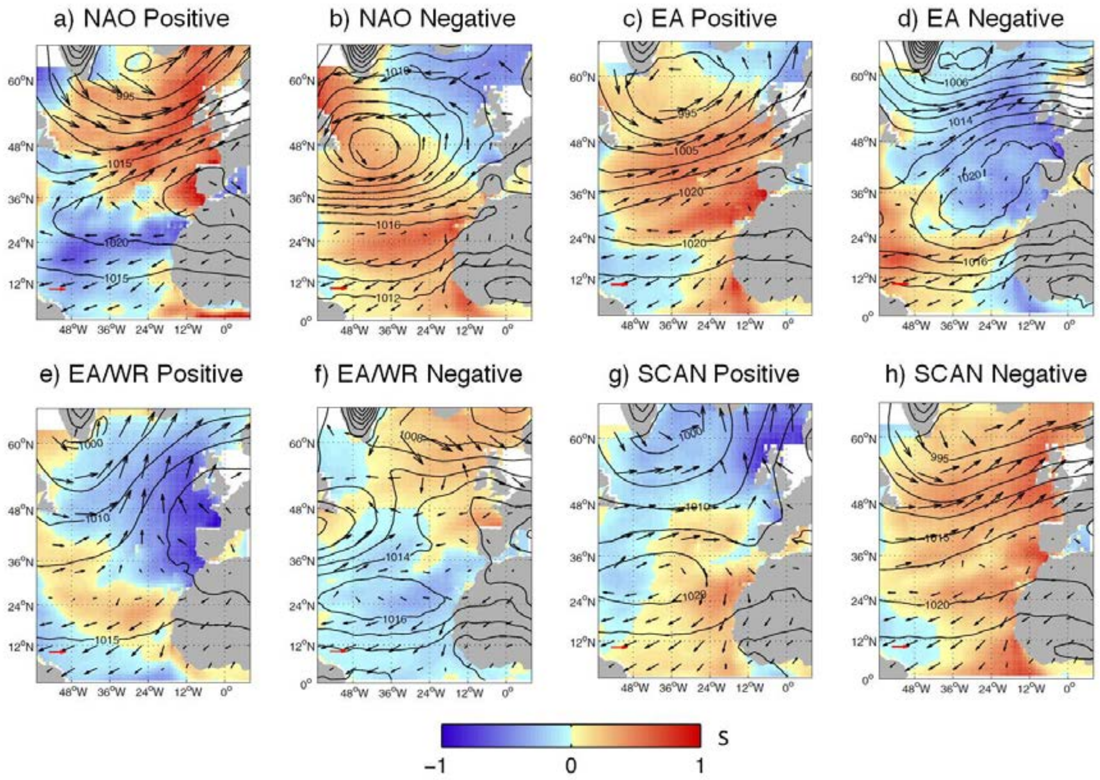

Figure 4.5. The same as at Figure 4, but for MWP anomalies (s per unit index).

per positive unit EA are found in the northwestern North Atlantic. Also negative phase of EA induce significant changes in MWD (Fig. 4.6d), e.g. more than 40º per negative EA unit in the Bay of Biscay. No significant changes in MWD anomalies induced by EA/WR and SCAN are found, except in some areas over open waters.

The values mapped in these Figures must be carefully interpreted, particularly if they are to be compared with simple regressions such as those of Fig. 4.3. A difference, already pointed out in the methodology section, is that the composites are produced selecting the winters with the highest (lowest) indices values (i.e. considering only strong and well defined phases of each index), whereas the regression coefficients were computed considering all winters.

4.5.2 Relation between atmospheric climate patterns and seasonal wave climate

During the winter period, the NAO is the climate mode that has the highest influence on the North Atlantic wave climate. The positive phase of winter NAO is characterized by a northward displacement of the Icelandic Low and a pressure gradient increase between 36°N and 60°N (Fig. 4.4a). This effect results in strong (and long duration) westerly winds and in a consequent increase in the SWH and MWP of the waves, which propagate eastwards towards North-western Europe

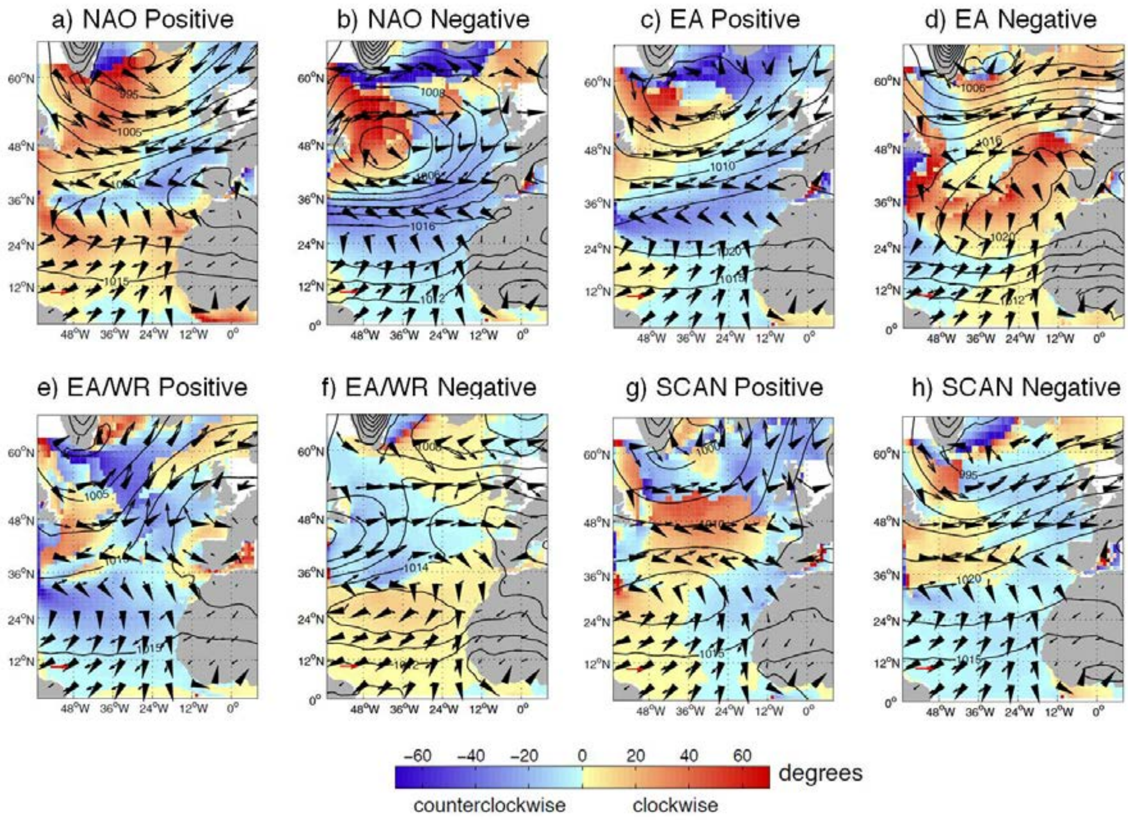

Figure 6. Winter (DJFM) MWD anomalies (º per unit index) (colours), 10m wind speed (vectors) and MWD (black triangles) averaged for winter NAO (a,b), EA (c,d), EA/WR (e,f) and SCAN (g,h) indices under a positive state (left) and a negative state (right). Corresponding averaged sea level pressures are contoured (black lines). The horizontal red vector is for scale and indicates a wind speed of 10m/s.

(Figs. 4.4a, 4.5a and 4.6a). The negative phase of winter NAO is characterized by a south-westward displacement of the meridional pressure gradient, which in this situation is located between 30ºN and 40ºN (Fig. 4.4b). The increase in SWH and MWP observed between these two latitudes during the negative phase derives from the southward displacement of the maximum gradient (Figs. 4.4b, 4.5b, 4.6b), not from their strengthening (the pressure gradient is slightly weaker than during the positive phase). An increase in the MWP is also observed at low latitudes (24ºN), coinciding with the position of the high pressure centre during the negative phase (Fig. 4.4b) and explaining the high inter-annual variability of MWP observed in that region (Fig. 4.2e). One possible explanation for the positive MWP anomalies at the Azores High (between 20ºN and 30ºN) is that in presence of weaker winds the swell waves, coming from the North (between 30ºN and 40ºN), dominate over wind-seas. At high latitudes (above 60ºN) the easterly winds resulting from the southern displacement of the Icelandic Low induce significant changes in MWD; this region is where the highest winter variability of MWD is observed (Fig. 4.2g).

The second mode of atmospheric inter-annual variability over the North Atlantic, the EA pattern, is also related to the displacements of the Icelandic Low and subtropical High. During its winter positive phase the southward displacement of the Icelandic Low makes that the maximum meridional pressure gradient associated with this mode is located between 36ºN and 48ºN, an area where strong westerly winds induce an increase in SWH and MWP (Figs. 4.4c, 4.5c) and waves propagate eastwards towards the coasts of Southern Europe (Fig. 4.6c). This is a similar behaviour to that of the NAO, but the pressure gradient is now located between 36ºN-48ºN, where the NAO does not show any impact in any of its phases (Fig. 4.4a). The pattern of the negative phase of winter EA is significantly different from the former patterns, as the high pressure centre is much wider and the pressure gradient is weaker (Fig. 4.4d). This results in the absence of strong winds and, in turn, in important changes in MWD, especially along the coasts of southern Europe (Fig. 4.6d).

The positive phase of winter EA/WR presents a high pressure centre over the Iberian Peninsula and a low pressure centre to the south of Greenland, which results in a weak NW-SE pressure gradient to the west of the British Islands and hence on waves propagating north-eastwards (Figs. 4.4e, 4.6e). During its negative phase, the pressure gradient is more zonal, resulting in the eastward propagation of waves (Fig. 4.6f). During the positive phase of winter SCAN, the pressure gradient decreases and moves westwards, leading to a slight increase in SWH and MWP over the coasts of the Iberian Peninsula, and to a northwards shift of MWD in the North Sea (Figs. 4.4g, 4.5g, 4.6g). On the contrary, during the negative SCAN phase the pressure gradient moves eastwards and waves propagate westwards in the North Sea (Fig. 4.6h).

4.5.3 Impact of climate modes on wind-sea and swell components

Correlations between climate indices and wave parameters were significant also in areas away from the larger pressure gradients. For instance, the EA is related to SWH, MWD and MWP at low latitudes, whereas the winter NAO is related to MWP and MWD but, surprisingly, not to SWH (except in a small area in the Gulf of Guinea). This behaviour was also noted by Semedo et al. (2011), who showed that the leading mode of variability of SWH corresponding to wind-sea (SWHw) had a NAO-like structure, while the leading modes of SWH corresponding to total-sea (SWH) and swell (SWHs) had not. In order to investigate whether the absence of correlation between the indices and SWH is a

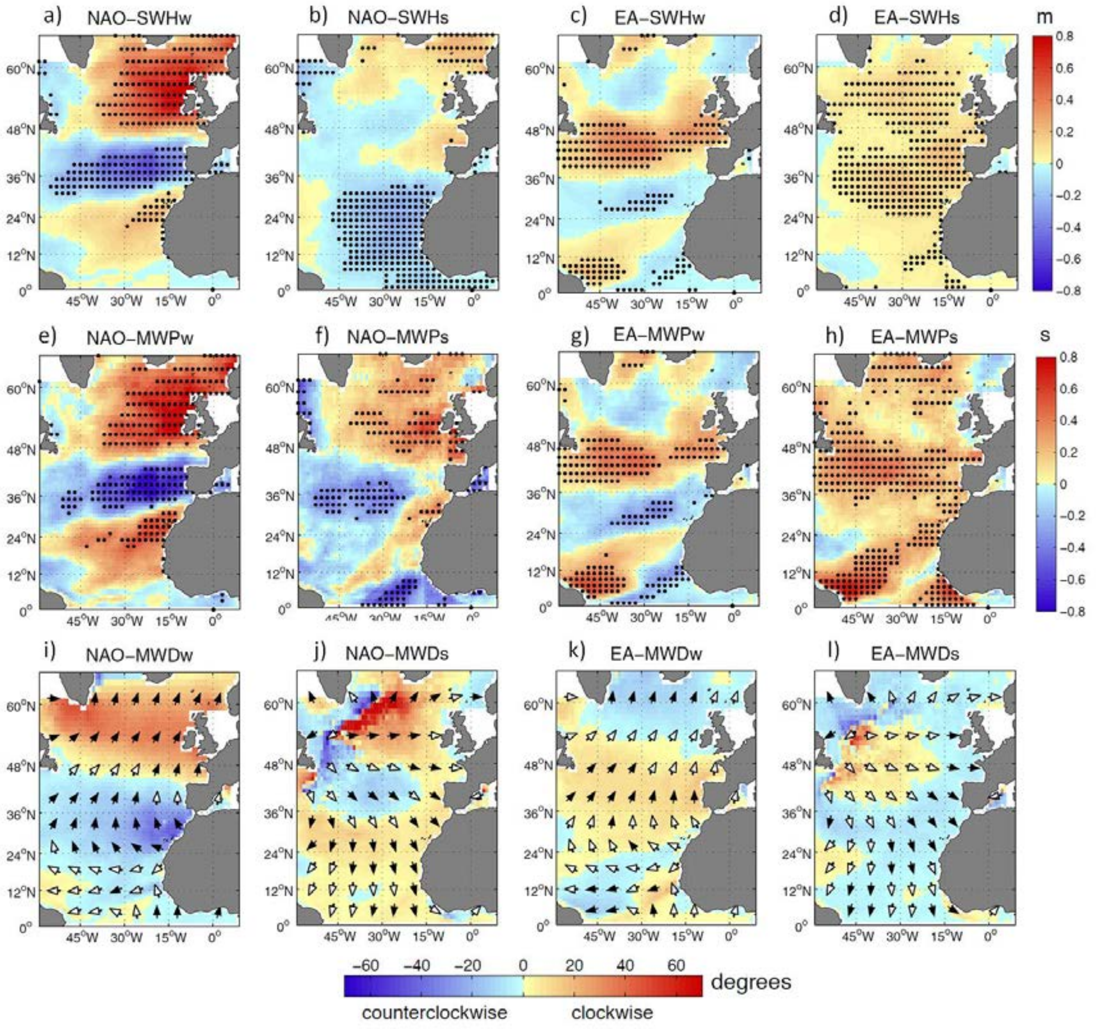

Figure 7. Winter (DJFM) regression coefficient between hindcasted wind-sea and swell parameters and NAO and EA indices for the period 1989-2009 (the regression coefficient for total wave parameters and NAO and EA indices have already been shown in Fig. 3). Black dots and black arrows denote a minimum 95% level of significance. Arrows indicate winter averaged MWD and coloured areas denote the change in direction from the winter averaged value in both clockwise (red) and counter-clockwise sense (blue). Units are m per unit index, s per unit index and degrees per unit index.

consequence of the different behaviour of wind-sea and swell, regression coefficients between winter NAO and EA leading indices and wave parameters were obtained at each grid point for both wind-sea and swell separately (Fig. 4.7), in the same way that it was done before for total SWH. The other two climate indices, EA/WR and SCAN, were not included as their relevance is much smaller.

Above 24ºN, the regression coefficients between winter NAO and SWH, SWHw and SWHs show similar patterns (Figs. 4.3a and 4.7a,b). The lower values obtained for SWHs indicate that the impact of winter NAO on total SWH is mainly through wind-sea and, to a lower extent, through swell. Below 24ºN, however, winter NAO is not related to SWH (see Fig. 4.3a), while it has a significant but opposite impact on SWHw and SWHs related to the Trade winds displacement between NAO phases (Figs. 4.7a,b): while the NAO index is positively correlated with SWHw due to the stronger Trade winds induced during the positive NAO phase, it is negatively correlated with SWHs due to southward propagation of swell waves from higher latitudes (30ºN-40ºN) induced during the negative NAO phase.

The interaction between wave components is even more complex for MWP. The dominant periods are always in between those of wind waves (shorter) and swell (longer). In the north-eastern sector, where both components are important, there is a positive relationship between winter NAO and MWP (Fig. 4.3e) as a result of the positive sensitivity of both MWPs and MWPw to winter NAO (Figs. 4.7e,f). At low latitudes the relation is more cumbersome. During positive phases of the NAO there is swell generated by the Trade winds, while during negative phases there is swell coming from the north and generated by the Westerly winds. This results in the absence of sensitivity of low latitude MWPs to the winter NAO index (see Fig. 4.7f). Conversely, wind waves show a clear sensitivity to winter NAO: they are the dominant component during positive phases of the winter NAO due to the Trade winds (Fig. 4.7e). This makes that the periods observed during positive NAO phases are shorter than those observed during negative phases (when only the swell component coming from the north remains). This results in the negative correlations (positive NAO-shorter periods) observed at low latitudes in Fig. 4.3e).

The impact of NAO on MWD for swell (MWDs) and for total MWD is very similar over most of the domain, indicating that the NAO impact on MWD is mainly through its effect on swell propagation (Figs. 4.7i, j).

When the impact of winter EA on wind-sea and swell parameters was explored, it was found that the spatial structure of swell was very similar (in terms of sign) to that of total waves (Figs. 4.7 c,d,g,h,k,l and Figs. 4.3 b,f,j). This indicates that the impact of EA on North Atlantic waves is mainly through the swell component. It is likely related to the dominance of swell component during the negative phase of the EA, which corresponds to a situation of weakening Westerlies and expansion of the Azores High (thus reduction of SWHw). The values of the regressions though, are smaller.

All the findings discussed so far address the relative importance of the atmospheric climate modes on wave climate variability over the North Atlantic. However, it is worth noting that climate modes account for only a part of this

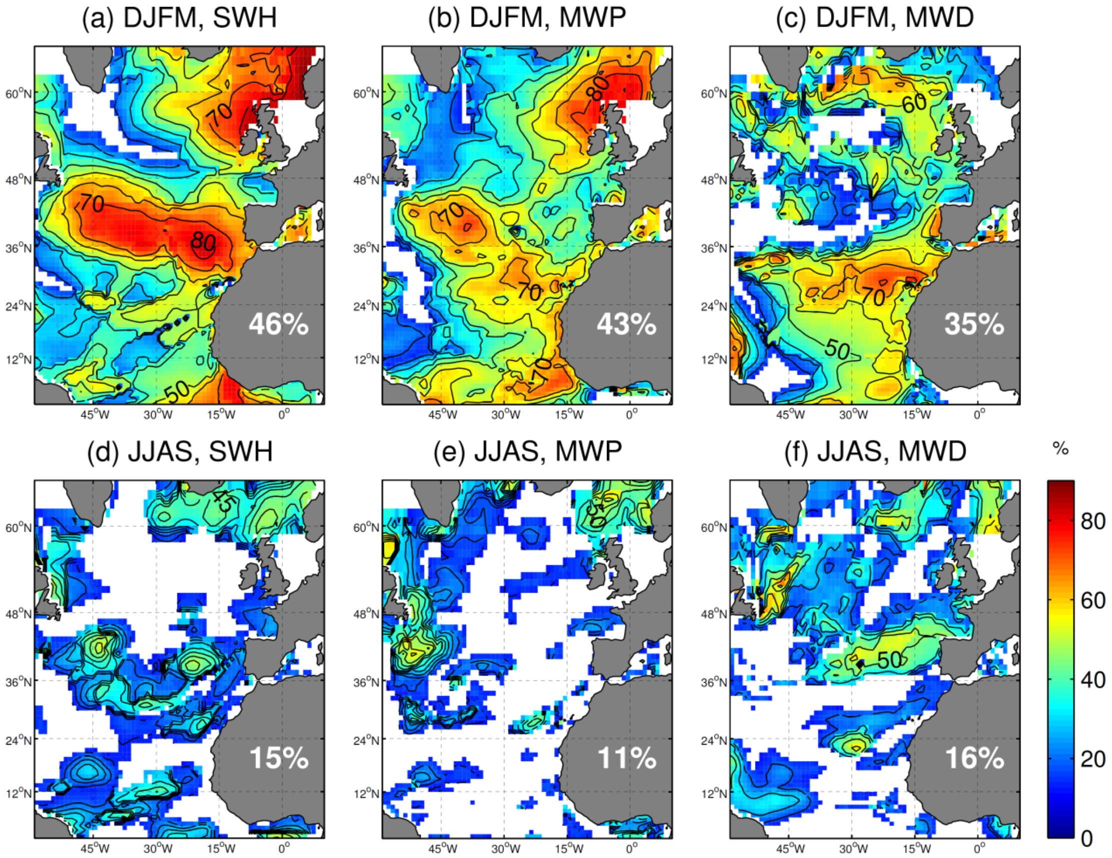

Figure 4.8. Variance accounted for by the regression model in which the four indices (NAO, EA, EA/WR and SCAN) has been regressed against the winter (a, b, c) and summer (d, e, f), SWH (a, d), MWP (b, e) and MWD (c, f) (units in %). Coloured areas denote model statistical significance at 5% level. Averaged values are also shown.

variability. In order to estimate how much of the total variance can be related to large scale climate modes, a multiple regression model has been built in which the four indices (NAO, EA, EA/WR and SCAN) were used as predictors and were regressed against SWH, MWP and MWD. The results, mapped in Fig. 4.8 for the four seasons, show that during the winter season the four climate modes accounted for the highest percentage of variance of SWH (46% on average), MWP (43% on average) and MWD (35% on average) (Figs. 4.8a,b,c). Finally, during summer the variance accounted for the climate modes was much smaller and only significant in some reduced areas (Figs. 4.8d,e,f).

4.6 Summary and Conclusions

In this study we have investigated and quantified the relationships between the wave climate parameters SWH, MWD and MWP and the four major atmospheric climate modes over the North Atlantic using a wind-wave hindcast covering the period 1989-2008. The hindcast has been evaluated against buoy and altimetry observations. The present study completes earlier works that had either focused only on one of the wave parameters (usually SWH) or had investigated only one of the major climate indices (usually the NAO) or have given only a partial view in terms of the covered area and time period.

The overall conclusion of the present work is that the NAO and EA modes have a major impact on North Atlantic SWH during the winter season. When winter NAO is in its positive phase, it induces higher than average SWH in the northern sector of the domain, especially to the northwest of the British Isles (up to 1.0 m per unit positive NAO). Conversely, during its negative phase it produces higher than average SWH in the central North Atlantic (up to 0.6 m per unit negative NAO), nearby Azores and the Iberian Peninsula. The separation between the wind sea and swell components has uncovered that in the southern sector of the North Atlantic (below 24ºN), where the wave climate had been reported to be uncorrelated with winter NAO, there is in fact a significant correlation with each of the components. What happens is that the combination of the positive correlation with the wind-sea component with the negative correlation with the swell component results in a non-statistically significant correlation with total SWH. Regarding the wave direction, winter NAO shifts MWD counter-clockwise over the whole basin, reaching 65º per unit NAO at 60ºN. The MWP is positively correlated with the winter NAO index in the area between the North Sea and the Bay of Biscay (up to 1.7s per unit positive NAO).

Also the EA pattern has a significant influence on North Atlantic wave climate. During positive phases of winter EA, SWH increases between the British Isles and the Iberian Peninsula (up to 0.86 m per unit positive EA), the MWP increases between the western coasts of Europe and North Africa (1.09s per unit positive EA) and MWD rotates counter-clockwise along the European coasts (by up to 60º per unit positive EA). A new result is that the impact of winter EA on all wave parameters is mostly caused through the swell wave component. The winter SCAN and EA/WR indices have a lower impact in terms of both intensity and areas with significant correlation.

These findings extend the results found by Woolf et al. (2002), Tsimplis et al. (2005), Dodet et al. (2010), Charles et al. (2011) and Feng et al. (2014a,b) and confirm the impact of the NAO and EA modes on SWH, MWP and MWD for both wind-sea and swell in the various areas of the North Atlantic. Our results are also in good agreement with Shimura et al. (2013), who showed the correlation patterns over the North Atlantic between winter SWH and the same four climate indices, although for a different period (1960-1990). They are also consistent with those of Charles et al. (2012), who focused on the Bay of Biscay.

The only discrepancy with that work is that we found a significant link between EA and MWD during summer and they did not; the discrepancy is likely related to the use of MWD (in our work) instead of the peak direction used in Charles et al. (2012).

The results presented here can be useful to infer wave changes derived from eventual future changes in the regional modes, under the assumption that the relationships between climate indices and wave parameters will remain stationary in time. Future work should consider a non-stationary approach to identify those changes.

Supporting Information

The following supporting information is available as part of the online article:

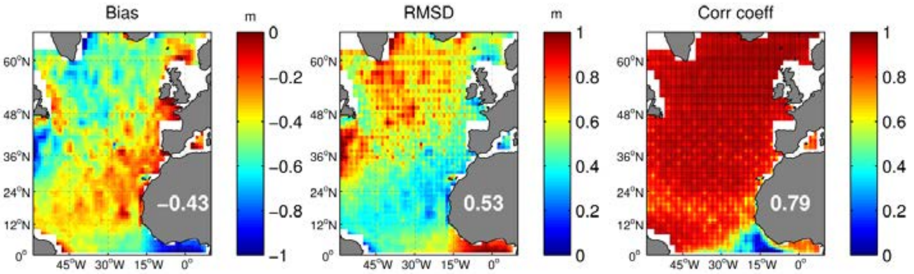

Figure 4.S1. Bias (units in meters) (a), RMSD (units in meters) (b) and correlation coefficient between altimeter and hindcasted monthly SWH during the period 1991-2009. Averaged values are also shown.

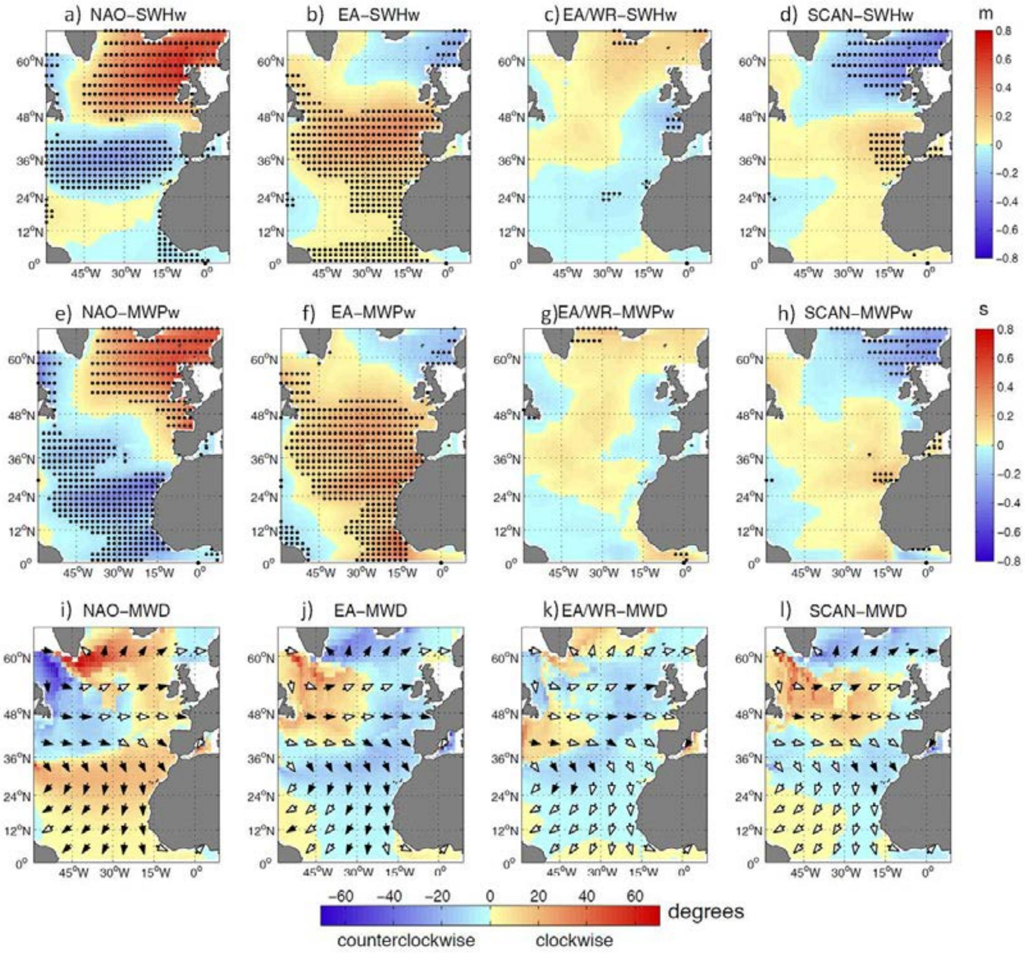

Figure 4.S2. Winter (DJFM) regression coefficient between climate indices and ERA40-hindcasted SWH, MWP and MWD anomalies for the period 1958-2002. Black dots and black arrows denote a minimum 95% level of significance. Arrows indicate winter averaged MWD and coloured areas denote the change in direction from the winter averaged value in both clockwise (red) and counter-clockwise sense (blue). Units are m per unit index, s per unit index and degrees per unit index.

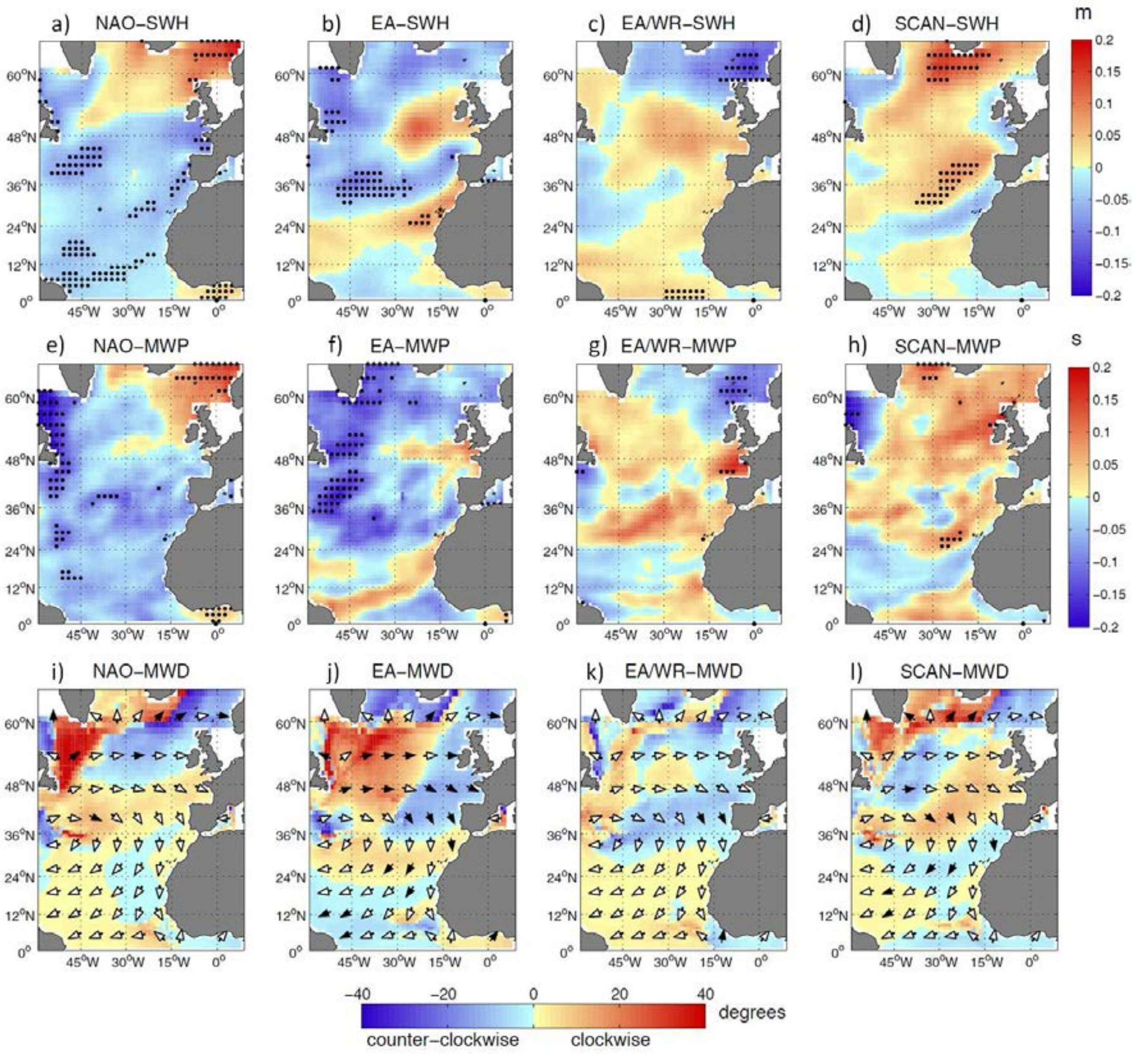

Figure 4.S3. Summer (JJAS) regression coefficient between hindcasted wave parameters and climate indices for the period 1989-2009. Black dots and black arrows denote a minimum 95% level of significance. Arrows indicate winter averaged MWD and coloured areas denote the change in direction from the winter averaged value in both clockwise (red) and counter-clockwise sense (blue).

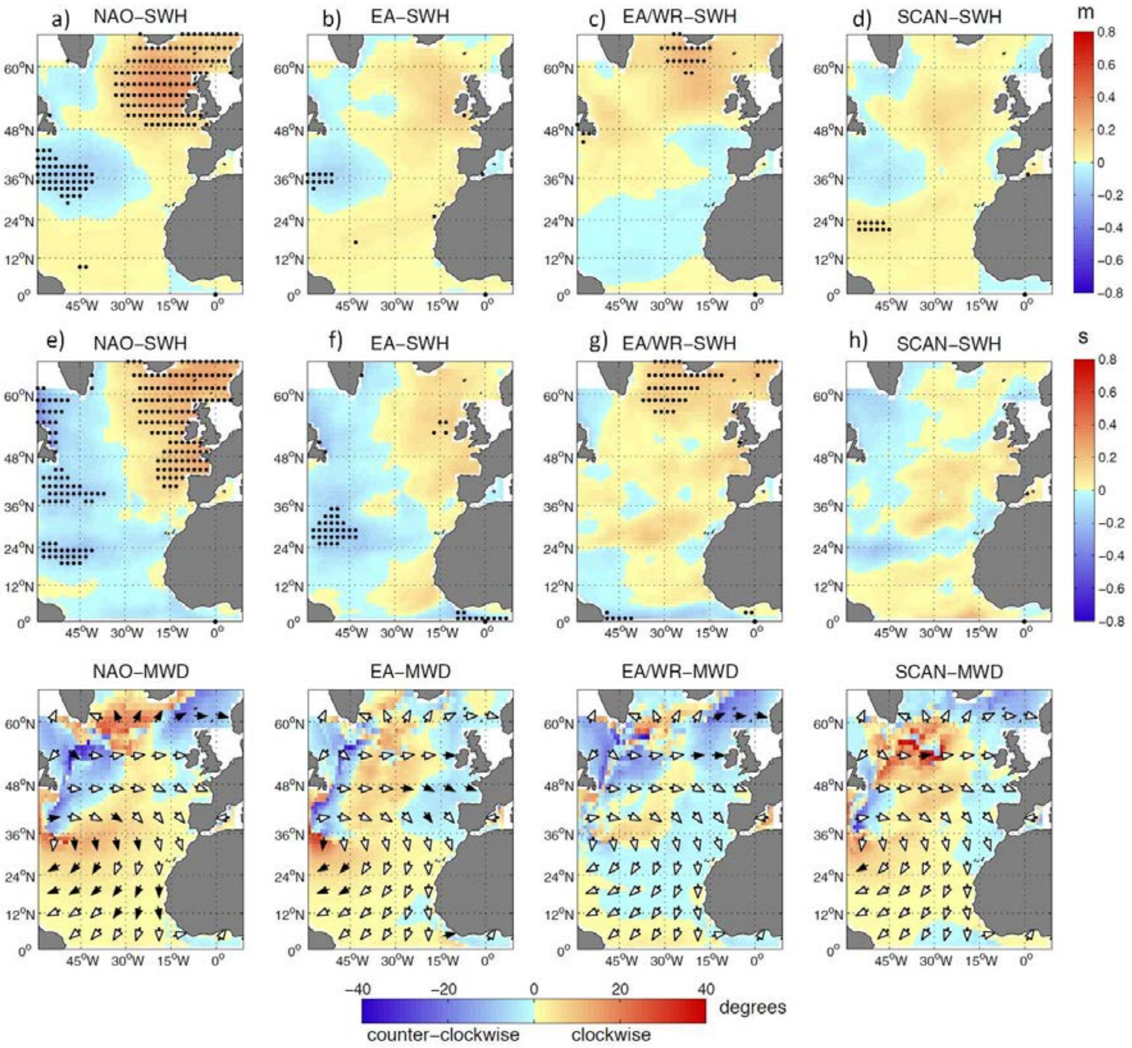

Figure 4.S4. Spring (MAMJ) regression coefficient between climate indices and hindcasted SWH, MWP and MWD anomalies for the period 1989-2009. Black dots and black arrows denote a minimum 95% level of significance. Arrows indicate winter averaged MWD and coloured areas denote the change in direction from the winter averaged value in both clockwise (red) and counter-clockwise sense (blue). Units are m per unit index, s per unit index and degrees per unit index.

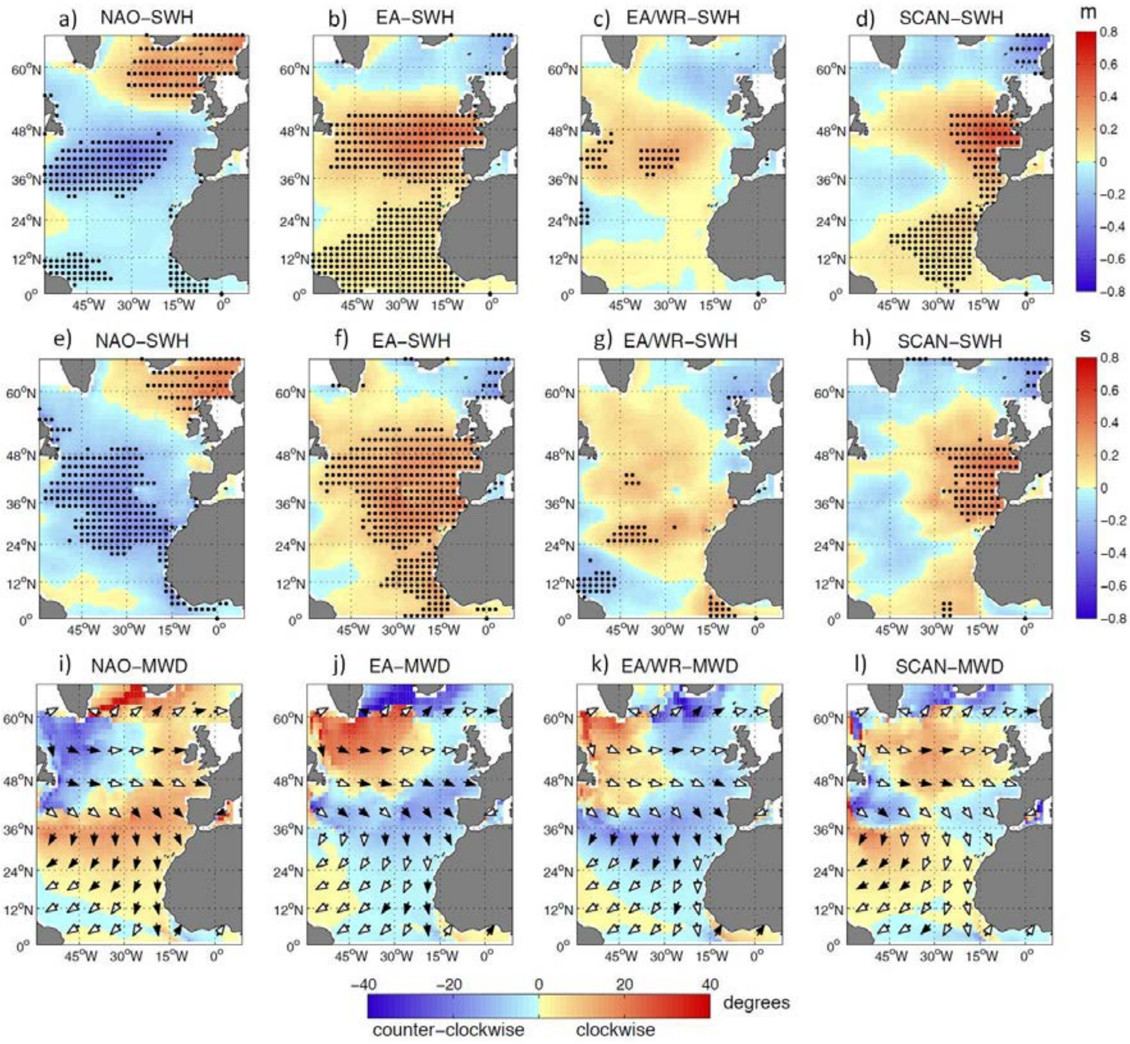

Figure 4.S5. Autumn (SOND) regression coefficient between climate indices and hindcasted SWH, MWP and MWD anomalies for the period 1989-2009. Black dots and black arrows denote a minimum 95% level of significance. Arrows indicate winter averaged MWD and coloured areas denote the change in direction from the winter averaged value in both clockwise (red) and counter-clockwise sense (blue). Units are m per unit index, s per unit index and degrees per unit index.

Acknowledgments

This work has been carried out in the framework of the projects VANIMEDAT-2 (CTM2009-10163-C02-01, funded by the Spanish Marine Science and Technology Program and the E-Plan of the Spanish Government) and ESCENARIOS (contract funded by the Agencia Estatal de METeorología). A. Martínez-Asensio acknowledges an FPI grant associated with the VANIMEDAT-2 project, M. Marcos and G. Jordà acknowledge a “Ramón y Cajal” contract funded by the Spanish Government, G. Jordà also acknowledges a postdoc contract funded by the Comunitat Autònoma de les Illes Balears and the European Social Fund, and M.N. Tsimplis and X. Feng acknowledge Lloyd's Register Foundation, which supports the advancement of engineering-related education, and funds research and development that enhances safety of life at sea, on land and in the air. We want to thank Puertos del Estado, Instituto Hidrográfico - Marinha and ISDM for kindly providing the buoy data and NOAA for the climate indices and the atmospheric reanalysis. Bathymetry was obtained from the GEBCO Digital Atlas published by the British Oceanographic Data Centre, on behalf of IOC and IHO, 2003. All co-authors have no conflict of interest to declare.

Bibliography

Bacon, S., & Carter, D. J. T. (1993). A connection between mean wave height and atmospheric pressure gradient in the North Atlantic. Int. J. Climatol., 13, 423–436

Barnston, A. G., & Livezey, R. E. (1987). Classification, seasonality and persistence of low-frequency atmospheric circulation patterns. Mon.Wea. Rev. 115, 1083–1126.

Bauer, E., (2001). Interannual changes of the ocean wave variability in the North Atlantic and in the North Sea. Climate Research 18, 63–69.

Bertin, X., Prouteau, E., Letetrel, C., (2013). A significant increase in wave height in the North Atlantic Ocean over the 20th century. Global Planet. Change 106, 77–83.

Caires, S., & Sterl, A. (2003). Validation of ocean wind and wave data using triple collocation. J. Geophys. Res., 108, 3098.

Carter, D. J. T. & Draper, L. (1988). Has the North-East Atlantic become rougher ?. Nature, 332, 494.

Charles, E., Idier, D., Thiébot, J., Le Cozannet, G., Pedreros, R., Ardhuin, F., & Planton S. (2012). Present wave climate in the Bay of Biscay: spatiotemporal variability and trends from 1958 to 2001. Journal of Climate, 25, 2020-2035.

Cotton, P. D., & Challenor, P. G. (1999). North Atlantic climate variability and the North Atlantic Oscillation index. In Proceedings of the 9th ISOPE Conference, Brest, France, May 30–June 4 1999, vol. 3, 1999 pp. 153–157.

Dee, D. P., Uppala, S. M., Simmons, A. J., Berrisford, P., Poli, P., Kobayashi, S., ... & Vitart, F. (2011). The ERA-Interim reanalysis: Configuration and performance of the data assimilation system. Quarterly Journal of the

Royal Meteorological Society, 137(656), 553-597.

Draper, N.R., & Smith, H. (1998). Applied Regression Analysis. Wiley-Interscience, Hoboken, NJ pp. 307–312.

Deser, C. (2000). On the teleconnectivity of the Arctic Oscillation, Geophys. Res. Lett., 27, 779–782.

Dodet, G., Bertin, X., & Taborda, R. (2010). Wave climate variability in the North-East Atlantic Ocean over the last six decades. Ocean Modelling 31, 120–131.

Dupuis, H., Michel, D. & Sottolichio, A. (2006). Wave climate evolution in the Bay of Biscay over two decades. J. Mar. Syst., 63, 105–114.

Feng, X., Tsimplis, M. N., Quartly, G. D. & Yelland, M. J. (2014a). Wave height analysis from 10 years of observations in the Norwegian Sea, Continental Shelf Research, Volume 72, Pages 47-56.

Feng, X., Tsimplis, M. N., Yelland, M. J. & Quartly, G. D. (2014b). Changes in significant and maximum wave heights in the Norwegian Sea. Global and Planetary Change, Volume 113, Pages 68-76.

Gulev, S. K., & Grigorieva, V. (2006). Variability of the winter wind waves and swell in the North Atlantic and North Pacific as revealed by the voluntary observing ship data, J. Clim., 19, 5667–5685.

Günther, H., Hasselman, S., & Jansen, P. A. E. (1992). The WAM model cycle, 4. Technical Report 4. DKRZ.

Hasselmann, S., Brüning, C., Hasselmann, K., & Heimbach, P. (1996). An improved algorithm for retrieval of ocean wave spectra from synthetic aperture radar image spectra. J. Geophys. Res., 101, 16 615-16 629

Hurrell, J.W., Kushnir, Y., Ottersen, G., & Visbeck, M. (2003). An overview of the North Atlantic Oscillation. In: The North Atlantic Oscillation: Climatic Significance and Environmental Impact [Hurrell, J.W., et al. (eds.)]. Geophysical MonographVol. 134, American Geophysical Union, Washington, DC, pp. 1–35Itoh H. 2008. Reconsideration of the true versus apparent arctic oscillation. Journal of Climate 21(10): 2047–2062.

Izaguirre, C., Méndez, F. J., Menéndez, M., & Losada, I. J. (2011). Global extreme wave height variability based on satellite data. Geophysical Research Letters, 38 (L10607)

Kalnay, E., Kanamitsu, M., Kistler, R., Collins, W., Deaven, D., Gandin, L., Iredell, M., Saha, S., White, G., Woollen, J., Zhu, Y., Chelliah, M., Ebisuzaki, W., Higgins, W., Janowiak, J., Mo, K.C., Ropelewski, C., Wang, J., Leetmaa, A., Reynolds, R., Roy Jenne, R., & Joseph, D.

(1996). The NCEP/NCAR 40-year reanalysis project. Bulletin of the American Meteorological Society 77, 437.

Kistler, R., Collins, W., Saha, S., White, G., Woollen, J., Kalnay, E., ... & Fiorino, M. (2001). The NCEP-NCAR 50-year reanalysis: Monthly means CD-ROM and documentation. Bulletin of the American Meteorological society,82(2), 247-267.

Kushnir, Y., Cardone, V. J., Greenwood, J. G., & Cane, M. (1997). On the recent increase in North Atlantic wave heights. J. Climate, 10, 2107-2113.

Le Cozannet, G., Lecacheux, S., Delvallee, E., Desramaut, N., Oliveros, C., & Pedreros, R. (2011). Teleconnection pattern influence on sea-wave climate in the Bay of Biscay. Journal of Climate 24 (3), 641–652.

Minguez, R., Espejo, A., Tomas, A., Mendez, F. J., & Losada, I. J. (2011). Directional calibration of wave reanalysis databases using instrumental data. Journal of Atmospheric and Oceanic Technology 28, 1466–1485.

Queffeulou P. (2004). Long term validation of wave height measurements from altimeters, Marine Geodesy, 27, 495-510.

Queffeulou, P., & Croizé-Fillon, D. (2010). Global altimeter SWH data set, version 7, <ftp://ftp.ifremer.fr/ifremer/cersat/products/swath/altimeters/waves/>.

Rogers, J.C. (1990). Patterns of low frequency monthly sea level pressure variability (1899-1986) and associated wave cyclone frequencies. J. Climate, 3, 1364-1379.

Semedo, A., Suselj, K., Rutgersson, A., & Sterl, A. (2011). A global view on the wind sea and swell climate and variability from era-40 Journal of Climate, 24, pp. 1461-1479.

Shimura T., Mori N. & Mase, H. (2013). Ocean waves and teleconnection patterns in the Northern Hemisphere, Journal of Climate, 26, pp.8654-8670.

Samuelsson P., Jones C., Willén U., Ullerstig A., Gollvik S., Hansson U., et al. (2011). “The Rossby Centre Regional Climate model RCA3: model description and performance” Tellus A. (2011).

Thompson, D. W., & Wallace, J. M. (1998). The Arctic Oscillation signature in the wintertime geopotential height and temperature fields. Geophysical Research Letters, 25(9), 1297-1300.

Tolman, H. L. (2009). User manual and system documentation of WAVEWATCH III version 3.14. NOAA/NWS/NCEP/MMAB Technical Note 276, 194 p.

Tsimplis, M.N.,Woolf, D.K., Osborn, T.J.,Wakelin, S., Wolf, J., Flather, R., &

Shaw, A.G.P. (2005). Towards a vulnerability assessment of the UK and northern European coasts: the role of regional climate variability. Phil. Trans. R. Soc. A 363, 1329–1358.

WAMDI Group (1988). The WAM model—a third generation ocean wave prediction model. J. Phys. Oceanogr., 18, 1775–1810.

Woolf, D.K., Cotton, P.D., & Challenor, P.G. (2002). Variability and predictability of the North Atlantic wave climate. Journal of Geophysical Research 107 (C10), 9–23.

Young, I. R. (1999). Seasonal variability of the global ocean wind and wave climate, Int. J. Climatol., 19, 931–950.

Young, I. R., Zieger, S., & Babanin, A. (2011). Global trends in wind speed and wave height, Science, 332(6028), 451–455.

Chapter 5

On the ability of statistical wind-wave models to capture the variability and long-term trends of the North Atlantic winter wave climate

> —Le he contado todas estas cosas—dijo—,
> como si ya hubieran ocurrido. También hubiera podido contarlas como si fueran a ocurrir
> en el futuro. Para mí, no hay demasiada diferencia.
>
> —I've described all these events —he said—
> , as if they'd already happened. I might just as well have described them as if they still lay
> in the future. To me, there's very little difference.
>
> Michael Ende, *Momo* (1973)

This chapter has been published in:

- Martínez-Asensio, A., Marcos, M., Tsimplis, M.N., Jordà, G., Feng. X., Gomis, D., 2015. On the ability of statistical wind-wave models to capture the long-term trends in winter wave climate. Ocean Modelling (in revision)

Abstract

A dynamical wind-wave climate simulation covering the North Atlantic Ocean and spanning the whole 21st century under the A1B scenario has been compared with a set of statistical projections using atmospheric variables or large scale climate indices as predictors. As a first step, the performance of all statistical models has been evaluated for the present-day climate; namely they have been compared with a dynamical wind-wave hindcast in terms of winter Significant Wave Height (SWH) trends and variance as well as with altimetry data. For the

projections, it has been found that statistical models that use wind speed as independent variable predictor are able to capture a larger fraction of the winter SWH inter-annual variability (68% on average) and of the long term changes projected by the dynamical simulation. Conversely, regression models using climate indices, sea level pressure and/or pressure gradient as predictors, account for a smaller SWH variance (from 2.8% to 33%) and do not reproduce the dynamically projected long term trends over the North Atlantic. Investigating the wind-sea and swell components separately, we have found that the combination of two regression models, one for wind-sea waves and another one for the swell component, can improve significantly the wave field projections obtained from single regression models over the North Atlantic.

5.1 Introduction

Changes in wave climate have received much attention in recent years due to their impact on coastal and offshore structures and ecosystems. Numerous wave climate simulations under different future scenarios of greenhouse gases (GHGs) emissions have been generated at both global and regional scales using numerical wave models. The North Atlantic is one of the most widely studied regions. Many earlier works have pointed to a decrease in wave heights as a consequence of global warming. For example, Mori et al. (2010) projected future decreases in the wave heights over the North Atlantic at mid-latitudes by using wind fields generated by the MRI-JMA General Circulation Model (GCM) run under the A1B scenario. Likewise, Hemer et al. (2012) projected future decreases in wave heights during winter and changes in wave directions over all the North Atlantic by using the ECHAM5 GCM and CSIRO Mk3.5 GCM wind fields, both under the A2 climate scenario. Semedo et al. (2013) projected decreases in both wave heights and periods over the North Atlantic during the winter season by using ECHAM5 GCM wind fields under the A1B scenario. Fan et al. (2013) projected decreases of wave heights during winter over the North Atlantic and increases over the north-eastern sector by using a three member ensemble forced by CM2 GCM, HadCM3 GCM and ECHAM5 GCM wind fields under the A1B scenario. In a subsequent paper, Fan et al. (2014) used the same model ensemble to obtain winter trends for the wind-sea and swell components separately. Andrade et al. (2007) projected decreases of wave heights and clockwise changes in wave directions and investigated their effects along the Portuguese coast. More local studies also exist in the region. In particular, Charles et al. (2012) projected very similar winter wave height decreases over the Bay of Biscay by using the ARPEGE-Climat GCM under three different future climate scenarios (B1, A1B, A2). All the simulations referred above are based on dynamical models forced with the surface wind fields from atmospheric models. The simulated wave parameters defining the wave climate are significant wave height (SWH), mean wave period (MWP) and mean wave direction (MWD), as well as their separation into local (wind sea) and remotely-forced (swell) waves. Both components can be properly modelled when using global wind-wave models. Regional models can also be suitable to model the swell component, although they require to be nested into larger domains to account for remotely generated swell; in turn, they usually provide higher spatial resolution.

Alternative approaches to explore wave changes in future climates cover a wide variety of statistical methods that can be classified into three main types (Wilby et al., 2004): i) regression methods, ii) weather generators and iii) weather typing schemes. Each method has its own advantages and shortcomings. Briefly, weather generators are stochastic models that replicate the statistical properties of the observed sequences of events, such as mean value and variance (Ailliot et al., 2014; Wilks, 1998). Weather typing schemes establish the relationship between atmospheric and wave parameters based on a division in weather classes, as shown for instance in Camus et al., (2014). Among these, the analogue method (Lorenz, 1969; Zorita et al., 1995) and the Monte Carlo method are also weather typing methods.

Among the regression methods, the canonical correlation analysis used by Wang et al., (2004) to simulate future SWH changes is a first example. Some of the most frequently used regression methods are based on transfer functions, which represent the relationship between observed wave parameters, usually SWH, and atmospheric variables such as the squared wind speed (W=u2+v2), sea level pressure (P) and/or the squared sea level pressure gradient (G) representing the geostrophic wind (that is the sum of the squared zonal and squared meridional SLP gradients). The atmospheric parameters obtained from model output under increased GHG scenarios can then be used to estimate the changes in the wave field through the statistical relationship between them obtained for the present-day period, assuming that such relationship holds also for the future period. Examples of application of such methodology can be found in Wang and Swail (2006), who used global anomalies of P and G as predictors in different regression models to simulate future SWH. Likewise, Wang et al. (2010) compared both dynamical and regression models to simulate future SWH changes over the North Atlantic at hourly and seasonal scales. They tested the inclusion of W as a predictor in a set of regression models, but they concluded that it was preferable to use P and G predictors to simulate future changes on SWH due to the bias in the winds produced by the atmospheric models. Wang et al., (2012) and Wang et al., (2014) improved the regression model predictability by including the Principal Components (PCs) of P and G as predictors, which result in a better representation of the swell component at hourly time scales. More recently, Casas-Prat et al. (2014) have developed a more complex regression model that better accounts for the swell component to simulate future changes in the wave climate of the Western Mediterranean. In a similar way to atmospheric variables, large scale climate indices can also in principle be used as proxies for the statistical projections of waves (Woolf et al., 2002; Tsimplis et al., 2005; Feng et al., 2014a). The obvious constraint is that they must be correlated for present-day climate with both wind sea and swell wave parameters (Shimura et al., 2013; Martínez-Asensio et al., accepted).

The statistical techniques offer low computational effort relative to dynamical modelling, which in turn permits the generation of larger ensembles resulting in a better understanding and quantification of uncertainties. Wang and Swail (2006) carried out an analysis of the uncertainty in SWH projections over the North Atlantic by running a set of statistical simulations forced with three different climate models (CGCM2, HadCM3 and ECHAM4/OPYC3) and three different scenarios (IS92a, A2 and B2) at a seasonal scale. They found that the uncertainty associated with the GCM used to feed the statistical model was much larger than that associated with the emission scenarios. Similar conclusions were pointed out by Charles et al. (2012). Hemer at al. (2013) went further into the uncertainty analysis by taking into account five independent studies projecting future changes in wave climate (namely those carried out by Wang and Swail, 2006; Mori et al., 2010; Hemer et al., 2012; Semedo et al., 2013; and Fan et al., 2013). They considered a total of four climate scenarios (A2, A1B, B2 and IS92a), six GCMs (ECHAM5, CSIRO-Mk3.5, GFDL-CM2.1, HadCM3, ECHAM4 and CGCM2), an ensemble mean of three CGCM2 simulations produced with different initial conditions, two ensemble means of 18 and 23 CMIP3 members, a set of three dynamical wave models (WaveWatch III, SWAN and WAM), one statistical model and three wave parameters (SWH, MWP and MWD). They found that the method used to obtain regional wave climates (the regional climate model, the downscaling technique, the wave model approach and the use of different predictors in statistical models) is also a high source of uncertainty.

In our study the accuracy of a set of transfer function statistical models to project the future wave climate over the North Atlantic Ocean is studied. Our aim is to compare a wide set of these statistical models against a reference dynamical model and quantify their performances. The chosen statistical models are based on some of the most widely used transfer functions; the set was complemented by other, more specific models as well as by models based on large scale climate indices.

A wind-wave hindcast and an atmospheric reanalysis are used to calibrate all the statistical models for the period 1958-2002. Altimetry SWH observations are used to validate both the dynamical and statistical models. Conversely, altimetry is not an option to calibrate the statistical models because of the short period spanned by observations. Then, the atmospheric output of a climate model (ECHAM5) run under the A1B emission scenario for the period 2000-2100 is used to obtain the changes in the atmospheric parameters used as statistical predictors and hence for the prediction of the winter SWH fields of the future. ECHAM5 is considered one of the best CMIP3 GCMs in simulating the recent past climate conditions in terms of inter-annual variability over the North-East Atlantic (Pérez et al.,2014).

The same output is used to force a dynamical regional wave model to project winter SWH, MWP and MWD fields. The differences between the dynamical and statistical approximations of the future wave field as well as their respective limitations are discussed.

The paper is organized as follows: the dynamical and statistical models and their forcing are presented in section 2. The models are validated for present-day climate in section 3. Projections of wave climate are presented in section 4. In the last section results are discussed and conclusions are outlined.

5.2 Data set and methodology

The set of dynamical and statistical simulations and the procedure to generate all them is schematically shown in Fig. 5.1, while the details are given in the sections below.

5.2.1 Dynamical simulations

Two wind-wave hindcasts over the North Atlantic (hereinafter HE40 and HEI) were obtained by forcing a third generation wave model that explicitly solves the wave transport equation (the WAM model, see WAMDI, 1988; Günther et al., 1992) with 6-hourly surface wind fields from the atmospheric reanalysis ERA-40 (1958-2002) with a spatial resolution of 2.5x2.5 degrees and ERA-INTERIM (1989-2009) with a spatial resolution of 0.5x0.5 degrees, respectively. HE40 was used for the calibration of the statistical models, whereas HEI was used as a basis for validation purposes (more details are given in section 3). In a third simulation the WAM model was forced with 6-hourly surface wind fields (1.875x1.875 degrees of spatial resolution) from the Max Plank Institute (MPI) ECHAM5 atmospheric GCM (Roeckner et al., 2003) run for the period 1950-2100. The period 1950-2000 is a historical run forced with observed GHG concentrations (the corresponding wave simulation will be referred to as DynHist), while the period 2001-2100 is a projection under the A1B emission scenario (the corresponding wave simulation will be referred to as DynProj).

The domain of the WAM model was set to cover the North Atlantic region (from 1ºN to 67ºN and from 59ºW to 8ºE) with spatial resolution varying between 2.5 km and 50 km (see Fig. 5.S1 in Supplementary information). Wind fields were bi-linearly interpolated onto the described model grid. This is the configuration routinely used by the Spanish Port Authority for operational purposes. The temporal resolution of the output is 3 hours. The separation of the wind-sea and swell components of the wave field is performed as in Hasselmann et al. (1996): the peaks (local maxima) of the directional wave spectrum are identified and attributed either to the sea or to the swell component depending on the period and direction of each peak. When the peak is in the same direction of the wind stress and the period is lower than 10 s, the waves are considered to be part of the wind-sea component; otherwise they are identified as swell.

For the present study, all 3-hourly fields of wave parameters (SWH and its wind and swell components) corresponding to the two hindcasts HE40 and HEI and to the ECHAM simulation, were monthly averaged and bi-linearly interpolated onto a regular grid of 1x1 degree over the North Atlantic domain. At each grid point, the mean seasonal cycle of each wave parameter was obtained by averaging each calendar month during the period 1961-1981 and removed from all the simulations. The resulting anomalies were used for all purposes.

5.2.2 Statistical regressions using atmospheric variables and climate indices

Winter (DJFM) anomaly fields (i.e., the temporal anomalies at each grid point defined above) of SWH from the HE40 run and of atmospheric variables from the ERA-40 reanalysis were used to estimate the regression parameters of the statistical models. Prior to the regression, 6-hourly W and P fields from ERA40 reanalysis were interpolated onto the same 1x1 grid as HE40. Subsequently, P fields were used to obtain 6-hourly G fields, i.e., as the squared sum of the zonal and meridional SLP gradients (equation 4 in the Appendix of Wang et al, 2008).

The regressions followed the most commonly used models in the literature and were completed with additional models. Recently developed statistical models appropriate for higher temporal resolution fields (6-hourly or daily) have not been considered here (e.g. those developed by Casas-Prat, 2014 or Camus et al., 2014) as far as we focus on seasonal to interannual time scales. The models are listed in the following with the corresponding reference and an identification code that will be used throughout the paper:

M1: $SWH = a + b*P$ (Wang et al., 2004)
M2: $SWH = a + b*G$ (Wang et al., 2004)
M3: $SWH = a + b*W$ (Wang et al., 2010)
M4: $SWH = a + b*P + c*G$ (Wang and Swail, 2006)
M5: $SWH = a + \sum_{i=1}^{n} b_i\, PC_i\, (P)$ (Wang et al., 2004)
M6: $SWH = a + \sum_{i=1}^{n} b_i\, PC_i\, (G)$ (Wang et al., 2004)
M7: $SWH = a + \sum_{i=1}^{n} b_i\, PC_i\, (W)$
M8: $SWH = a + b*P + \sum_{i=1}^{n} c_i\, PC_i\, (P)$ (Wang and Swail, 2006)
M9: $SWH = a + b*G + \sum_{i=1}^{n} c_i\, PC_i\, (G)$ (Wang and Swail, 2006)
M10: $SWH = a + b*W + \sum_{i=1}^{n} c_i\, PC_i\, (W)$
M11: $SWH = a + b*P + c*G + \sum_{i=1}^{n} d_i\, PC_i\, (P) + \sum_{i=1}^{n} e_i\, PC_i\, (G)$ (Wang et al, 2012; 2014)
M12: $SWH = a + b*NAO$ (Woolf et al., 2002)
M13: $SWH = a + b*EA$
M14: $SWH = a + b*NAO + c*EA + d*EA/WR + e*SCAN$
M15: $SWHw = a + b*W$
M16: $SWHs = a + \sum_{i=1}^{n} b_i\, PC_i\, (W)$
M17: $SWH = \sqrt{(< SWHw^2 > + < SWHs^2 >)}$

where PC in M5-M11 and M16 stands for the Principal Components obtained from a singular value decomposition of the covariance matrix (see e.g. Wallace, et al., 1992) of the winter anomalies of ERA40 P, W and G fields spanning the period 1958-2002; n is the number of PCs included in the model, sorted by decreasing explained variance. They were used by Wang et al. (2012; 2014) as large-scale predictors in order to account for changes in the swell component, which is related to remote atmospheric forcing. Namely, Wang et al (2012) used 6-hourly time series and found that the inclusion of a large number of PCs (n~30) did not have an impact on trends, but resulted in a better representation of the large-scale patterns that generate swell. Another worth noting point is that model M11 corresponds to the particular case of no autoregressive process explained in Wang et al (2012) (their equation 2). We chose this simplified case because we deal with seasonal data, in contrast with the 6-hourly temporal resolution used by Wang et al (2012), and we do not expect significant time-lag correlations between seasons.

For each model with at least two predictors, a forward/backward stepwise regression was applied at each grid point in order to determine the number of predictors to be included (Draper and Smith, 1998) and their corresponding coefficients (see Appendix 5.A). This procedure selects the most correlated independent variable and removes its influence through a regression analysis. Then it checks for correlation between the rest of the independent parameters and

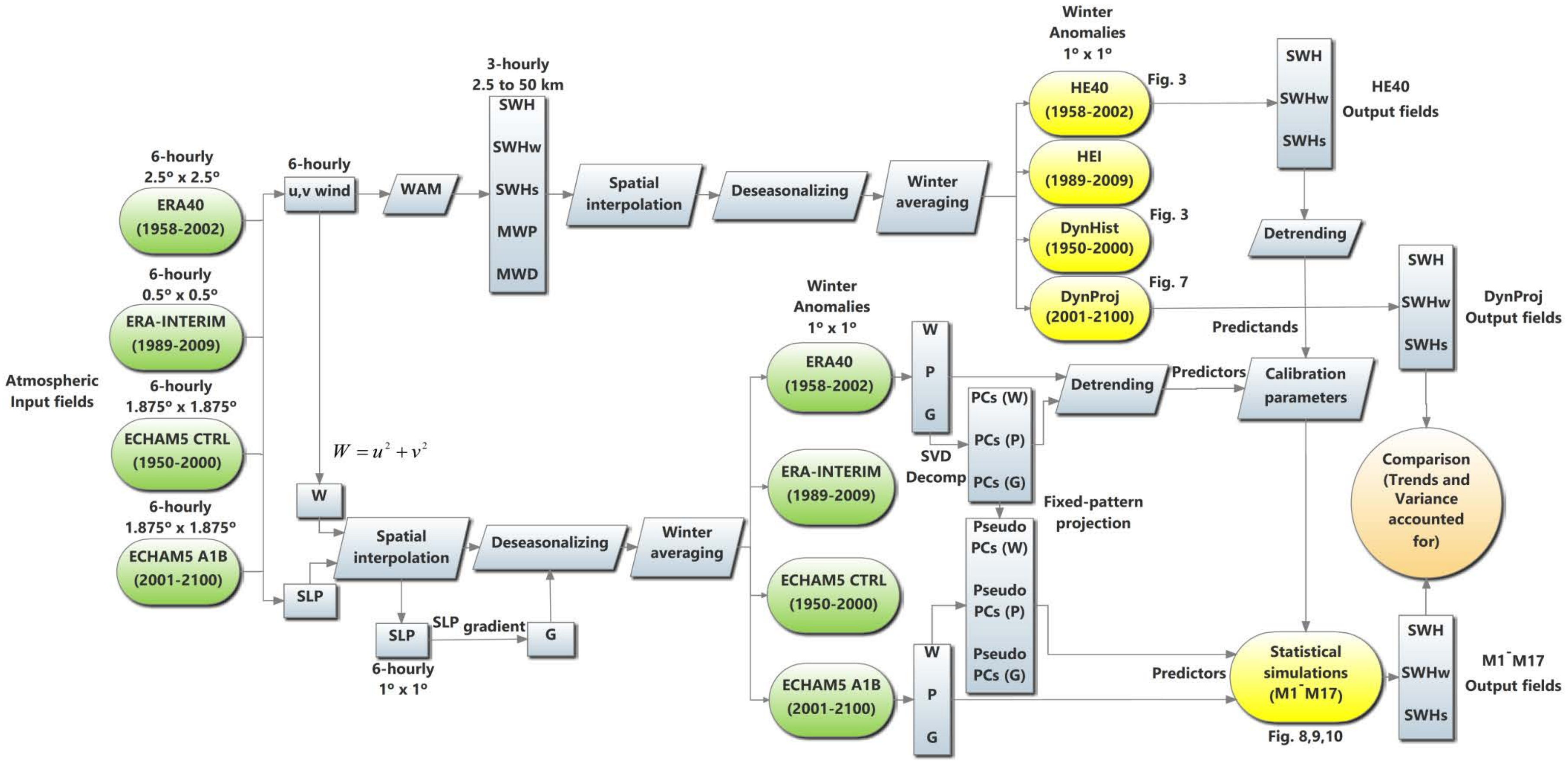

Figure 5.1. Dynamical and statistical simulations flowchart. Green colours indicate atmospheric fields and yellow colours indicate wave fields.

the residual signal, until the correlation becomes non-significant. When more than one predictor account for the same part of variability the regression model favours the predictor that accounts for the highest percentage of total variability. In other words, the statistical fit calculates the value of the coefficients and defines the number of parameters that optimise the fit to SWH data at each point. This also applies to the models using PCs as predictors. We have established a maximum number of PCs n=6 because for larger values the increase in explained variance was negligible (the fact that a small number of PCs is requested is due to working with seasonal values). The linear trends from all dependent and independent variables were removed before the estimation of the regression parameters.

The regression coefficients estimated for the historical period were then used to project winter SWH along the 21st century using the projected atmospheric fields of the ECHAM5 GCM. Winter (DJFM) anomaly fields of P, G and W from ECHAM5 and their corresponding PCs were used as predictors to obtain projections of winter SWH for the period 1950-2100. It is worth noting that the projected atmospheric fields are not detrended and therefore the underlying assumption is that the correlation at inter-annual scales, which determines the regression parameters, remains unaltered at lower frequencies. This means that a long term trend in the predictor will result in a trend in winter SWH with the sign and intensity given by the regression. The PCs in M5-M11 were obtained using a fixed-pattern projection approach, which consists of projecting winter anomaly fields from ECHAM5 onto the PCs obtained from the ERA-40 reanalysis used for the regression (Wang et al., 2004). In this way, the correspondence of the regression coefficients between these so called pseudo-PCs and the original PCs used to train the model is ensured. An eventual disadvantage of the fixed-pattern projection approach is that the percentage of hindcast variability explained by each original PC is not necessarily the same than for the corresponding pseudo-PC. To check this point, we have compared the percentage of winter SWH variance accounted for in HE40 and in DynHist by the 6 leading PCs and pseudo-PCs, respectively. For HE40 we obtained variance fractions of 50% (M5 model), 41% (M6 model) and 68 % (M7 model); for DynHist the fractions were 36%, 33% and 45%, respectively.

The climate indices considered in this work correspond to the most relevant modes of atmospheric variability over the North Atlantic, namely the North Atlantic Oscillation (NAO), East Atlantic Pattern (EA), East Atlantic/Western Russian Pattern (EA/WR) and Scandinavian Pattern (SCAN). The climate indices were obtained for the same period than the atmospheric parameters (1958-2002) using P fields from ERA-40. Monthly anomalies of P fields over the Northern Hemisphere (20ºN-90ºN) were first computed removing the mean seasonal cycle at each grid point and then averaged for the winter season

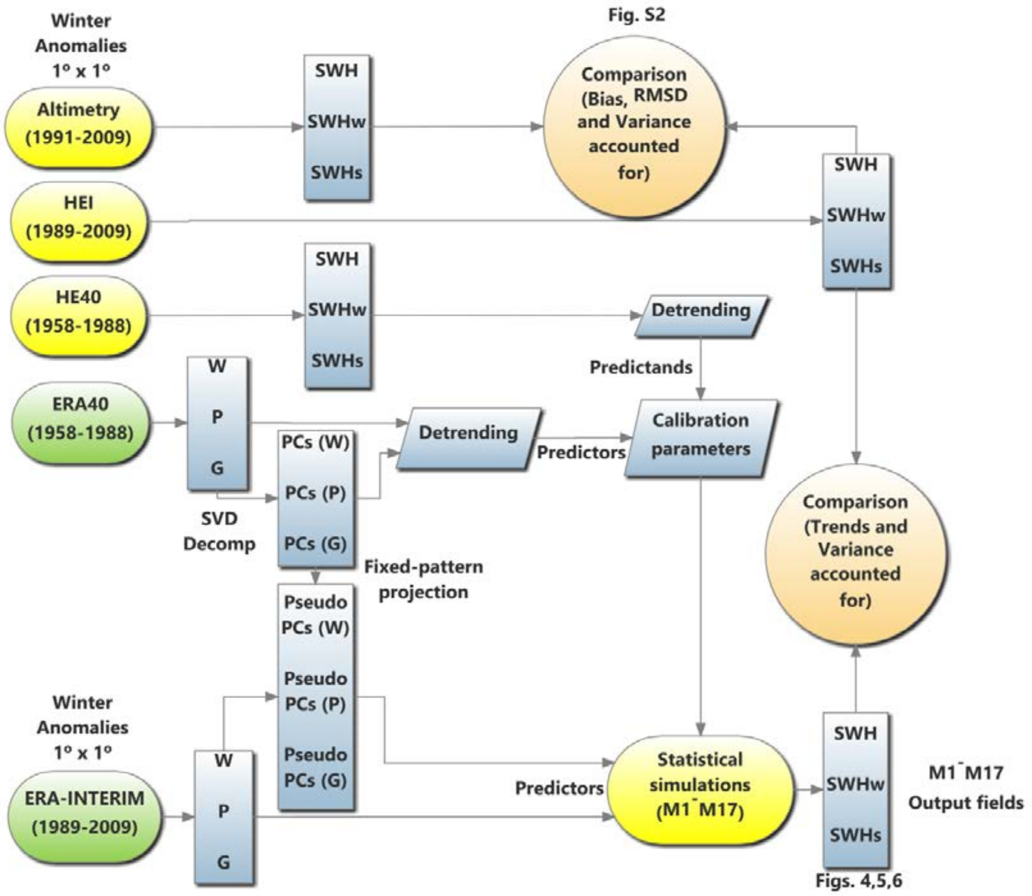

Figure 5.2. Validation process flowchart. Green colours indicate atmospheric fields and yellow colours indicate wave fields.

(DJFM). The EOFS were obtained from a singular value decomposition of the covariance matrix of P fields. Finally, the first ten EOFs were orthogonally rotated applying a “Varimax” rotation (Richman, 1986). The aim of the EOFs rotation was to reduce the mode complexity in order to obtain a more physical interpretability of the modes. The percentage of P variance accounted for by the ten selected rotated EOFs was 90.1%. Seven of them (accounting for 72% of the variance) were similar to those found by the NOAA Climate Prediction Center (http://www.cpc.ncep.noaa.gov/data/teledoc/telecontents.shtml) using monthly Z500 fields from NCEP/NCAR atmospheric reanalysis (Kistler et al., 2001) spanning the period 1950-2010. These were the SCAN (19%), NAO (16%), West-Pacific (WP) (10%), EA/WR (9%), Pacific-North American (PNA) (7%), Tropical-Northern Hemisphere (TNH) (6%) and EA (5%). The corresponding PCs of the leading rotated EOFs with a strong signal over the North Atlantic wave climate (Izaguirre et al, 2011; Shimura et al., 2013) were finally selected; they correspond to the indices NAO, EA, EA/WR and SCAN, which were used as independent variables to obtain the parameters of the regression models M12, M13 and M14. A model including the ten PCs was rejected because it did not result in any significant improvement. The same fixed-pattern method described in section 2.2 was used to obtain projections of the climate indices during 1950-2100. That is, simulated winter anomaly fields of P from ECHAM were projected onto the selected rotated PCs derived from the ERA40 reanalysis. The resulting climate indices were finally introduced in models M12 to M14 to obtain SWH anomalies during 1950-2100.

Models M1-M14 simulate total SWH. We further used two additional models: M15, describing the wind sea (SWHw) field, and M16, describing the swell component (SWHs). Winter (DJFM) anomalies of SWHw and SWHs were obtained from HE40 in the same way as for SWH and regressed against atmospheric variables from ERA40. The independent parameters used as predictors were winter anomaly W for SWHw (adequate to describe the local character of the field) and the corresponding PCs of W (accounting for large-scale processes) for SWHs. In order to provide estimates for total SWH, the relationship between this field and its components SWHw and SWHs was used. At quasi-instantaneous (3h) scales SWH, SWHw and SWHs from HE40 verify:

$$\mathrm{SWH}^2 = \mathrm{SWHw}^2 + \mathrm{SWHs}^2 \qquad (1)$$

The winter (DJFM) average was applied to the 3-hourly squared fields. In this way the monthly averages $< SWH\mathrm{w}^2 >$ and $< SWHs^2 >$ simulated with M15 and M16 can be combined to obtain winter SWH as:

$$< SWH >= \sqrt{(< SWH\mathrm{w}^2 > + < SWHs^2 >)} \qquad (2)$$

5.3 Validation of present-day simulated wave climate

The performance of all (dynamical and statistical) models was first evaluated for the present climate, using HEI as the basis for the evaluation. Altimetry SWH was also used for completeness, but only for some representative models (see Appendix 5.B and Suplementary information, in particular Fig. 5.S2). The validation process is schematically shown in Fig. 5.2, while the details are given in the sections below.

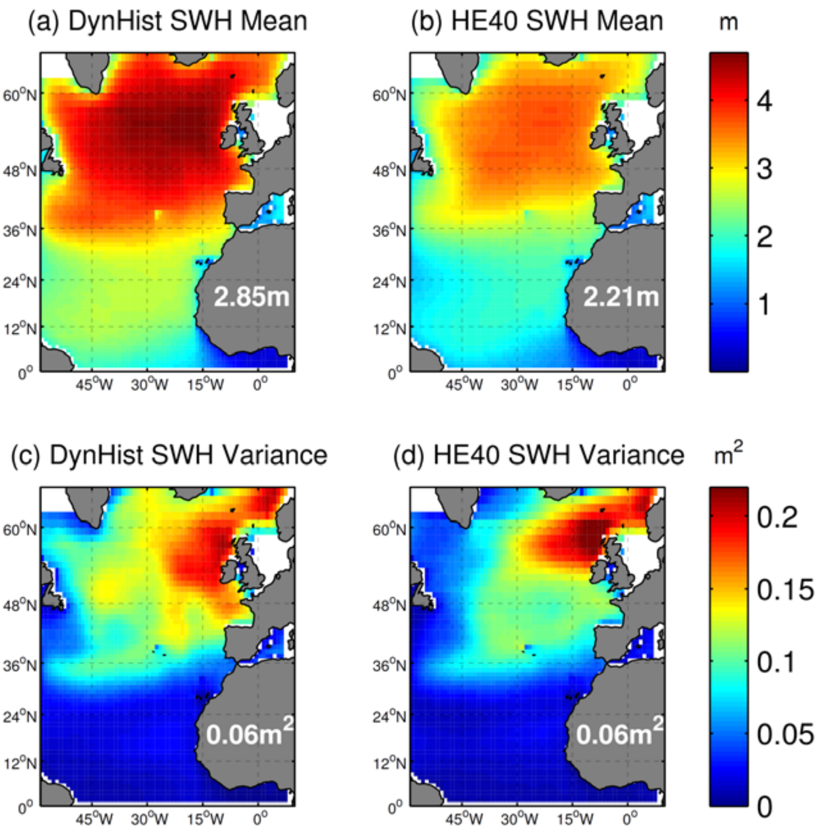

Figure 5.3. Mean value and variance of winter (DJFM) SWH fields for DynHist (a, c) and HE40 (b, d) for the common period 1958-1999. Spatially averaged values are also shown.

5.3.1 Dynamical simulation

The means and variances of winter (DJFM) averaged SWH fields derived from the historical run (DynHist) and the hindcast (HE40) are shown in Figs. 5.3a-d. The spatial patterns of the means are broadly similar, but DynHist shows higher values (differences of up to 0.5-1m) over most of the domain. The origin of such differences is that the winds in DynHist are stronger (0.9 m/s on average) than in HE40 over the North Atlantic (not shown). Regarding the variances, both DynHist and HE40 show maximum values of similar magnitude in the north-eastern sector of the domain (Fig. 5.3c-d). Also the spatial averaged variance is similar (0.1m2), though the two distributions show some differences at regional scale (e.g. in the Bay of Biscay).

5.3.2 Statistical simulations

The stability of the regression parameters of the statistical models was tested by estimating the parameters for the period 1958-1988 (using HE40) and then using

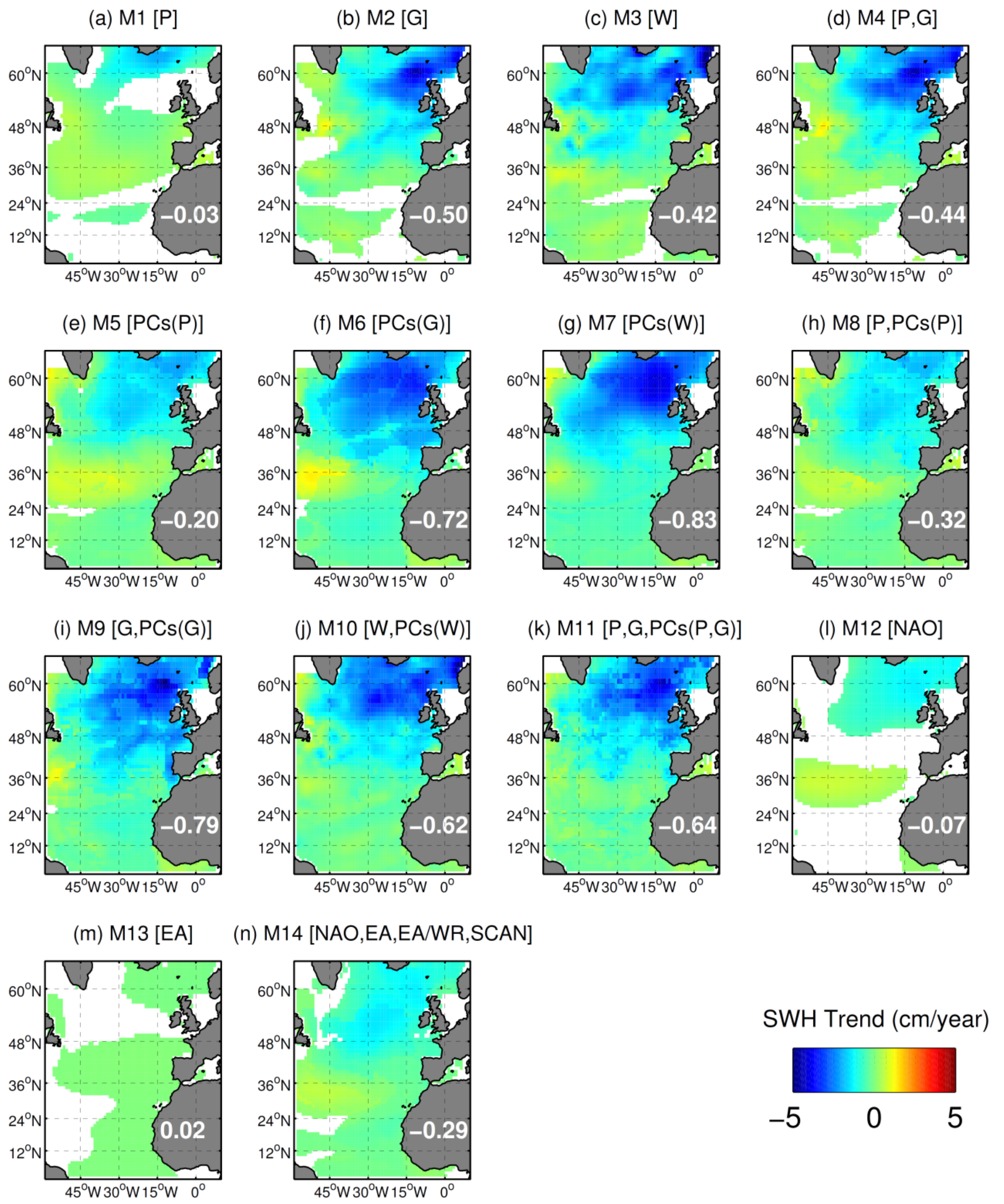

Figure 5.4. Winter SWH trends (cm/yr) inferred from the statistical models (a-n) for the period 1989-2009. Coloured areas denote model statistical significance (F-test) at 5% level. Spatially averaged values are also shown.

the parameters to predict SWH for the HEI period 1989-2009. Models M10, M11, M14 and M17 describing the period 1989-2009 were also compared with altimetry (spanning the period 1991-2009) in terms of bias, unbiased root mean square differences (URMSD) and variance accounted for (Fig. 5.S2). The comparison revealed that, in terms of bias, statistical models M17 and M10 were in better agreement with altimeter data than HEI, while HEI accounted for the highest percentage of variance.

Figure 5.4 shows linear trends of statistically simulated winter SWH during the period 1989-2009 fed with ERA-Interim. Coloured areas denote statistical significance (F-test) of the regression model at a 5% level. They must be compared with the trends obtained from HEI (Fig. 5.6a), which show negative values of up to -4 cm/yr over the northern sector of North Atlantic. Such negative trends had already been obtained by other authors, e.g. Young et al. (2011) obtained negative trends of up to -2.5 cm/year for the period 1985-2008, although they used annual SWH values from altimeter observations over large regions of the North Atlantic. Most of the models based on statistical downscaling (M1-M11) are able to reproduce the HEI trend pattern; the exceptions are those including P and/or its PCs as unique predictors: M1, M5 and M8 (Figs. 5.4a, e, h). The models based on climate indices (M12-M14) show only weak negative trends over the northern sector (Figs. 5.4l-n).

The percentages of variance of winter SWH from HEI accounted for by each statistical model are mapped in Fig. 5.5. Models M3, M7 and M10 account for a considerable amount of variance over large areas; on the contrary, M1 shows values lower than 50% everywhere. The spatial averaged fractions of variance captured by the best models are 44% (M3), 51% (M7) and 68% (M10); local values reach up to 97% in some areas, especially at mid and high latitudes.

Figure 5.6 shows the trends (computed over the validation period 1989-2009) of winter SWH, SWHw and SWHs for the HEI hindcast, the statistical models M15, M16 and the combination of both models according to equation 2. Similarly to M5-M11, a value of n=6 PCs was used to run M16. Hindcasted winter SWH and SWHw trends (Figs. 5.6a, b) are very similar in magnitude, especially at high latitudes, while the contribution of SWHs to the total trend is much lower, with maximum values of 2 cm/yr over reduced areas at high and mid latitudes, particularly in the Bay of Biscay (Fig. 5.6c).

Statistical models for the two components were able to represent the main features of the observed winter SWH, SWHw and SWHs trends (see Figs. 5.6d-f). Regarding the accounted variance, M15 was able to recover a high percentage (77% on average) of the hindcasted SWHw, while M16 recovered a small percentage (37% on average) of the hindcasted SWHs. The agreement for the wind component was high over all the domain, reaching 99% of explained variance in some regions (Figs. 5.6g, h). The agreement for the swell component was higher over the SW sector of the domain, where M16 reached a 93% of explained variance coinciding with swell-dominated areas (sometimes referred to as 'swell pools', see Semedo et al., 2011). However, along a significant part of the European coasts, particularly to the North of the Bay of Biscay, the swell component is poorly recovered by the M16 model. This is a key issue, since swell is the

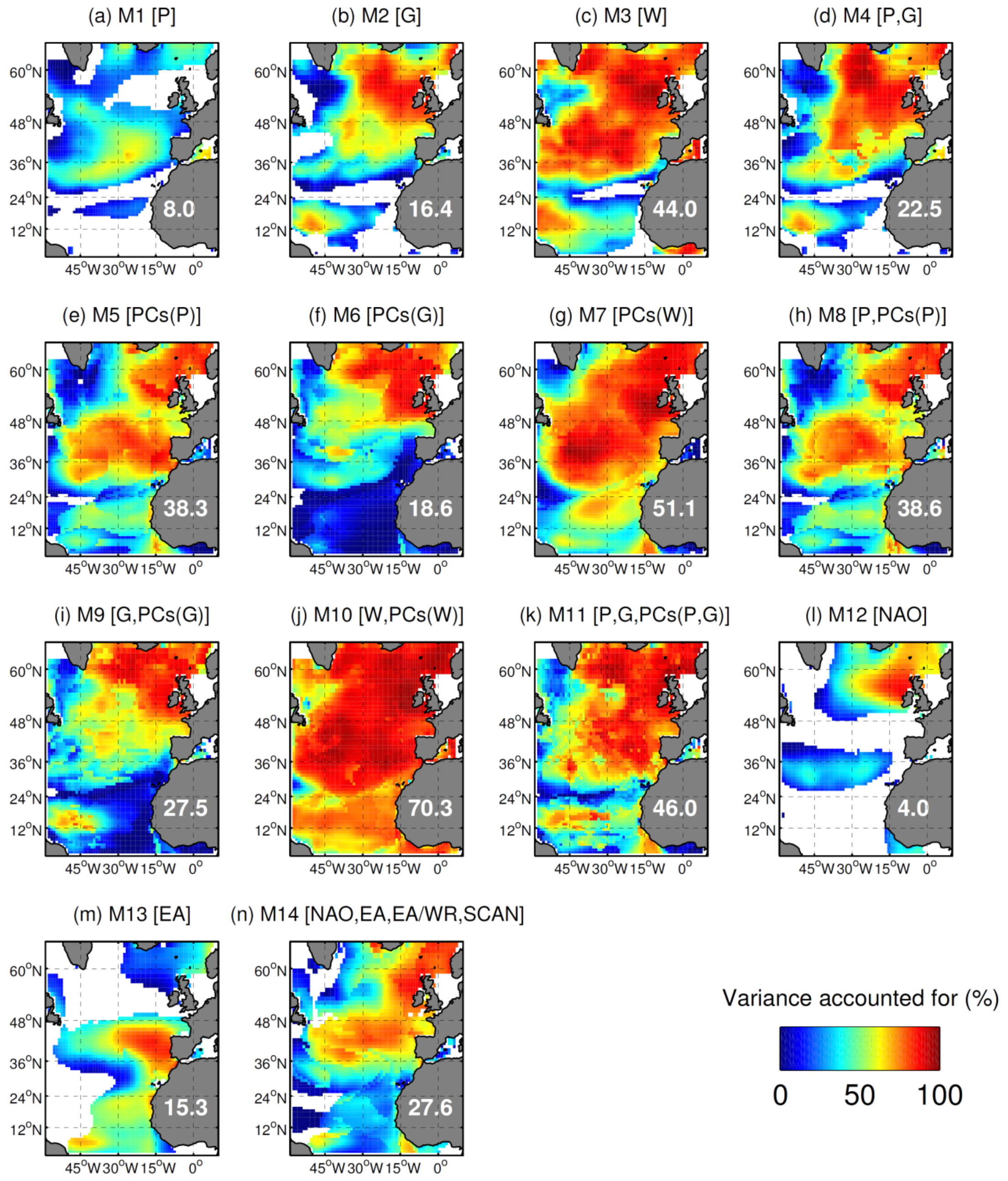

Figure 5.5. Percentage of variance of hindcasted winter SWH accounted for by each of the statistical models (a-n) for the period 1989-2009. Coloured areas denote model statistical significance (F-test) at 5% level. Spatially averaged values are also shown.

dominant component of the wave climate in those areas (Semedo et al., 2011). Overall, the models M10 and M17 explained the highest percentages of winter SWH variance, with values of 70% (Fig. 5.5j) and 67% (Fig. 5.6g).

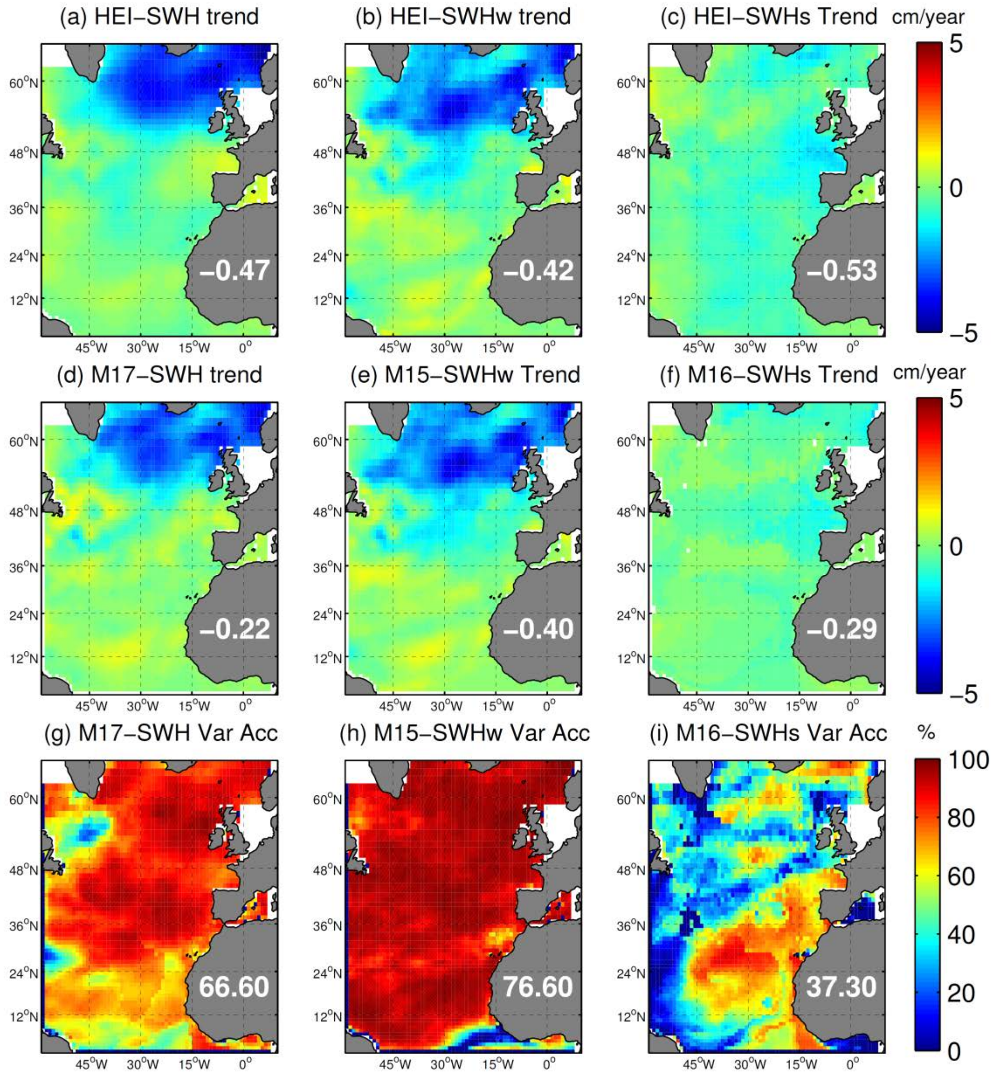

Figure 5.6. *Linear trends (cm/yr) of winter SWH, SWHw and SWHs for HEI (a-c), M17 (d), M15 (e) and M16 (f) obtained for the period 1989-2009. The percentage of HEI winter SWH, SWHw and SWHs variance accounted for M17, M15 and M16 respectively (g-i). Coloured areas denote model statistical significance (F-test) at 5% level. Spatially averaged values are also shown.*

5.4 Projections of wave climate for the 21st century

5.4.1 Dynamical projection

Winter SWH trends for 2000-2100 obtained from the DynProj simulation under the A1B scenario are shown in Fig. 5.7a. White dots denote statistically non-significant (F-test) trends at the 5% confidence level. The projection shows

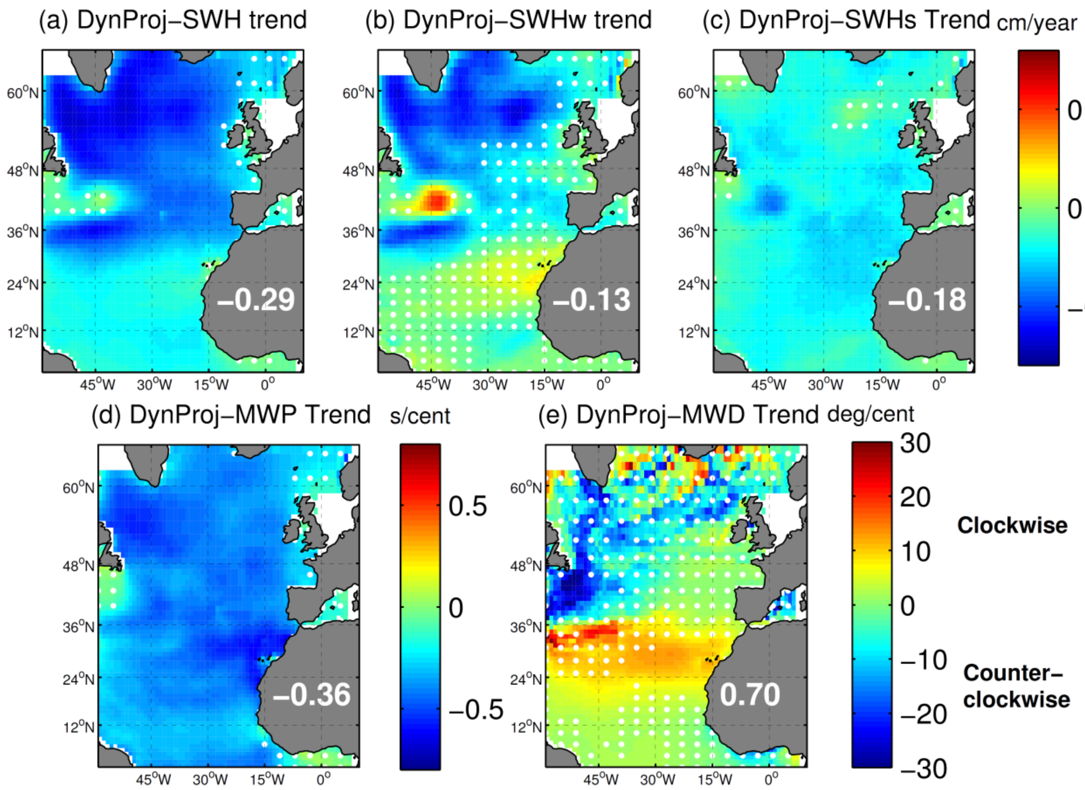

Figure 5.7. Linear trends of winter SWH (a), SWHw (b), SWHs (c) MWP (e) and MWD (f) obtained from DynProj for the period 2000-2100. White dots denote no statistical significance (F-test) at 5% level. Spatially averaged values are also shown.

negative (significant) trends over the North Atlantic, with values of -0.7 cm/yr above 30ºN latitude. Below 30ºN latitude trends are also negative, with values of -0.3 cm/yr, These results are consistent with previous studies based on dynamical approaches. For instance, Hemer et al. (2012) obtained a decrease of up to ~0.7m in annual SWH over the North Atlantic between 1979 and 2099, with higher decreases (~1m) during winter season (they used ECHAM5 wind fields under a SRES A2 scenario to force the WaveWatch III model; see Tolman, 2009 for details on the model). In the same line, Semedo et al. (2013) showed a decrease of up to 10% (~0.5m) in winter (DJF) SWH between 1959 and 2100 over the North Atlantic (they used high-resolution surface winds from ECHAM5 under A1B scenario to force the WAM model).

The linear winter trends of the two components of SWH (Figs. 5.7b, c) show different spatial patterns. SWHw shows negative changes in excess of -0.6 cm/yr at mid latitudes and in the NW sector of the North Atlantic, and positive (although non-significant) trends between 20-30ºN, mainly in the eastern sector,

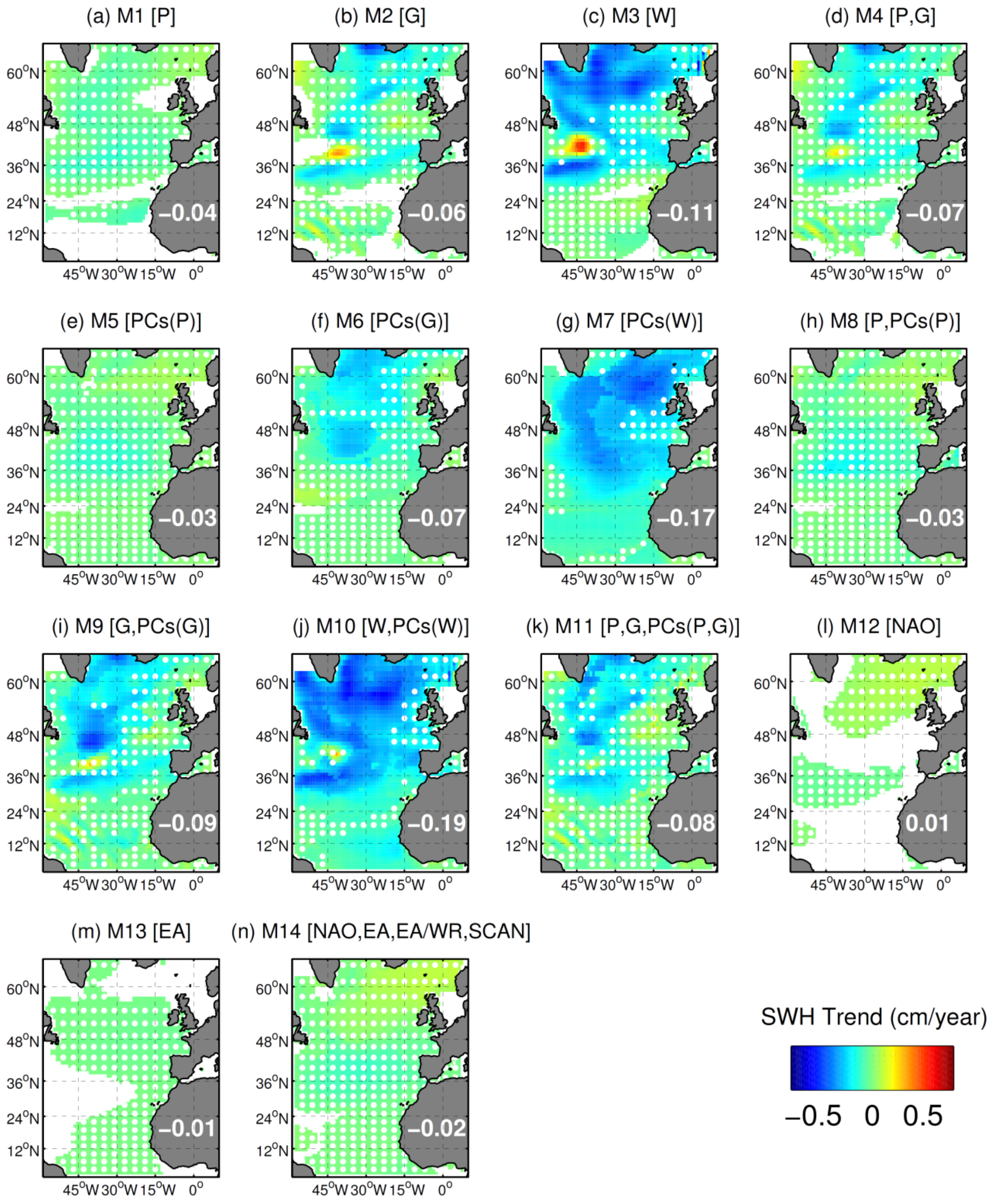

Figure 5.8. Linear trends (cm/yr) of winter SWH obtained from the statistical models (a-n) for the period 2000-2100. Coloured areas denote model statistical significance (F-test) at 5% level. White dots denote no statistical significance (F-test) of the trend at 5% level. Spatially averaged values are also shown.

in the area under the influence of the Trade winds. SWHs shows smaller (in absolute value) trends than SWHw; they are between -0.1 cm/yr and -0.2 cm/yr over most of the domain, reaching -0.4 cm/yr around 38-40ºN and 45ºW. All

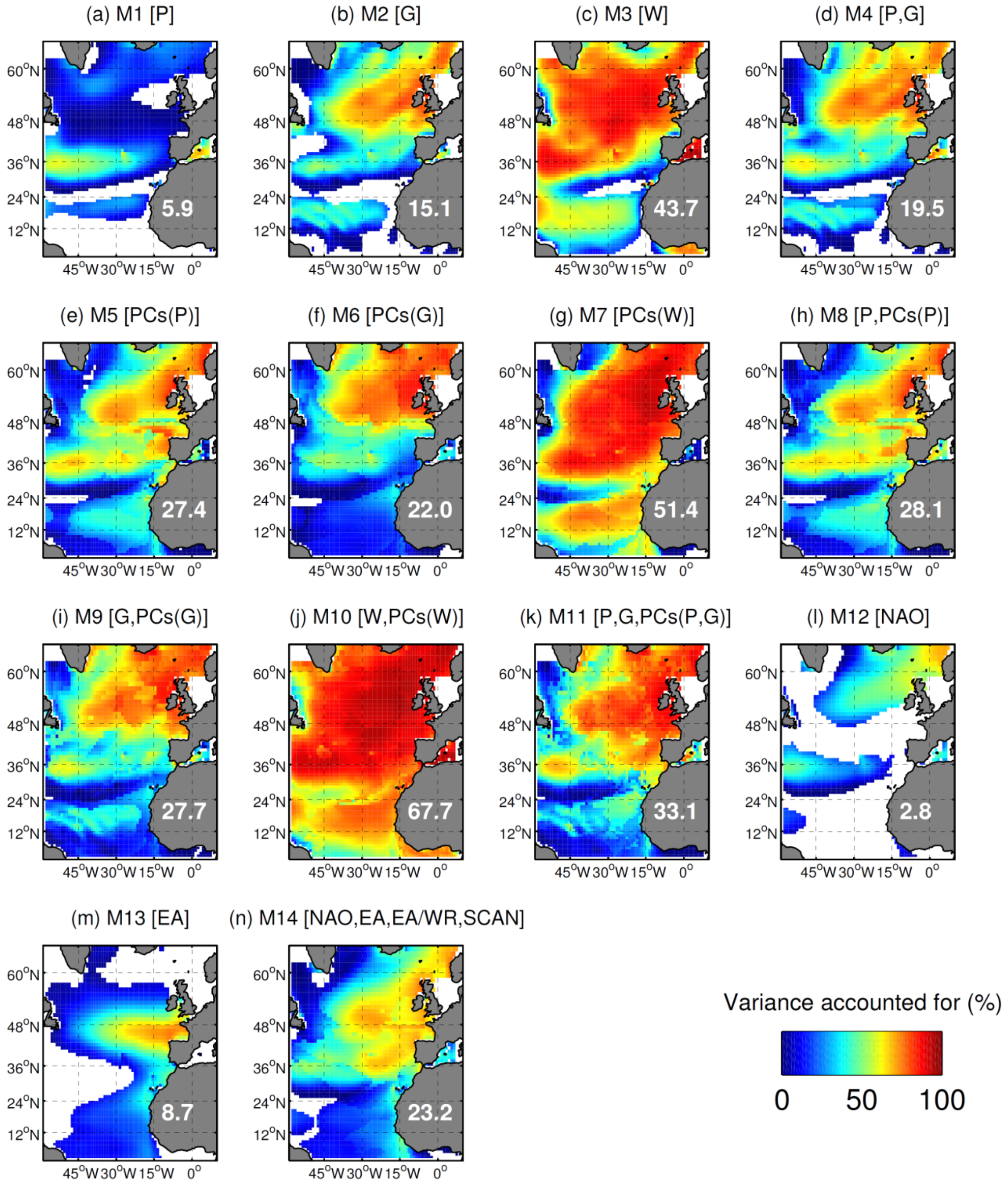

Figure 5.9. Percentage of variance of the DynProj winter SWH accounted for each of the statistical models (a-n) for the period 2000-2100. Coloured areas denote model statistical significance (F-test) at 5% level. Spatially averaged values are also shown.

these trends (Figs. 5.7a-c) will be used in the following as the basis for comparison with the statistical models.

In order to give a more complete description of the future wave projections provided by DynProj, the trends of both winter mean wave period (MWP) and mean wave direction (MWD) are also shown in Figs. 5.7d and 5.7e. The

Table 5.1. Spatially averaged percentages of variance of DynProj winter SWH (2000-2100, A1B scenario) accounted for by the statistical simulations (M1-M17). Spatially averaged winter SWH trends and the corresponding standard deviation (cm/year). Differences between averaged winter SWH trends of statistical simulations and DynProj (with an averaged value of-0.29cm/year).

Model	Variance account (%)	Mean trend (cm/year)	Std trend (cm/year)	Trend diff. (cm/year)
M1	5.9	-0.04	0.04	0.25
M2	15.1	-0.06	0.10	0.23
M3	43.7	-0.11	0.16	0.18
M4	19.5	-0.07	0.09	0.22
M5	27.4	-0.03	0.04	0.26
M6	22.0	-0.07	0.09	0.22
M7	51.4	-0.17	0.11	0.12
M8	28.1	-0.03	0.05	0.26
M9	27.7	-0.09	0.11	0.20
M10	67.7	-0.19	0.14	0.10
M11	33.1	-0.08	0.10	0.21
M12	2.8	0.01	0.05	0.30
M13	8.7	-0.01	0.01	0.28
M14	23.2	-0.02	0.05	0.27
M15	80.3	-0.12	0.19	0.01
M16	33.8	-0.09	0.05	0.09
M17	63.8	-0.20	0.19	0.09

simulation shows small but statistically significant negative MWP trends over the North Atlantic (-0.4 s/century, on average) reaching maximum values (-0.7 s/century) over the Canary Islands. These results are in agreement with Semedo et al.(2013), who showed an overall decrease in DJF MWP of up to 5% (~0.5s). Significant clockwise trends in MWD of about 10 deg/century are projected at 24ºN-36ºN latitudes reaching maximum values of 35 deg/century over the western sector. Conversely, counter-clockwise trends of about -10deg/century are projected over the north-western sector, reaching maximum values of up to -35 deg/century at 36ºN-48ºN latitudes. This trend pattern is in agreement with those projected by Hemer et al. (2012) and Andrade et al., (2007).

5.4.2 Statistical projections

Winter SWH trends during 2000-2100 (A1B scenario) obtained using the statistical models M1-M11 are mapped in Fig. 5.8 (a-k). Averaged values of explained variance and trend differences with DynProj are listed in Table 5.1. Most of the models show very weak trends over most of the domain. The exceptions are the models including W as a predictor, namely M3, M7 and M10, which show trend patterns and values closer to DynProj (Figs. 5.8c, g, j). The variance accounted for by each statistical model is shown in Fig. 5.9. It is worth

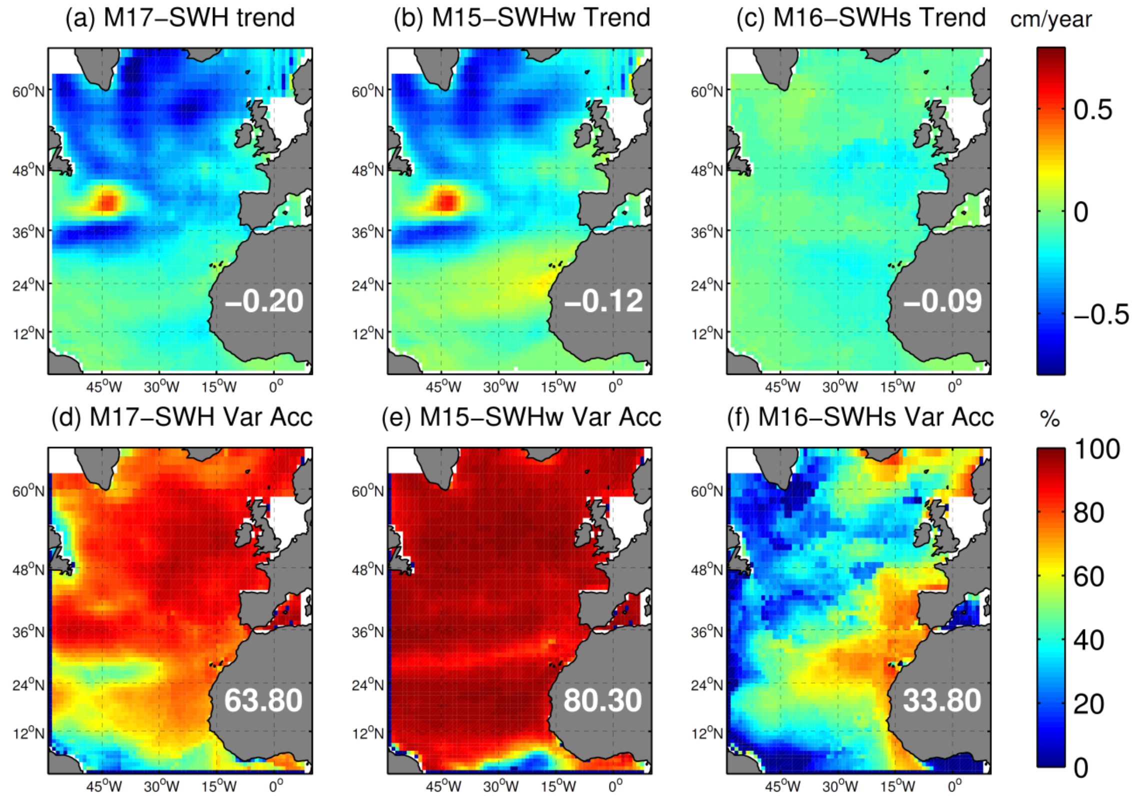

Figure 5.10. *Linear trends (cm/yr) of winter SWH, SWHw and SWHs for M17 (a), M15 (b) and M16 (c) for the period 2000-2100. Percentage of variance of DynProj winter SWH, SWHw and SWHs accounted for M17 (d), M15 (e) and M16 (f). Spatially averaged values are also shown.*

noting that models were detrended before the calculation of the explained variance, so that the latter does not include the variance associated with the trend. The variance accounted for is highest for M10, with an average value of 68% (Table 5.1) and a maximum of 95% in the north-central part of the basin, followed by M7 (51% on average and a maximum of 94%), M3 (44% on average and a maximum of 91%) and M11 (33% on average and a maximum of 90%).

Models based on climate indices (M12-M14) yielded very weak winter SWH trends (Figs. 5.7l-n) and only accounted for a small fraction of the variance (Figs. 5.9l-n). For example, M14, which includes all four climate indices as independent parameters, accounted for 23% of the variance on average (Table 5.1), with maximum values of 72% (Fig. 5.9n). Climate indices accounted for SWH variance regionally.The EA index-based model (M13) accounted for 78% of the variance at 48°N latitude (Fig. 5.9m) and the NAO index-based model (CM1) for 71% over the North Sea (Figs. 5.9l).

Models based on climate indices (M12-M14) yielded very weak winter SWH trends (Figs. 5.7l-n) and only accounted for a small fraction of the variance (Figs. 5.9l-n). For example, M14, which includes all four climate indices as independent parameters, accounted for 23% of the variance on average (Table 5.1), with maximum values of 72% (Fig. 5.9n). Climate indices accounted for SWH variance regionally.The EA index-based model (M13) accounted for 78% of the variance at 48ºN latitude (Fig. 5.9m) and the NAO index-based model (CM1) for 71% over the North Sea (Figs. 5.9l).

The results of the statistical models that address separately winter SWHw and SWHs are mapped in Fig. 5.10, together with the total winter SWH estimated from the combination of the two components. The M15 and M16 models reproduce the spatial patterns of winter trends obtained from the dynamical model (Figs. 5.7b-c) but with slightly smaller values in the case of M16 (Figs. 5.10b-c). Regarding the explained variance, M15 accounts for a large amount of winter SWHw variance (80% on average, with maximum values of up to 98%, Fig. 5.10e), while M16 accounts for a smaller fraction (34% on average, with large values only in the SE sector of the domain, where it accounts for up to 83% (see Table 5.1). When both contributions are combined (Figs. 5.10a,d), the spatial patterns of the trends and the variances accounted for are very similar to those obtained with M3 and M10. The negative trends obtained for SWH (reaching -0.9 cm/yr) are stronger than those obtained with DynProj. In terms of variance, the combined model (M17) accounted for 64 % of the DynProj variance on average (Table 5.1), reaching values of up to 96% in some areas. These results suggest that the statistical modelling of the wave field benefits from a separate modelling of the wind and swell components.

5.5 Discussion and conclusions

The ability of a statistical downscaling method based on 17 different combinations of predictors to project future changes in the wave climate of the North Atlantic Ocean has been explored. Statistical models have been calibrated during the period 1958-2002 by using atmospheric fields from ERA-40 reanalysis and wave fields from a dynamical hindcast (HE40). Another dynamical wave hindcast (HEI) and altimetry observations have been used to validate the statistical models. The changes projected by a dynamical wave model run for the period 2000-2100 are used as reference for the comparison. The reference dynamical projection (an ECHAM5 simulation run under the emission scenario A1B) shows a decrease of SWH over the North Atlantic, especially at high latitudes, which is in agreement with other works (e.g. Hemer et al., 2012, Semedo et al., 2013, Wang et al., 2014).

Previous works like the one by Wang and Swail (2006) had found that wave climate projections are sensitive to the choice of the forcing (in particular the selected GCM), while others like the one by Hemer et al (2013) pointed to the downscaling method (including the regional climate model) and to the choice between dynamical or statistical approach as major uncertainty sources. Our study complements these results by demonstrating three main issues pointed out in the following.

The first one is that the statistical models used in our study (transfer functions of the seasonally averaged wave fields) resulting in better agreement with the dynamical simulation (in terms of winter inter-annual variability and trends) are those using the wind as predictor. Namely, the use of wind speed as independent variable makes that statistical models can account for a significant part of the winter SWH inter-annual variability (68% on average for the model M10) and correctly reproduce the long term changes shown by dynamical projections. Regression models that use sea level pressure and/or its gradient as independent variables can also account for a part of the inter-annual variability of winter SWH (from 6% to 33% on average), but they cannot reproduce the dynamically projected long term trends over the North Atlantic. It is important to note, however, that wind is a difficult variable to project. The latest Intergovernmental Panel on Climate Change Assessment Report (IPCC AR5, 2013) states that there is a high uncertainty associated with future winds and storms (Bindoff et al., 2013). This is the reason why many statistical models use SLP fields to project SWH, instead of winds (e.g. Wang et al., 2010; Wang et al., 2012; Wang et al., 2014; Casas-Prat et al., 2014). The point to be underlined from our work is that efforts in reducing the uncertainties on projected wind fields would translate into more reliable statistical projections of wave climate.

A second issue dealt with in this work is the use of climate indices as predictors. The most important climate pattern over the North Atlantic is the NAO (Rogers et al., 1990) and its influence on wave climate has been discussed for more than a decade (Woolf et al., 2002; Bertin et al., 2013; Feng et al., 2014a,b). Hemer et al. (2013), for instance, forecasted negative SWH changes over almost the entire North Atlantic by the end of the 21st century using a CMIP3 ensemble, while at the same time they forecasted increases in the NAO index. This is consistent with observational studies (for example Woolf et al., 2002) that show a negative correlation between SWH and the NAO index at mid latitudes, but it is contradictory for the northern sector of the North Atlantic, where they are positively correlated. It should be noted, however, that dynamical models run with increasing GHG are not in agreement with each other regarding the future behaviour of the NAO index: while Feng et al. (2014a) did not find a significant NAO trend during the 21st century using the MSLP fields of the CMIP5 ensemble under a RCP85 scenario, Cattiaux et al. (2013) found negative NAO trends using a different method. Even though a negative trend of the NAO index could be related to the negative SWH changes projected by Wang et al. (2014) over the northern sector of the North Atlantic, it could not explain the negative SWH changes projected at middle latitudes. What we have shown is that the NAO index alone is not capable of describing the wave field over the north Atlantic. Even when the four major regional climate indices over the North Atlantic are used, the statistical modelling is not sufficiently good. The same applies to the present climate, when it has been shown that the four climate indices account for only a part of winter SWH variability (Martínez-Asensio et al., accepted. The non-stationarity of the relationships between wave parameters and climate indices may also be relevant. In this line, Hemer et al. (2012) found significant changes in the SWH-NAO relationships under warming conditions, especially over the Bay of Biscay.

The third issue demonstrated in this work is that the combination of two regression models, one for wind waves and another one for swell, based on different independent parameters, can improve the projected wave fields. And this is in spite of the limited performance of the statistical models for the swell component over a large part of the domain.

Summarizing, this study highlights the importance of the selection of the independent variables in the statistical models and demonstrates the uncertainty involved in simulating future wave climate on the basis of such statistical models. It must be noted that all regression models were tested using seasonal statistics of wave climate. If higher frequency processes were analyzed (e.g. storm events) the conclusions of the comparison may differ. The conclusions of this study are also relevant for future studies involving the results from the new developed CMIP5 models. A way to reduce the uncertainties would be to rely only on those statistical methods that use winds as a predictor. The problem in this case is that there is a significant spread in the projections of winds, so the use of a large number of GCMs (i.e. from the new developed CMPI5 or the on-going CMIP6) would be recommended in order to reduce the uncertainties.

Supporting Information

The following supporting information is available as part of the online article:

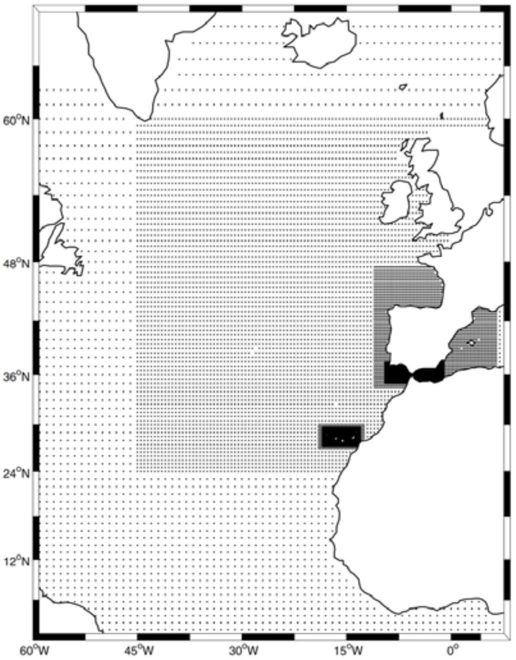

Figure 5.S1. *Domain of the WAM model in the North Atlantic. Grid points with the different resolutions used in different regions (black dots).*

Appendix 5.A

The Stepwise regression method used for statistical models with more than one predictor is illustrated with an example (see Table 5.S1): the fitting of model M7 at a specific grid point (-40ºW, 50ºN). The method first selects the most correlated dependent variable (the one with the less p-value of an F-statistics) and removes its influence through a regression analysis. Then it checks for the p-values of the rest of the dependent parameters. The term with a smallest p-value (lower than a value of 0.05) is then included in the model, assuming that there is sufficient evidence that this term has a non-zero coefficient (i.e. the null hypothesis is rejected). Conversely, if a p-value of any term included in the model is higher than 0.1 it is then excluded from the model. It means that there is sufficient evidence that this term has a zero coefficient. This forward/backward procedure is repeated until the model is not improved in terms of its p-value (note that the p-value reflects the total model performance and not that of the individual terms). Three different models are fitted at each step in the example (see Table 5.S1):

Step 1: SWH= - 5.7e10-4 PC1
Step 2: SWH= - 6.2e10-4 PC1 - 8.4e10-4 PC2
Step 3: SWH= - 6.5e10-4 PC1 - 8.4e10-4 PC2 + 2.9e10-4 PC3

The p-values and explained variances for each of these models are shown in Table 5.S1.

Table 5.S1. *P-value of each independent variable of the model M7 throughout the stepwise regression procedure at grid point (-40ºW, 50ºN). The percentage of HEI winter SWH variance accounted for M7 at each step is also shown.*

	Before stepwise regression		Step 1: PC1 included	Step 2: PC2 included	Step 3: PC3 included
	Corr. Coef.	Pvalue of an F-statistic			
PC1	-0.63	0.000007	0.000007	0.000000	0.000000
PC2	-0.54	0.000213	0.000000	0.000000	0.000000
PC3	0.12	0.437032	0.216563	0.032044	0.032044
PC4	0.10	0.507104	0.573319	0.092025	0.063947
PC5	0.30	0.048526	0.531827	0.951542	0.841806
PC6	0.00	0.998939	0.708841	0.425440	0.388856
Var.acc. (%)			40.9	79.5	82.2

Appendix 5.B

The along-track high-resolution SWH observations used to calibrate the hindcasts were obtained from the Ifremer altimeter Hs database (Queffeulou and Croizé-Fillon, 2010). This database consists of calibrated (Queffeulou, 2004) SWH measurements from seven altimeters (Jason-1, Jason-2, Topex/Poseidon, European Remote Sensing (ERS-1 and ERS-2), Envisat and Geosat Follow-On) spanning the period from January 1991 to December 2009. Along-track SWH observations were first aggregated onto a regular 2x2 degree grid and monthly averaged. Only those grid points with more than a 10% of the maximum number of available observations per cell (N = 96412) were selected. Gridded SWH data were then linearly interpolated onto a 1x1 degree grid. Finally, winter (DJFM) averaged fields were calculated. The comparison between altimeter and modelled winter SWH fields was done in terms of bias, URMSD and percentage of variance accounted for during the period 1991-2009 (see Fig. 5.S2).

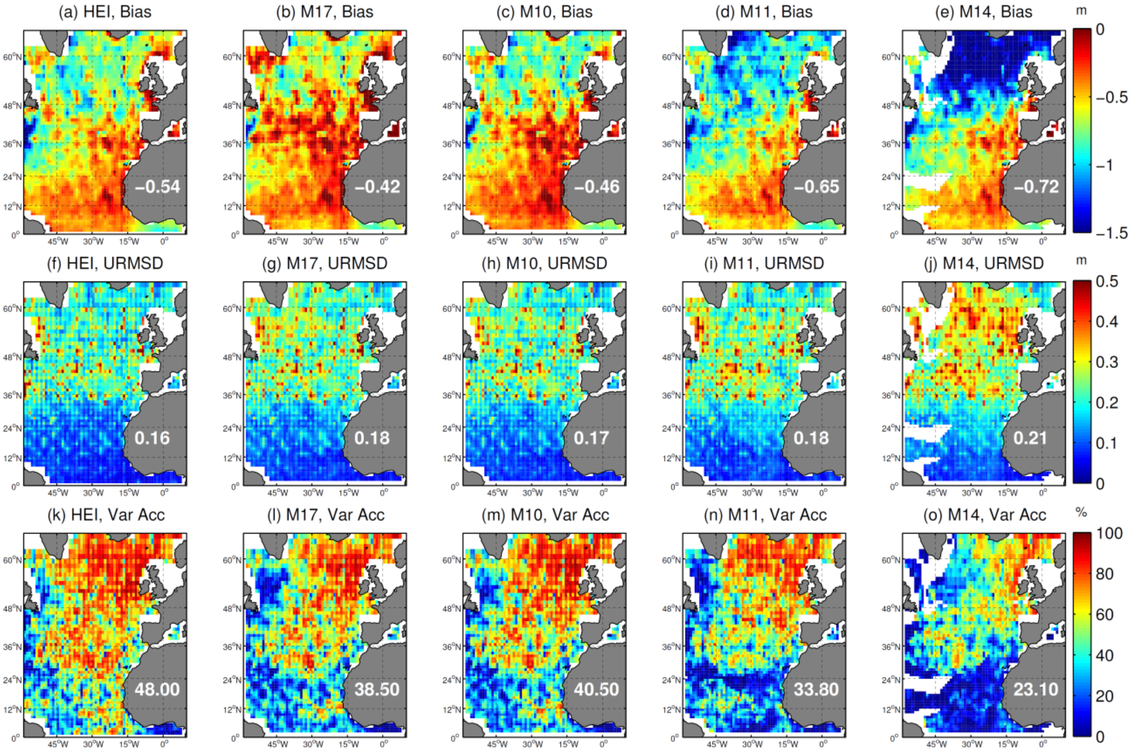

Figure 5.S2. *Bias (in meters) (a-e), URMSD (in meters) (f-j) and variance accounted for (in %) (k-o) between winter altimeter SWH and HEI (a, f, k), M17 (b, g, l), M10 (c, h, m), M11 (d, i, n) and M14 (e, j, o) for the period 1991-2009. Coloured areas denote that the statistical regression of the model is significant (F-test) at a 5% level. Spatially averaged values are also shown.*

Acknowlegdments

This work has been carried out in the framework of the projects VANIMEDAT-2 (CTM2009-10163-C02-01, funded by the Spanish Marine Science and Technology Program and the E-Plan of the Spanish Government) and ESCENARIOS (contract funded by the Agencia Estatal de METeorología). A. Martínez-Asensio acknowledges an FPI grant associated with the VANIMEDAT-2 project. M. Marcos and G. Jordà acknowledge a “Ramón y Cajal” contract funded by the Spanish Government. M.N. Tsimplis and X. Feng acknowledge Lloyd's Register Foundation, which supports the advancement of engineering-related education, and funds research and development that enhances safety of life at sea, on land and in the air. The final version of this work has been significantly improved thanks to the suggestions of three anonymous reviewers.

Bibliography

Andrade, C., H. O. Pires, R. Taborda, and M. C. Freitas, 2007. Projecting future changes in wave climate and coastal response in Portugal by the end of the 21st century. J Coast Res, 50, 263-257.

Ailliot, P., D. Allard, V. Monbet, and P. Naveau, 2014. Stochastic weather generators: an overview of weather type models.

Bertin, X., E. Prouteau, and C. Letetrel, 2013. A significant increase in wave height in the North Atlantic Ocean over the 20th century. Global Planet. Change, 106, 77–83.

Bindoff, N.L., P.A. Stott, K.M. AchutaRao, M.R. Allen, N. Gillett, D. Gutzler, K. Hansingo, G. Hegerl, Y. Hu, S. Jain, I.I. Mokhov, J. Overland, J. Perlwitz, R. Sebbari and X. Zhang, 2013. Detection and Attribution of Climate Change: from Global to Regional. In: Climate Change 2013: The Physical Science Basis. Contribution of Working Group I to the Fifth Assessment Report of the Intergovernmental Panel on Climate Change [Stocker, T.F., D. Qin, G.-K. Plattner, M. Tignor, S.K. Allen, J. Boschung, A. Nauels, Y. Xia, V. Bex and P.M. Midgley (eds.)]. Cambridge University Press, Cambridge, United Kingdom and New York, NY, USA.Casas-Prat M., X. L. Wang, and J. P. Sierra, 2014. A physical-based statistical method for modeling ocean wave heights. Ocean Model, 73:59–75

Camus, P., M. Menéndez, F. J. Méndez, C. Izaguirre, A. Espejo, V. Cánovas, J. Pérez, A. Rueda, I. J. Losada, and R. Medina, 2014. A weather-type statistical downscaling framework for ocean wave climate, J. Geophys. Res. Oceans, 119, 7389–7405.

Cattiaux, J., H. Douville, and Peings, Y.,2013. European temperatures in CMIP5: origins of present-day biases and future uncertainties. Climate dynamics, 41(11-12), 2889-2907.

Charles, E., D. Idier, P. Delecluse, M. Déqué, and G. Le Cozannet, 2012. Climate change impact on waves in the Bay of Biscay, France. Ocean Dynamics, 62(6), 831-848.

Draper, N.R., and H. Smith, 1998. Applied Regression Analysis. Wiley-Interscience, Hoboken, NJ pp. 307–312.

Fan, Y., I., I. M. Held, S.-J. Lin, and X. Wang, 2013. Ocean warming effect on surface gravity wave climate change for the end of the twenty-first century. J. Climate, 26, 6046–6066.

Fan, Y., S. J. Lin, S. M. Griffies, and M. A. Hemer, 2014. Simulated global swell and wind-sea climate and their responses to anthropogenic climate change at the end of the twenty-first century. Journal of Climate, 27(10), 3516-3536.

Feng, X., M.N. Tsimplis, M.J. Yelland, and G.D. Quartly, 2014a. Changes in significant and maximum wave heights in the Norwegian Sea. Global and Planetary Change, 113, 68-76.

Feng, X., M.N. Tsimplis, G.D. Quartly, and M.J. Yelland, 2014b. Wave height analysis from 10 years of observations in the Norwegian Sea. Continental Shelf Research, 72, 47-56.Günther, H., S. Hasselman, and P. A. E. Jansen, 1992. The WAM model cycle, 4. Technical Report 4. DKRZ.

Günther, H., Hasselman, S., & Jansen, P. A. E. (1992). The WAM model cycle, 4. Technical Report 4. DKRZ.

Hasselmann, S., C. Brüning, K. Hasselmann, and P. Heimbach, 1996. An improved algorithm for retrieval of ocean wave spectra from synthetic aperture radar image spectra. J. Geophys. Res., 101, 16 615-16 629

Hemer, M. A., J. Katzfey, and C. Trenham, 2012. Global dynamical projections of surface ocean wave climate for a future high greenhouse gas emission scenario. Ocean Modelling, 70, 221–245

Hemer, M. A., Y. Fan, N. Mori, A. Semedo, and X. L. Wang, 2013. Projected changes wave climate from a multi-model ensemble. Nature Clim. Change, 3, 471–476.

Izaguirre, C., F. J. Méndez, M. Menéndez, and I. J. Losada, 2011., Global extreme wave height variability based on satellite data, Geophys. Res. Lett., 38, L10607, doi:10.1029/2011GL047302.

Kistler, R., E. Kalnay, W. Collins, S. Saha, G. White, J. Wollen, M. Chelliah, W. Ebisuzaki, M. Kanamitsu, V. Kousky, H. van den Dool, R. Jenne, and M. Fioriono, 2001. The NCEP/ NCAR 50-year reanalysis: monthly means CD-ROM and documentation. Bull. Am. Meteorol. Soc. 82, 247–267.

Lorenz, E. N., 1969. Atmospheric predictability as revealed by naturally occurring analogues. Journal of the Atmospheric sciences, 26(4), 636-646.

Martinez-Asensio, A., M.N. Tsimplis, M. Marcos, X. Feng, D. Gomis, G. Jorda, and S. Josey, (accepted in International Journal of Climatology) Response of the North Atlantic wave climate to atmospheric modes of variability.

Mori, N., T. Yasuda, H. Mase, T. Tom, and Y. Oku, 2010. Projection of extreme wave climate change under global warming. Hydrol. Res. Lett., 4, 15–19.

Pérez, J., M. Menéndez, F.J. Méndez, and I. J. Losada, 2014. Evaluating the performance of CMIP3 and CMIP5 global climate models over the north-east Atlantic region. Climate Dynamics, 43(9-10), 2663-2680.

Queffeulou P., 2004. Long term validation of wave height measurements from altimeters, Marine Geodesy, 27, 495-510.

Queffeulou, P., and D. Croizé-Fillon, 2010. Global altimeter SWH data set, version 7, <ftp://ftp.ifremer.fr/ifremer/cersat/products/swath/altimeters/waves/>.

Richman, M. B. 1986. Rotation of principal components. J. Climatol. 6, 293_335.

Roeckner, E., G. Bauml, L. Bonaventura, R. Brokopf, M. Esch, M. Giorgetta, S. Hagemann, I. Kirchner, L. Kornblueh, E. Manzini, A. Rhodin, U. Schlese, U. Schulzweida, and A. Tompkins, 2003. The atmospheric general circulation model ECHAM 5. Part I: model description.Technical Report 349, Max Planck Institute for Meteorology Rogers, J.C., 1990. Patterns of low frequency monthly sea level pressure variability (1899-1986) and associated wave cyclone frequencies. J. Climate, 3, 1364-1379.

Rogers, J.C.,1990. Patterns of low frequency monthly sea level pressure variability (1899-1986) and associated wave cyclone frequencies. J. Climate, 3, 1364-1379.

Semedo, A., K. Sušelj, A. Rutgersson, and A. Sterl, 2011. A global view on the wind sea and swell climate and variability from ERA-40. Journal of Climate,24(5), 1461-1479.

Semedo, A., Ralf Weisse, Arno Behrens, Andreas Sterl, Lennart Bengtsson, and Heinz Günther, 2013. Projection of Global Wave Climate Change toward the End of the Twenty-First Century. J. Climate, 26, 8269–8288.Shimura T., N. Mori and H. Mase, 2013. Ocean waves and teleconnection patterns in the Northern Hemisphere, Journal of Climate, 26, pp.8654-8670

Tolman, H. L., 2009. User manual and system documentation of WAVEWATCH III TM version 3.14. Technical note, MMAB Contribution, 276.

Wallace, J. M., C. Smith, and C. S. Bretherton, 1992. Singular value decomposition of wintertime sea surface temperature and 500-mb height anomalies. Journal of climate, 5(6), 561-576.

WAMDI Group, 1998. The WAM model-A third generation ocean wave prediction model, J. Phys. Oceanogr., 18, 1775–1810.

Wang X.L.L., F.W. Zwiers and V.R. Swail, 2004. North Atlantic ocean wave climate change scenarios for the twenty-first century. J Clim 17:2368–

2383

Wang, X. L., and V. R. Swail, 2006. Climate change signal and uncertainty in projections of ocean wave heights. Clim. Dyn., 26, 109–126.

Wang, X. L., V. R. Swail, F. W. Zwiers, X. Zhang, and Y. Feng, 2008. Detection of external influence on trends of atmospheric storminess and ocean wave heights, Clim. Dyn., 32, 189–203.

Wang, X. L., V. R. Swail, and A. Cox, 2010. Dynamical versus statistical downscaling methods for ocean wave heights, Int. J. Climatol., 30, 317–332.

Wang, X. L., Y. Feng, and V. R. Swail, 2012 North Atlantic wave height trends as reconstructed from the twentieth century reanalysis, Geophys. Res. Lett., 39, L18705.

Wang X. L, Y. Feng, and V. R. Swail, 2014. Changes in global ocean wave heights as projected using multimodel CMIP5 simulations. Geophys Res Lett 41(3):1026–1034

Wilby, R. L., S. P. Charles, E. Zorita, B. Timbal, P. Whetton, and L. O. Mearns, 2004. Guidelines for use of climate scenarios developed from statistical downscaling methods. Supporting material of the Intergovernmental Panel on Climate Change. Task Group on Data and Scenario Support for Impacts and Climate Analysis, Rotherham

Wilks, D. S., 1998. Multisite generalization of a daily stochastic precipitation generation model. Journal of Hydrology, 210(1), 178-191.

Woolf, D.K., P.D. Cotton, and P.G. Challenor, 2002. Variability and predictability of the North Atlantic wave climate. Journal of Geophysical Research 107 (C10), 9–23.

Young, I. R., S. Zieger, and A. V. Babanin, 2011. Global trends in wind speed and wave height. Science, 332(6028), 451-455.

Zorita, E., and H. Von Storch, 1999. The analog method as a simple statistical downscaling technique: comparison with more complicated methods. Journal of climate, 12(8), 2474-2489.

Chapter 6

Discussion and concluding remarks

> *—Nunca se ha de pensar en toda la calle de una vez, ¿entiendes? Sólo hay que pensar en el paso siguiente, en la inspiración siguiente, en la siguiente barrida. Nunca nada más que en el siguiente.*
>
> *—You must never think of the whole street at once, understand ? You must only concentrate on the next step, the next breath, the next stroke of the broom, and the next, and the next. Nothing else.*
>
> Michael Ende, *Momo* (1973)

The sea level and wave climate play an important role on coastal societies, assets and ecosystems. At present, the amplitude of the inter-annual variability of these high impact marine variables is at least as large as the forcing signal derived from the increasing greenhouse gas concentrations. This makes that, in some regions, the interannual marine climate variability can mask the signal resulting from global warming, while in others it can increase its magnitude.

The work presented in this thesis was aimed, first, at improving the understanding of the processes driving the interannual variability of the high impact marine variables observed over the North Atlantic Ocean and the Mediterranean Sea during the second half of the 20th century. Further, it has also explored the future responses of these key variables to the atmospheric climate variability and change during the 21st century. Particular attention has been paid to characterize their responses in terms of the large-scale modes of atmospheric circulation.

The results are based on the analysis of different types of data. Regarding observations we have used tide gauge records describing total sea level, wave buoy observations giving the different wave parameters, satellite altimetry giving remote estimations of sea level anomalies and significant wave heights, and hydrographic data bases giving the steric component of sea level. These observations are complementary to the outputs from different types of numerical models (reanalyses, hindcasts and climate projections) describing atmospheric parameters such as sea level pressure and winds and marine parameters such as the atmospheric component of the sea level and waves.

This final chapter intends to highlight the most relevant results presented throughout the thesis, as well as to place them in a common thread defined by the research projects that have framed the work. It is worth stressing that we do not intend to give a complete view of the marine climate over the domain of interest. Instead, we have worked out specific issues that have resulted in a collection of four related, but independent research articles that constitute the nucleus of the work. Nevertheless, the major findings summarized in the following are presented in terms of their topic, rather than just pointing out the major conclusions of each paper.

Characterization of the present wind-wave climate of the Western Mediterranean

A new calibrated product of SWH over the Western Mediterranean spanning the last five decades has been generated and is now freely distributed to the users through the web site of the Sea Level and Climate Research Group. This work was identified as a relevant added value for the wind-wave hindcast generated in the framework of the ESCENARIOS project. The calibration of hindcasted SWH has proven satisfactory in correcting, to a great extent, the differences between the model output and the point-wise observations from buoys, as well as remote observations from altimetry. A key lesson to learn from the results obtained is that, although the best results in terms of similarity with observations were obtained using the highest number of buoys available in the calibration, it is possible to obtain a similar performance with a number of buoys significantly lower, as far as these are evenly distributed. This result highlights the importance of considering the available observations when planning an increase of the instrumental network. The main limitation of the method developed for the calibration is the use of a log-normal distribution, which only allows the calibration of the mean regime (the log-normal distribution does not take into account the extreme values). Therefore, the calibrated fields must be used with caution when extreme waves are concerned.

The obtention of an accurate, calibrated hindcast allows a better characterization of the present wind-wave climate of the Western Mediterranean, which is essential for the design of coastal infrastructures and coastal management in general. While there were previous validated hindcasts in the region, this is the first one that covers the entire basin and extends until present time (which has allowed the use of a larger number of buoys for the calibration).

Large scale climate modes and Mediterranean sea level

Sea level variability in the Mediterranean Sea has been the focus of most of the research developed by the Sea Level and Climate Research Group during the last decade. The availability of new regional marine simulations generated in the framework of the VANIMEDAT2 project has represented a step forward in these investigations. One of the topics dealt with in this thesis and not addressed in earlier studies is the influence of the large scale atmospheric climate modes onto Mediterranean total sea level and and onto its different components.

The investigation of the relationships between the large-scale atmospheric patterns over the North Atlantic and Europe (NAO, EA, EA/WR and SCAN) and Mediterranean sea level has confirmed that the NAO is the atmospheric pattern having the largest overall impact and particularly during winter. The winter season is mostly considered because of its larger sea level variability. Some influence of the climate modes has also been detected in summer, but it is less important than in winter. The way the NAO acts onto Mediterranean sea level is through two processes which, combined, amplify the atmospheric signal: i) the direct forcing of atmospheric pressure and wind over the basin; and ii) the remote forcing produced by changes in the winds over the North Atlantic sector close to the Strait of Gibraltar, which induce mass exchanges throughout the Strait that obviously affect sea level within the basin.

The other three indices have a smaller impact: the SCAN index is redundant with the NAO since they are significantly anti-correlated in winter over the domain of interest; the EA/WR pattern significantly contributes to the winter Mediterranean sea level variability through its impact on atmospheric pressure changes; and the EA pattern is related to the rate of change of the thermosteric sea level overall the basin through its impact on surface heat fluxes. This altogether has contributed to clarify the main drivers of the observed variability, as the climate indices altogether explain more than 80% of the winter sea level variability (less than a half in summer).

Large scale climate modes and North Atlantic wave climate

Given the expertise developed with large scale climate patterns and the availability of several decades of simulated wind-wave fields over the North Atlantic Ocean, the same argument as for regional sea level was followed to study the relationships between large scale patterns and the wave climate in that region.

In a first step, the relationships were established for present-day wave climate using a wind-wave hindcast of the last decades. The results underline that the NAO and the EA are the patterns that have the largest impact in this region and that this influence is most important in winter. The higher impact of the NAO on wave heights and periods occurs over two areas located at different latitudes (namely, the northern and central sectors of the North Atlantic Ocean) while the higher impact of the EA is located among them and reaches the southern sector, mainly due to the response of the swell component to this pattern. Surprisingly, the impact of the NAO over the southern sector is masked by an opposite response of both the local (wind sea) and remote (swell) components of wave climate to the NAO. Wave directions respond to both patterns over almost all the basin. SCAN and EA/WR patterns are less important for the wave climate, as they have a lower impact in terms of intensity and areas of significant correlation.

A dynamical projection of the 21st century wind-wave climate over the North Atlantic was also generated in the framework of the ESCENARIOS project. This was used, first, to test whether the projected climate indices are good indicators of the changes projected for the wave climate. In addition to this, the dynamical projection was used to test different statistical wave models; these comprised both the models most commonly used in the literature and new models using different predictors, such as wind or separating wind-sea and swell components. The comparison of the whole set of wind-wave climate statistical simulations with the dynamical model revealed that only those statistical models using wind speed as predictor were capable of reproducing the winter wave climate variability and trends simulated by the dynamical model during the 21st century. This is not a surprising result, as in these cases both the statistical and the dynamical models were forced by the same wind fields. Moreover, the use of the wind speed as a predictor raises the question of the reliability of the wind fields produced by climate projections in comparison with other better behaved variables such as the atmospheric pressure. What our results point out, therefore, is that future wave projections would largely benefit of improved projections of wind fields.

Finally, our work also showed that another way to improve future wave projections is through the combination of two statistical regression models, one for the wind-sea component and other for the swell component, based on different predictors. If in a near future statistical models demonstrate to project the wave climate with the same accuracy than dynamical models it would be a big step forward. The reason is these models are much cheaper in terms of computational cost, which would allow to obtain a large number of simulations and hence a better estimation of the uncertainties associated with the projection ensemble.